PERFORMANCE STUDY AND OPTIMIZATION OF THE ZEPHERGY WIND TURBINE

A Thesis

by

MOEIN SOODAVI

Submitted to the Office of Graduate and Professional Studies of
Texas A&M University
in partial fulfillment of the requirements for the degree of

MASTER OF SCIENCE

Chair of Committee,	Othon K. Rediniotis
Committee Members,	Paul Cizmas
	Mark Holtzapple
Head of Department,	Rodney Bowersox

December 2013

Major Subject: Aerospace Engineering

Copyright 2013 Moein Soodavi

ABSTRACT

There are many problems associated with small wind turbines, such as small Reynolds number and poor starting performance, that make them much more expensive than the large ones per unit power. New technologies are needed to improve the quality of these turbines and reduce their costs. This thesis investigates a novel type of small wind turbine called Zephergy. Unlike conventional wind turbines, Zephergy is composed of more than one rotor/stage. A two-stage turbine is examined here. Each stage has two inner and outer rings. The blades are designed based on the recognized principles of turbomachinery, and are mounted between the two rings. Initially, performance of each individual stage is studied and compared to the performance of Bergey XL 10 kW as a typical small-size wind turbine. Next, various experiments are performed and the results are analyzed when both stages are installed in the test section to see how the presence of one stage affects the operation of the other. Our work shows that the Zephergy wind turbine performs very well especially in terms of the efficiency and starting performance.

DEDICATION

I would like to dedicate this work to my parents, Mr. Mohammad Soodavi and Ms. Rezvan Saadatpoor, and my siblings, Ms. Nasim Soodavi and Mr. Mojtaba Soodavi whose unbounded support and love always keep me going.

ACKNOWLEDGEMENTS

I would never have been able to finish my thesis without the guidance of my committee members and help from friends.

I would like to express my deepest gratitude to my adviser, Dr. Othon Rediniotis, for his excellent guidance, caring, patience, and providing me with an excellent atmosphere for doing research. I could not have imagined having a better adviser and mentor for my Master's study.

Besides my adviser, I would like to thank the rest of my thesis committee: Dr. Paul Cizmas and Dr. Mark Holtzapple for their insightful comments. I would also like to thank Dr. Hamid Toliyat for letting me do some experiments at his laboratory: Electrical Machines & Power Electronics (EMPE) Laboratory at Texas A&M University. My thanks also go to Dr. Ahmadreza Tabesh for his guidance about electrical machines.

I would like to extend my gratitude to Michael Joly for designing the blades of the Zephergy wind turbine. My sincere thanks also go to a group of friends who helped me run different experiments: Siavash Pakdelian, Kamyar Ravaji, Majid Tabesh, and Yogesh Babbar.

Finally, I thank my department faculty and staff for making my time at Texas A&M University a great experience.

NOMENCLATURE

α	Angle of Attack
β	Flow Angle
β_f	Metal Angle
θ	Pitch Angle
λ	Tip Speed Ratio
ρ	Density of Air
υ	Kinematic Viscosity
ϕ	Yaw Angle
Φ	Flux
ω	Angular Velocity
a	Axial Induction Factor
$a^{'}$	Rotational Induction Factor
A	Area
c	Chord Length
C_d	Drag Coefficient
C_l	Lift Coefficient
C_p	Power Coefficient
I	Current
P	Power
R	Radius of Turbine Rotor Disk and Resistance
R_e	Reynolds Number
T	Period
U	Blade Velocity

V	Free Stream Velocity and Voltage
W	Relative Velocity of Fluid to Rotor
AC	Alternating Current
AWEA	American Wind Energy Association
DC	Direct Current
NACA	National Advisory Committee for Aeronautics
PM	Permanent Magnet
PV	Photovoltaics

Units

Ω	ohm
A	ampere
Btu	British thermal unit
g	gram
hp	horsepower
lb	pound
m	meter
mph	miles per hour
N	newton
oz-in	ounce-inch
rad	radian
rpm	revolutions per minute
s	second
V	volt
W	watt
Wh	watt-hour

Prefixes

G	Giga
k	Kilo
m	Milli
M	Mega

TABLE OF CONTENTS

LIST OF FIGURES

FIGURE Page

LIST OF TABLES

TABLE Page

1. INTRODUCTION

1.1 An Introduction to Wind Energy

As indicated in the Annual Energy Outlook 2013 [5], the energy consumption in the United States increases 0.3% per year from 2011 to 2040 and grows to 107.6 quadrillion Btu in 2040. There are many concerns associated with the conventional energy resources such as fossil fuel; the emission of greenhouse gases specially CO_2 and global climate change, air pollution, water withdrawal, and insecurity and instability of these resources are just a few to name [6]. Currently, 30 states and the District of Columbia have enacted the renewable portfolio standard (RPS) under which each state is supposed to provide a specific amount of its required energy from the renewable capacities, for instance, Texas has set a target to generate 5880 MW electricity from wind, solar, biomass, etc. by 2018 [5]. The majority of the states are going to reach or exceed the target points [7]. Federal incentives such as tax credits and loan guarantees, and improvements in technologies that result in reducing the equipment costs of wind turbines and solar PV systems as well as achieving a better performance, are two major factors that provide a suitable environment for the renewable energy generation [5].

In the United States, electricity demand increases from 3,839 billion in 2011 to 4,930 billion kWh in 2040 [5]. It is estimated that 20% of the total generated electricity in 2040 will be provided by the renewable resources [5]. It should be mentioned that the high increase in the renewable capacity during the initial years of the period results from the financial incentives that expire at the end of 2012, 2013, and 2016. If the tax credits are not extended after 2016, the growth will significantly decrease through 2030 mainly because of the natural gas low price, but significant

improvements in the renewable technologies make them cost-competitive after 2030 and result in the growth of the electricity generation from the renewable resources. Although the solar-based generation leads the capacity increase by more than 1000%, wind will still be the major renewable resource thanks to the rapid growth of the wind power in the last decade in response to the production tax credits [5].

According to the American Wind Energy Association annual report [8], 13,131 MW of the new wind capacity was installed in 2012 (28% annual growth) that resulted in the cumulative capacity of 60 GW, and interestingly for the first year, wind power was the largest source of the new electricity generation with 41.6% share. Sixty gigawatt wind power prevents about 100 million metric tons of CO_2 per year that is equivalent to 4% of the total carbon dioxide emitted by power plants [8].

1.2 An Introduction to Small-size Wind Turbines

AWEA defines a small wind turbine as a turbine with a rated power less than 100 kW [9]. The rated power is the generated power at the maximum performance of the wind turbine. Small turbines are subdivided into three groups [4] as indicated in Table 1.1. The numbers in the table are typical values, and could be different for various turbines.

Category	P (kW)	R (m)	Max. ω (rpm)	Application
Micro	≤ 1	1.5	700	Electric fences, Yachts
Mid-range	1-20	2.5	400	Remote power systems, Single-user grid connections
Mini	≥ 20	5	200	Mini grids, Remote communities

Table 1.1: Classification of small turbines [4].

Interestingly, micro-turbines are the most common small wind turbines. China, Britain and the United States are the leading producers of these turbines [1].

Basics of the operation are the same for all sizes of wind turbines, but some issues depend on the size [1]. Here are some major differences between small and large wind turbines:

- Aerodynamic operation of small wind turbines is severely affected by small Reynolds numbers.

- Because of the high cost, pitch control is not usually used in small turbines that makes it impossible to adjust the angle of attack based on the wind direction. This problem is specially important when the blades are going to start turning but at first they have to overcome the large resistive torques caused by the generator coupled to the turbine.

- Small wind turbines are installed in places that power is required, for example close to a house. These places are not necessarily the windiest locations whereas large turbines are located in windy areas.

- Yaw systems are used in large wind turbines to align the rotor to the wind. This mechanism is very expensive for small turbines. So some other options such as tail fins are employed, but none of them are optimal. It should be mentioned that if the yaw angle is denoted by ϕ, the generated power decreases proportional to $\cos^2(\phi)$ [10, 11].

- A protection system is required for all turbines at very high wind speeds. Although large turbines use a brake on the shaft, the small ones use a furling system that has some problems and is not an optimal method. More details about the furling system are found in [1].

- Large turbines are upwind, i.e., when seen from the upstream, the blades are in front of the tower. Also, they have two or three blades. But many more

types of small turbines are available in the market, and both types of upwind and downwind are common. In addition, the number of blades could change from two to seven.

Two major challenges that small-size wind turbines have to deal with are briefly investigated here: small Reynolds number and starting performance.

1.2.1 Small Wind Turbines and Reynolds Number

Reynolds number for an airfoil is defined as

$$Re = \frac{Wc}{\upsilon} \tag{1.1}$$

where c is the chord length, υ is the kinematic viscosity, and W is the magnitude of the wind velocity relative to the airfoil as indicated in Figure 1.1.

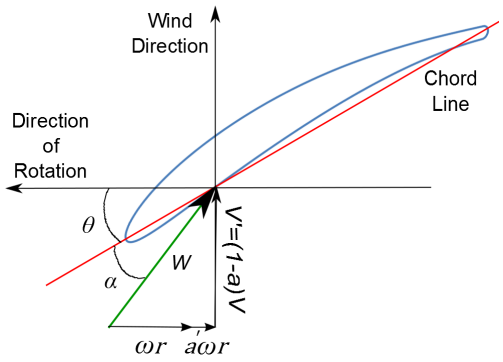

Figure 1.1: Velocities at radius r of a wind turbine blade [1].

Parameters a and $a^{'}$ are the axial and rotational induction factors [12]. By means of the control volume method, it can be easily shown that the magnitude of the wind velocity at the turbine plane changes to $V^{'} = (1-a)V$ where V is the free stream

velocity. Also, the circumferential velocity of the blade section that is located at radius r is ωr if its rotational velocity is ω. It can be shown that the turbine induces a rotational velocity equal to $a^{'}\omega r$ on the airflow. Pitch angle and angle of attack are shown by θ and α, respectively. It is desired that the forces applied on a wind turbine blade generate some torque about the axis of rotation. Figure 1.2 indicates that the lift force is increasing this torque whereas the drag reduces it. So the ratio of lift to drag is a more critical parameter in evaluating the performance of a wind turbine than the individual forces.

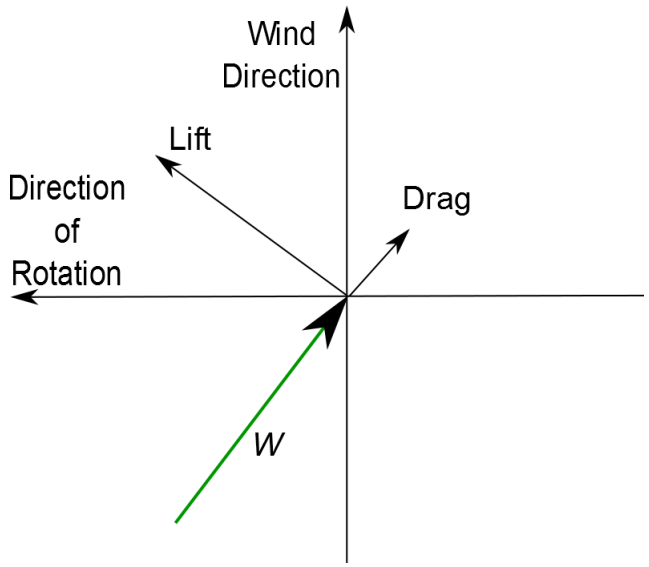

Figure 1.2: Lift and drag forces on a blade of a wind turbine [1].

Reynolds number could effectively change this ratio, for instance, the ratio for two special types of airfoil, SG6040 and SG6043, that are used in manufacturing small wind turbines, is shown at different Reynolds numbers in Figure 1.3. As it can be seen, higher Reynolds numbers result in larger lift-to-drag ratios at different angles of attack. Aerodynamics at low Reynolds numbers is more extensively investigated

in [13].

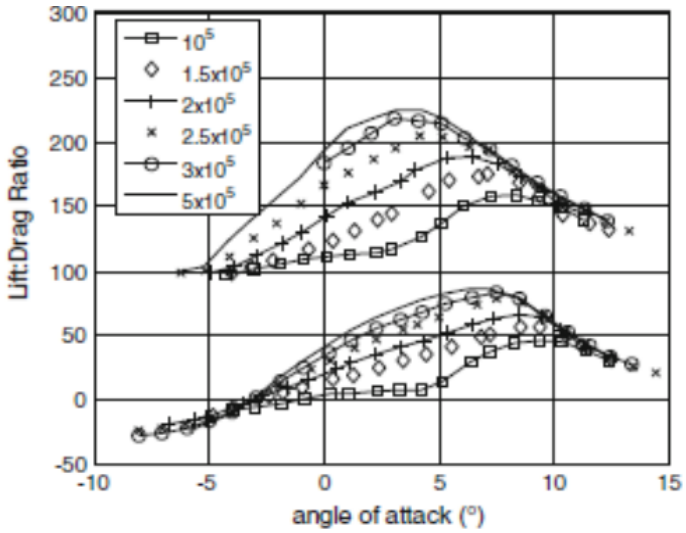

Figure 1.3: Lift-to-drag ratio of SG6040 (bottom) and SG6043 (top). The latter is shifted upwards by one unit [1].

For the majority of large wind turbines, the Reynolds number is greater than 500,000 near the tip region of each blade (the area where the most power is extracted from [12]) but a $500-\mathrm{W}$ wind turbine could operate at a minimum Reynolds number of 8,400 [1]. Therefore, small Reynolds number is a major problem for small-size wind turbines.

1.2.2 Starting Performance in Small Wind Turbines

To generate the maximum power by a wind turbine, the blades are twisted in such a way that the pitch angle near the tip is close to zero and increases when going toward the hub [1], for example, the pitch angle at the hub of a two-blade wind turbine investigated in [14] is 24.21°. So when the turbine is stationary, Figure 1.1 shows that α is very high even at the hub region. Therefore, the performance analysis

of the wind turbines at high angles of attack is very important when investigating their starting behavior. Unfortunately, there is not enough data for lift and drag coefficients at high α, although NACA 0012 and NACA 0015 are examined in [15]. Also, NACA 4415 and NACA 4418 are investigated in [16]. Based on the available data, lift and drag coefficients at high angles of attack could be approximated by

$$C_l = A\sin(2\alpha) \tag{1.2}$$

$$C_d = B - C\cos(2\alpha) \tag{1.3}$$

where A, B, and C depend on Re and type of the airfoil [1]. So if for example $A = B = C = 1$, then $C_l = 0$ and $C_d = 2$ when the angle of attack is 90° and so the lift-to-drag ratio is very small at high α. In addition, it can be shown that high angles of attack happen at low Reynolds numbers [1]; this makes the situation even worse and harder to produce enough lift to turn the blades. In addition, a wind turbine starts working only when the generated aerodynamic torque is more than the resistive torques of the generator coupled to the turbine including the cogging torque [17]. Starting performance is not a big problem for large wind turbines because they have a pitch control system that changes the pitch angle when the blades start rotating, and reduces the angle of attack significantly; this results in an efficient aerodynamic performance, but this control system is not usually used in small turbines because it is expensive. Neglecting the effect of Reynolds number, the generated aerodynamic torque in a wind turbine is proportional to the cube of the rotor radius whereas the decrease in the resistive torques of the generator is less than that, and so micro-turbines have five or even more blades to produce more torque [1].

In large wind turbines, the hub region is made of thick airfoils because this makes the turbine able to bear centrifugal forces and other stresses. Thicker airfoils have

poorer aerodynamic quality than the thinner ones, but the most power in a wind turbine is extracted near the tip region and the hub area is not very important in the power generation. On the other hand, it can be verified that the most starting torque is generated in the hub region [12]. So for a small-size wind turbine, a very special airfoil in the hub region is required such that it can generate enough torque, but also be able to resist against the centrifugal forces. This gives rise to another problem in manufacturing small wind turbines.

1.2.3 Small Wind Turbines: Technologies and Costs

The most important parameter that characterizes a wind turbine is power coefficient C_p defined as

$$C_P = \frac{P_{out}}{\frac{1}{2}\rho A V^3} \tag{1.4}$$

where P_{out} is the generated power by the turbine, and ρ and A are the air density and rotor area, respectively. It can be easily shown that the denominator in Equation (1.4) is the power of the air flowing through area A when its velocity is V. So the turbine can be considered as a system for which the input power P_{in} is

$$P_{in} = \frac{1}{2}\rho A V^3 \tag{1.5}$$

and the output power P_{out} is the generated power. For every system, the efficiency is defined as the ratio of the input to output powers. Therefore, the power coefficient of a turbine represents its efficiency.

Some difficulties associated with small wind turbines were described before. The power coefficient in small turbines is much lower than the large-size ones because of these problems. The cost of a large wind turbine installation is \$2/W of the generated electricity whereas this price is \$5/W for the small ones. So new technologies are

needed to manufacture small wind turbines to improve their efficiency and reduce the costs. As an example, some airfoils are specifically designed to be employed in small wind turbines. For instance, Professors Michael Selig (S) and Phillipe Giguere (G) at the University of Illinois at Urbana-Champaign designed SG airfoils. Detailed characteristics of these airfoils are explained in [18, 19]. MEL 081 is another type of airfoil that is used in small wind turbines [20].

1.3 Thesis Objective and Outline

As it was explained in the previous section, small wind turbines are more expensive than the large ones, and so a lot of research needs to be performed to improve the technologies in manufacturing these turbines. This research is devoted to the performance study and optimization of a novel type of small wind turbine called Zephergy [21]. Unlike conventional wind turbines, Zephergy consists of multiple rotors. Each rotor is called a stage or a wheel. The stages rotate independently from each other and generate electricity. More details about the idea are discussed in Section 2. Section 3 describes the design process of the airfoils. The experimental setup is investigated in Section 4. A method for calculating the output power of the wind turbine is described in Section 5. Results are provided and analyzed in Section 6. Finally, Section 7 includes summary, conclusions and recommendations for future work.

2. AN INTRODUCTION TO THE ZEPHERGY WIND TURBINE

2.1 Principle of Operation

As indicated in Figure 2.1, the Zephergy wind turbine is composed of multiple stages. The size of the stages decreases from the first wheel to the last one, i.e., the largest stage is the first one looking from the upstream. Each stage rotates independently of the other ones, and consists of two inner and outer rings. At each stage, a series of blades is distributed peripherally along the outer ring which is in turn connected to the inner ring by means of a number of spokes. The brown parts in the figure are magnets, and are attached to the inner rings. Electrical coils (the green parts) are mounted on the turbine shaft. The shaft is stationary, and when the stages rotate, the magnets turn around the coil and produce electricity. The wheels operate independently, and so the smaller stages can rotate at very low wind speeds because of their small inertia. For this project, the magnets and coils were supposed to be provided by a third party.

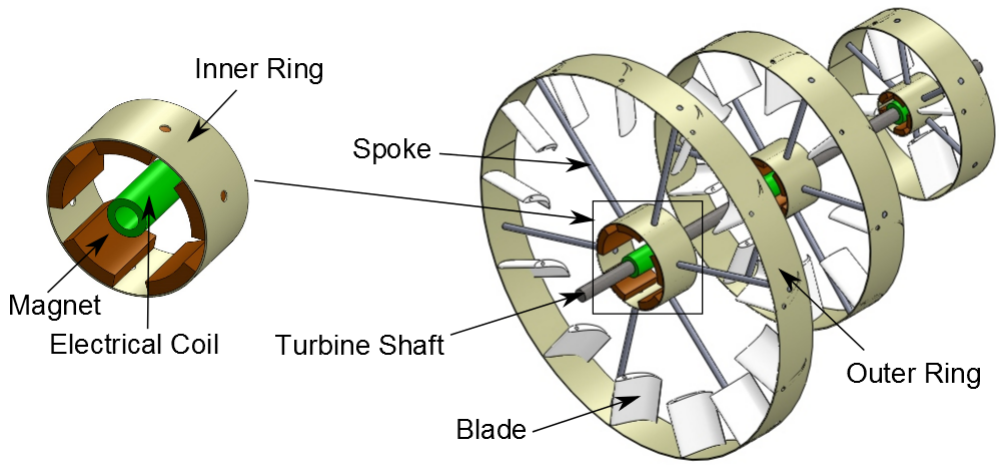

Figure 2.1: Initial design of the Zephergy wind turbine.

2.2 Research and Optimization Issues

There were several areas that needed to be investigated so that the turbine could be optimized and work at a high efficiency. The areas are itemized as follows:

- Blade shape, size, and arrangement
- Overlapping bladed areas of the adjacent stages or not
- Diameter variation from stage to stage
- Co-rotating or counter-rotating stages
- Addressing blade tip losses
- Aerodynamic interaction of the stages
- Minimization of the total angular momentum for easier yawing
- Possible use of a contraction shell to capture more wind energy

The design of the blades and the number of them for each stage was very critical. This issue was investigated based on the blade design and arrangement in turbomachinery. It was proposed that the adjacent stages did not overlap because it could reduce the performance of the stage that was in the back. At first, a three-stage turbine was chosen to be designed because a two-stage one did not address all the issues whereas a four-stage or more turbine added to the complexity and cost. The diameter variation was chosen based on the number of stages, the fact that there was no overlap between two consecutive stages, and the dimensions of the wind tunnel cross section that was 3×4 feet. It was also decided to have adjacent stages counter-rotating because of aerodynamic performance reasons and minimization of the angular momentum. Because the tips of the blades in Figure 2.1 are free, there

existed losses due to the lift-induced drag. A solution was adding another ring that connected the tips as shown in Figure 2.2.

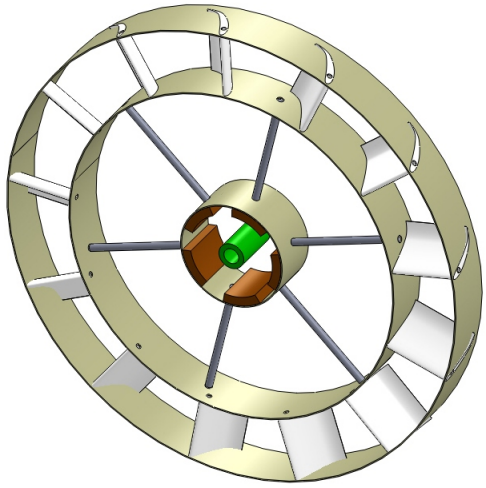

Figure 2.2: Modified design of one stage including the blade-tip connecting ring.

Another issue was using a contraction shell that is shown in Figure 2.3. The figure is comprised of the turbine and a shell that is attached at the inlet. This feature has two major benefits:

- The air is accelerated because of the contraction, and so the turbine could extract more power because the power is proportional to the cube of the wind speed.
- The contraction conditions the flow in the sense that it cuts down on turbulent intensities.

At first, it was supposed that two graduate students would work on the project, but to save money, it was decided then to reduce the number of students to one.

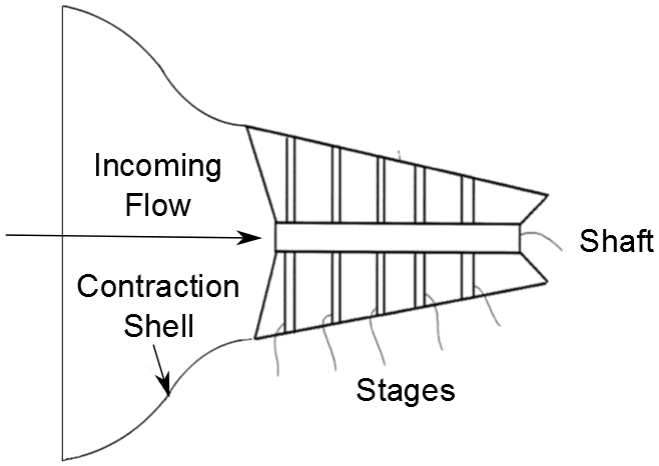

Figure 2.3: Contraction shell added to the turbine inlet.

Instead, a group of five graduate students worked on the project as part of a graduate class (AERO 629) for one semester. A summary of what they did is provided in the next part.

2.3 Previous Work on the Project

The turbine designed by the AERO 629 group had three stages. The magnets were not provided by the third party, and so the turbine did not have the innermost ring in Figure 2.2. From now on, the outermost ring in the figure is called the outer ring, and the blade-tip connecting one is named the inner ring. The blades were mounted between these two rings. The outer ring of the first stage was designed in such a way that its diameter was 18" so that the turbine could fit in the 3×4 feet wind tunnel and minimize blockage effect. There was no overlap between the adjacent stages, and the goal was to maximize the power extraction from the wind; so the stages were designed in such a way that there was no gap between the inner ring of one stage and the outer ring of the next wheel. The span (the distance between the inner and outer rings of each stage) was set at 2.5", so that a small gap (1.5")

remained between the innermost ring, i.e., the inner ring of the third stage, and the shaft of the turbine. The width of each stage was set at 2". The airfoil used in the turbine was the same for all stages. It was a highly modified NACA 9715. The Blade design and choosing its pitch angle were accomplished based on the analysis conducted using X-FOIL at Reynolds number of 15000. The number of blades at each stage was determined based on the simple rule of thumb in turbomachinery: the blades were spaced by a distance equal to double their chord length. Because the magnets were never provided, the group had to use electrical motors to generate electricity. Only one motor was available at the time, and so it was decided to mount all three stages on a common shaft (Figure 2.4) which was in turn connected to the

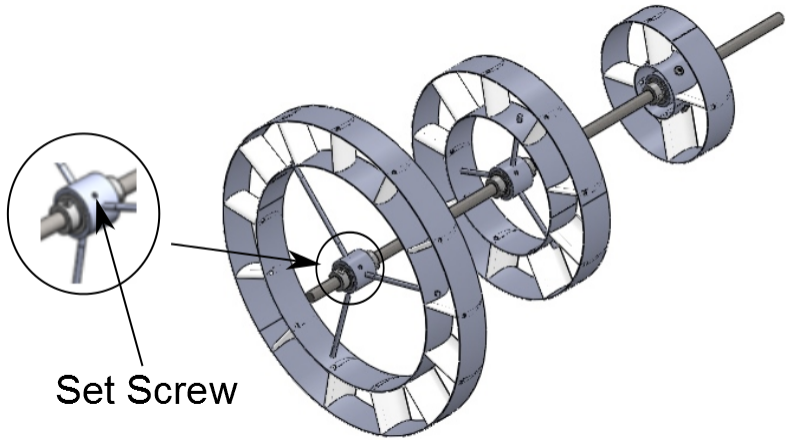

Figure 2.4: Three stages of the Zephergy wind turbine mounted on a common shaft.

shaft of the motor at its end. Each stage was attached individually to the shaft by the set screws shown in Figure 2.4, and its performance was examined. A cowling was also designed for the turbine to be used as a contraction shell. Separate parts of the turbine and the assembly are shown in Figures. 2.5a and 2.5b, respectively.

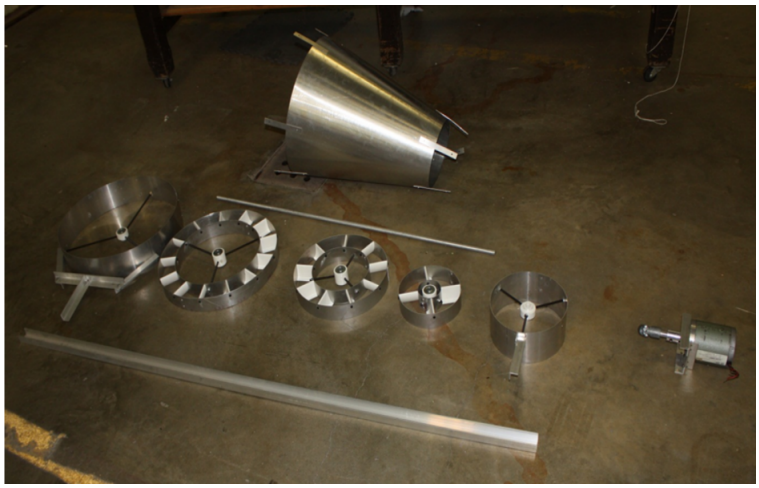

(a) Individual parts

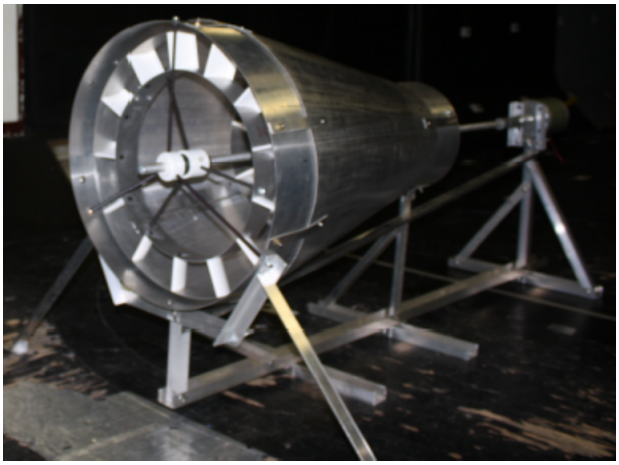

(b) Assembly

Figure 2.5: Three-stage Zephergy wind turbine designed by the AERO 629 group.

The tests were done in the wind tunnel at different wind speeds, and indicated very poor results. For example, the first stage generated only 1.6 W at a wind speed of 45 mph. The reason was a large streamline deflection at the entrance of the turbine as shown in Figure 2.6. Smoke visualization technique was used to take the picture. The reason for the deflection was that the cowling did not work as a contraction shell; the major difference between the cowling designed by the AERO 629 group

Figure 2.6: Flow visualization at the turbine inlet.

(Figure 2.7) and the contraction shell in Figure 2.3 was the head part of the cowling that caused the deflection. Some experiments were done after removing the cowling and the results were disappointing again. For instance, the best power coefficient obtained for the first stage was below 8%. This indicated that the airfoils were not efficient enough.

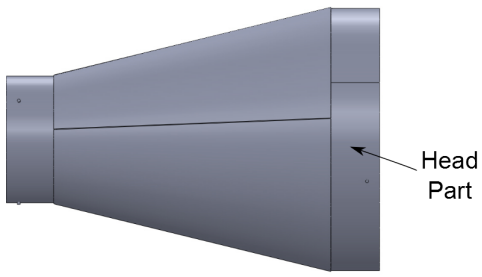

Figure 2.7: Cowling designed by the AERO 629 group.

2.4 Current Work

Unfortunately, the magnets and coils were not provided by the third party. Consequently, each stage had to be mounted on a separate shaft and connected to a different electrical motor. Because the space in the test section was limited, a 2-stage Zephergy wind turbine was studied. At first, blades were designed based on turbomachinery. The blade design and number were different for the two stages. Then, each stage was tested individually and its performance characteristics were derived and analyzed. Finally, both stages were placed in the test section and different experiments were run.

3. BLADE DESIGN AND ARRANGEMENT

The operating principles of jet-engine turbines were utilized in the process of blade shape design and arrangement. The first part of this section is devoted to an introduction to some basic concepts of turbomachines. Characteristics of the blades used in the Zephergy wind turbine are investigated in the second part.

3.1 Velocity Vectors and Diagrams

When some fluid flows through a rotating part of a turbine (rotor), a coordinate system composed of three basis vectors is defined as follows: the first coordinate is parallel to the axis of rotation, the second one is considered parallel to the radius of the rotor, and the third coordinate is defined as the tangential vector to the rotating stage [2]. The axial, radial, and tangential velocity components of the fluid are shown in Figure 3.1 at two points.

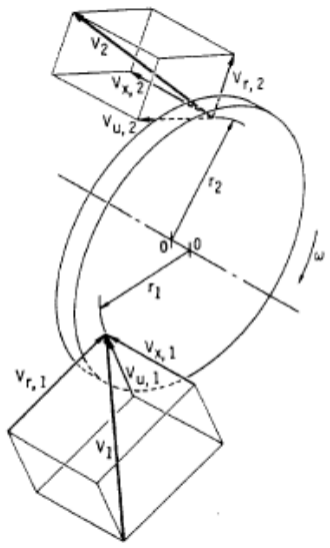

Figure 3.1: Velocity components of the fluid passing through a turbine rotor [2].

The three basis vectors form three different planes. The velocity of the fluid and its variation in different directions are important variables in the analysis of a turbine performance and energy transfer. Velocity diagrams and other calculations are investigated in the three planes. The radial-tangential plane is used if the flow is radial, for example at the inlet to a radial-flow turbine, but in an axial-flow turbine such as a wind turbine that the flow is predominantly axial, the axial-tangential plane is utilized. The change in the axial component of the velocity results in an axial force called thrust. If the radial component of the velocity changes, a radial bearing load is generated. None of the radial and axial components of the velocity could affect the angular momentum of the fluid. The change in the angular motion of the rotor that results in the energy transfer from the fluid to the rotor is provided only by the change in the tangential velocity component of the fluid. The change could happen in either magnitude or radius of the component.

The relative velocity of the fluid to the rotating blade must be considered when the turbine operation is studied. This velocity is defined as

$$\text{Relative velocity} = \text{Absolute velocity -Blade velocity} \tag{3.1}$$

It is obvious that the blade velocity has only the tangential component. In a velocity diagram, the variations in the circumferential direction are not considered. In other words, the variation of the parameters from blade to blade is ignored. This type of calculation is called an axisymmetric analysis [2]. Both absolute and relative velocities have to be included in a velocity diagram.

The velocity diagram in Figure 3.2 is drawn in the axial-tangential plane, and shows Equation (3.1) and the two components of the absolute and relative velocities. The relative, absolute, and blade velocity vectors are represented by $\vec{W}$, $\vec{V}$, and

$\vec{U}$, respectively. U, V and W are the magnitudes of the vectors $\vec{U}$, $\vec{V}$ and $\vec{W}$,

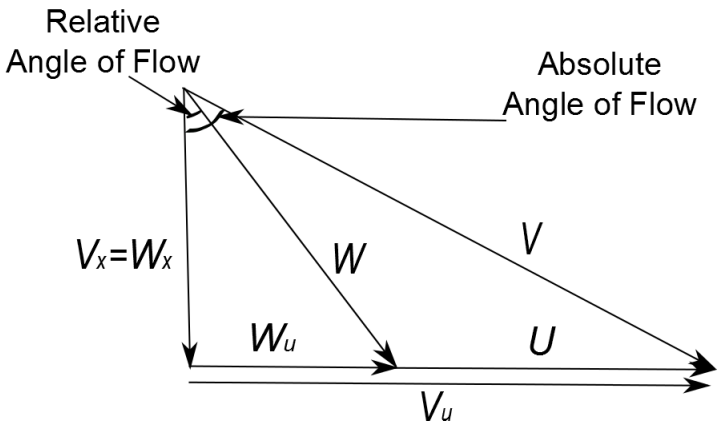

Figure 3.2: Velocity vector diagram in the axial-tangential plane [2].

respectively. The axial components of the absolute and relative velocities are shown by V_x and W_x, respectively whereas V_u and W_u indicate the tangential components. U is equal to $r\omega$, where r is the radius at which the blade is located, and ω is the angular velocity of the blade.

A typical blade section is indicated in Figure 3.3. Camber line is the mean line of the blade profile, and chord line is the straight line that connects the trailing and leading edges of the blade. The stagger angle indicated in the figure is defined as the angle between the chord line and the axial coordinate. In other words, the stagger angle determines how the blade has to be installed on the rotor of a turbine with respect to the axis of rotation.

A velocity diagram is analyzed at the upstream and downstream of a blade as indicated in Figure 3.4. It is assumed that the velocity at either upstream or downstream has no radial component, and so the diagram is drawn in the axial-tangential plane. In this thesis, the axial and tangential basis vectors are

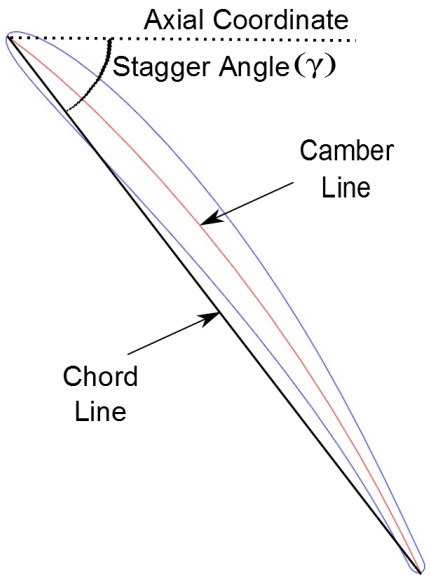

Figure 3.3: Typical blade section.

shown by $\vec{i}$ and $\vec{j}$, respectively. At the inlet, the fluid flows with an absolute velocity of $\vec{V_1}$, and the blade rotates with a tangential velocity of $\vec{U_1}$. So the relative velocity of the fluid to the blade section is $\vec{W_1}$. The angle of $\vec{W_1}$ with respect to the positive direction of the axial coordinate is β_1. This angle is called inlet flow angle. The angle between the tangential line to the camber line at the leading edge and the axial coordinate is selected equal to the inlet flow angle. In a similar manner, $\vec{V_2}$, $\vec{U_2}$, and $\vec{W_2}$ are defined. It is desired that the flow leaves the blade tangentially to the camber line, i.e. with the outlet flow angle β_2, but the real angle of the flow is β_{2f} that is named metal angle. If the blade section is located at the same radius, the tangential velocities at the inlet and outlet are the same, i.e., $U_1 = U_2$.

As it was mentioned earlier, the change in the tangential component of the fluid velocity causes the transfer of energy from the fluid to the rotor. So a designer needs to design a blade section in such a way that the blade induces changes to the tangential component of the relative velocity as much as possible. This critical point

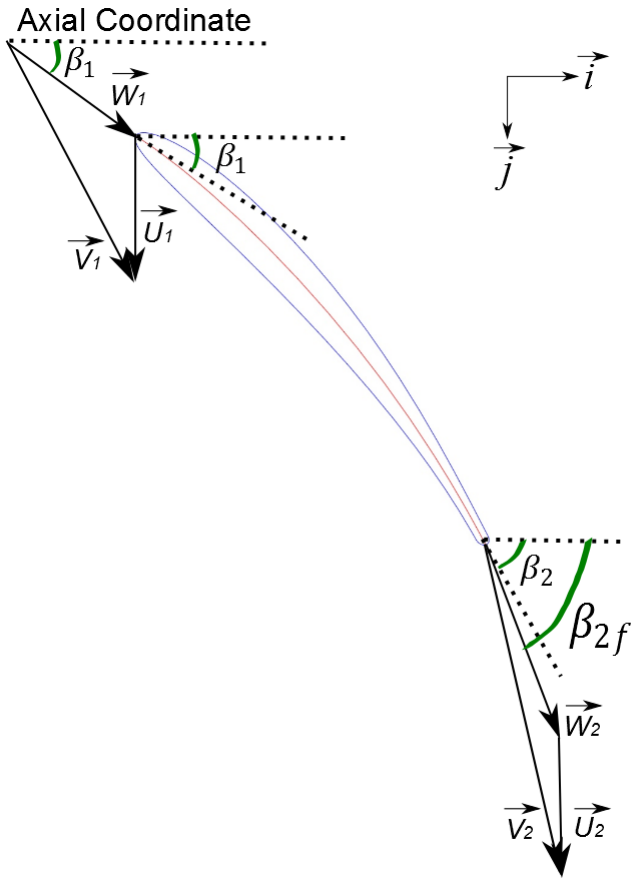

Figure 3.4: Velocity vector diagrams at upstream and downstream of a blade.

is employed in the process of the blade design described in the next part.

3.2 Blade Design Process

The wind turbine in this project was comprised of two stages that rotated in opposite directions. The blades used in one stage were different from those employed in the other one. Each blade consisted of three section areas: hub, middle, and tip (Figure 3.5). The hub and tip areas were the innermost and outermost regions of the blade, respectively.

The first step in the blade design process was designing the middle section.

Drawing the camber line was the fundamental part of designing the section profile. The operating conditions of each stage, i.e., the wind velocity, the radius of the stage,

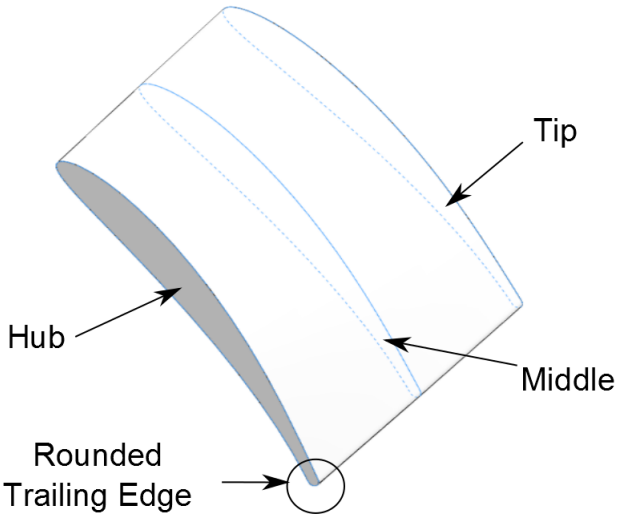

Figure 3.5: Three section areas of a blade.

and the angular velocity were required for this purpose. The mentioned parameters were selected by the designer. So $\vec{V_1}$ and $\vec{U_1}$ in Figure 3.4 were known for each stage: $\vec{V_1}$ was the wind velocity vector that was supposed to have no tangential component and was equal to $V_1\vec{i}$ where V_1 was the magnitude of the velocity. U_1 was the tangential velocity of the middle section area, and was equal to the radius at which the section was located multiplied by the angular velocity of the stage. Consequently, $\vec{W_1}$ and β_1 were derived. Then, β_2 and the stagger angle were selected based on the experience of the designer. The stagger angle was set at 45° for both stages. Because the width of each stage was chosen as 2" by the AERO 629 group,

according to Figure 3.3, the chord length was selected as 2.7661" because

$$c = \frac{2"}{\cos(45°)} = 2.7661"$$

The design process started from point A in Figure 3.6. Then, point B was obtained by means of the stagger angle and the chord length as indicated in the figure. The inlet and outlet flow angles of the blade, i.e., β_1, and β_2 were utilized then to achieve the third point, i.e., C in Figure 3.7. Finally, the Beizer curve that is a parametric

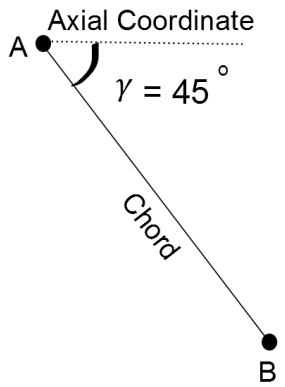

Figure 3.6: Points A and B in the process of the camber line design.

curve and is widely used in computer graphics was employed to draw the camber line as it is shown in Figure 3.8. For more information about the Beizer curve see [22].

To build the middle section profile, it was necessary to add thickness to the camber line. NACA 0012 profile description [23] was employed to do so. All NACA airfoils have a sharp trailing edge, and so for the manufacturability, it was decided to round the trailing edge as it is shown in Figure 3.5.

The hub and tip regions were not located at the same radius as the middle area. This resulted in the different tangential velocity components and relative velocities.

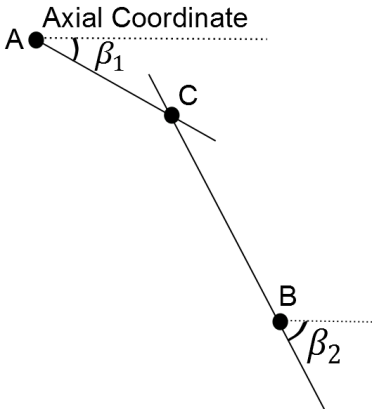

Figure 3.7: Points A, B, and C in the process of the camber line design.

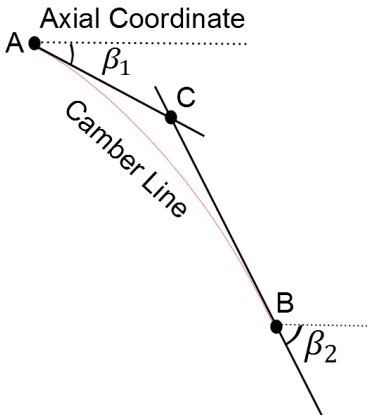

Figure 3.8: Camber line design by means of the three points A, B, and C, and Beizer curve.

So the inlet flow angles were different at these areas from those in the middle section. To obtain the airfoil profile at the hub and tip, the middle profile was simply rotated around its central point as it is shown in Figure 3.9 because the inlet flow angles were different at these areas. In other words, the blade was twisted. The number of blades for each stage was determined based on the designer's experience. The blades were made from ABS plastic in a rapid prototyping (RP) machine.

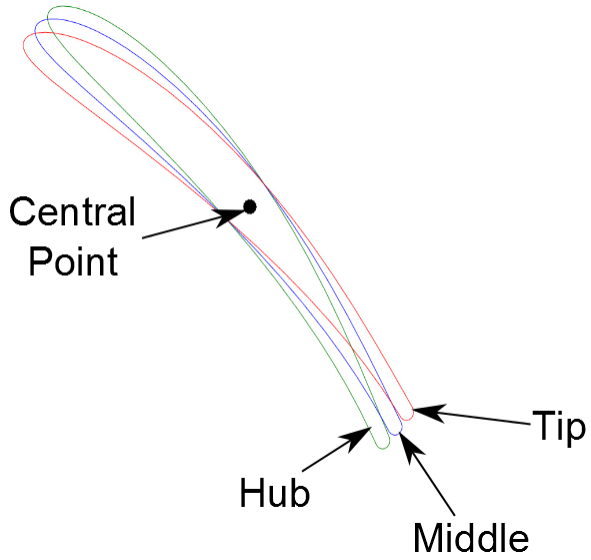

Figure 3.9: Rotation of the middle profile around its central point to obtain the tip and hub profiles for a blade.

3.2.1 Characteristics of the Bigger Stage Blade

In the initial design of the turbine performed by the AERO 629 group, the outer and inner rings of the bigger stage had diameters of 18" and 13", respectively. So the blade section areas at the hub, middle, and tip had radii of 6.5", 7.75", and 9", respectively. The wind velocity at which the stage was supposed to operate was chosen as 17 m/s. The angular velocity was set at 17 rad/s. So at the middle section area

$$\vec{V_1} = 17\vec{i}\ \text{m/s} \tag{3.2}$$

$$\vec{U_1} = 3.3465\vec{j}\ \text{m/s} \tag{3.3}$$

$$\vec{W_1} = 17\vec{i} + 3.3465\vec{j}\ \text{m/s} \tag{3.4}$$

$$\beta_1 = 11.1364^\circ \tag{3.5}$$

The outlet flow angle, β_2 was selected as 67° based on the designer's experience. The tangential velocity component and inlet flow angle changed to 2.8067 $^{m}/_{s}$ and 9.3750° at the hub section, and 3.8862 $^{m}/_{s}$ and 12.8766° at the tip region, respectively. The number of blades for this stage was set at 20.

3.2.2 Characteristics of the Smaller Stage Blade

The outer and inner rings of the smaller stage had diameters of 13" and 8", respectively. So 4", 5.25", and 6.5" were the radii of the hub, middle, and tip regions, respectively. The wind velocity and angular velocity of the wheel were set at 16 $^{m}/_{s}$ and 35 $^{rad}/_{s}$, respectively. Because this stage was smaller than the other one, it was expected to rotate faster, and that was why its angular velocity was selected about twice that of the bigger stage. So at the middle section area

$$\vec{V_1} = 16\vec{i}\ ^{m}/_{s} \tag{3.6}$$

$$\vec{U_1} = 4.6673\vec{j}\ ^{m}/_{s} \tag{3.7}$$

$$\vec{W_1} = 16\vec{i} + 4.6673\vec{j}\ ^{m}/_{s} \tag{3.8}$$

$$\beta_1 = 16.2623^\circ \tag{3.9}$$

The outlet flow angle, β_2, was chosen as 60° by the designer. The tangential velocity and inlet flow angle were 5.7785 $^{m}/_{s}$ and 19.8575° at the tip region, and 3.5560 $^{m}/_{s}$ and 12.5303° at the hub area. The number of blades was set at 13.

4. EXPERIMENTAL SETUP

The Zephergy wind turbine consisted of two stages. The first goal of the experiments was to derive the performance characteristics of each stage when the other one was not in the tunnel. The second goal was to investigate how the performance of each stage was affected by the other one when both stages were mounted in the tunnel. This section describes the experimental setup for running one and two stages in the 3×4 feet wind tunnel at Texas A&M University. All components of the experiments as well as the assembly setup are investigated in different subsections.

4.1 Rings

Although the inner and outer rings of the stages were designed by the AERO 629 group, new rings were required for the turbine. The reason was that the new airfoils described in the previous section were twisted and did not fit between the designed inner and outer rings, and so more span was required. The reader is reminded that span was the distance between the inner and outer rings. So for example, the diameters of the outer and inner rings for the bigger wheel were changed from 18" and 13" to 19" and 13.5", respectively. The width of the rings was changed from two to three inches as well. The rings were built from aluminum sheets with a thickness of 0.125". The reason for choosing this sheet was that aluminum was light and minimized the angular momentum but on the other hand, a very thin aluminum sheet might not be able to tolerate the high forces at high wind speeds.

In this subsection, designing the outer ring of the bigger stage is described in details. Other rings were designed in the same manner. The goal is to provide the engineering drawing of the aluminum sheet for the machinist.

4.1.1 Outer Ring of the Bigger Stage

Since the aluminum sheet had a specific amount of thickness (0.125"), the ring could be considered to have two inner and outer circles as indicated in Figure 4.1. The numbers mentioned before as the diameters of the rings refer to the diameters of the outer circles, for instance, the outer circle in the outer ring of the bigger stage had a diameter of 19".

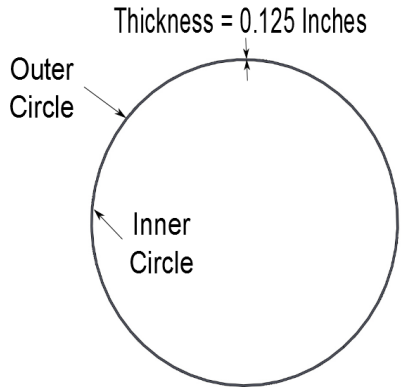

Figure 4.1: Outer and inner circles of a ring.

After investigating the assembly of the whole stage, the radius of the outer ring was a little bit reduced to optimize the gap between each blade and the ring (Figure 4.2), and was changed from 9.5" to 9.47". So the radius of the inner circle was 9.345". As a result, the perimeters of the outer and inner circles were 59.5018" and 58.7164", respectively. The length of the aluminum sheet was the average of these perimeters that was 59.1091". The precision of the lathe and milling machines were up to the third decimal place; so the length was set at 59.109". The bigger stage had 20 airfoils, and so 20 holes were needed on the ring to attach the blades to the ring by means of screws. The distance between the centers of each two adjacent holes was then

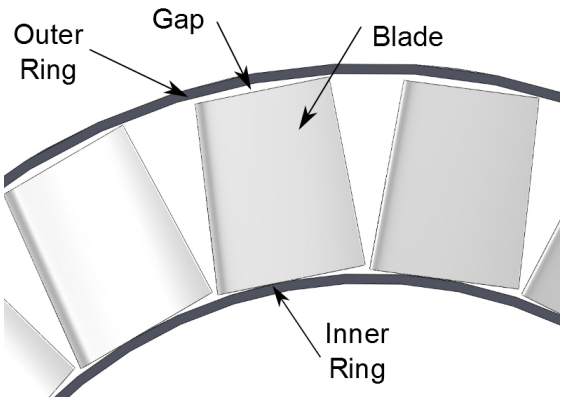

Figure 4.2: Blades between the inner and outer rings.

2.9554". It was impossible for the machinist to make such a distance because as it was mentioned, the machines were precious up to the third decimal place. So it was decided to set the distance at 2.96". This resulted in the change of the sheet length to 59.2" because $2.96 \times 20 = 59.2$. So the radius of the outer circle was changed to 9.4845". The sheet was going to be bent to form the ring, and so the two ends of the sheet overlapped (Figure 4.3). The amount of this overlap was set at 0.7". Therefore, the total length of the aluminum sheet was 59.9". The drawing of the

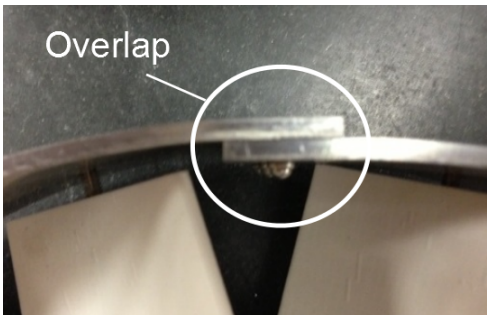

Figure 4.3: Overlap between the two ends of the aluminum sheet.

sheet is indicated in Figure 4.4. The blades were attached to the rings by means of

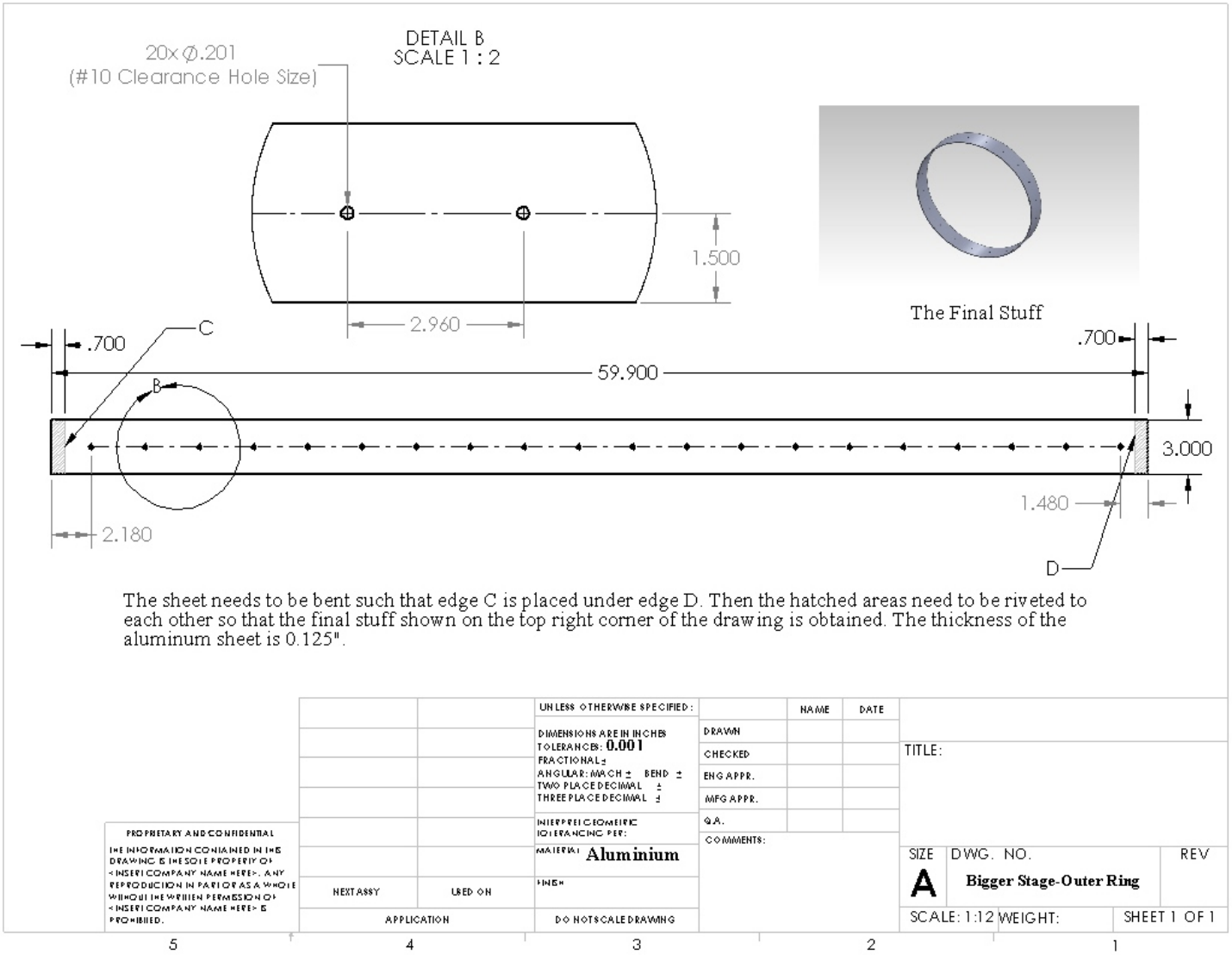

Figure 4.4: Engineering drawing for the outer ring of the bigger stage.

8-32 thread pan-head Phillips machine screws, and so the hole size could have been chosen #8 clearance hole size instead of #10 in the drawing.

4.1.2 Other Rings

The inner ring of the bigger stage and both rings of the smaller stage were designed in a similar manner as the outer ring of the bigger stage. The only difference for the inner rings was additional holes that were added because of the spokes. The radii of the outer circle in the inner ring of the bigger stage and the outer and inner rings of the smaller one were 6.7470", 6.6213", and 3.8488", respectively. Also the distance between the centers of each two adjacent holes for these three rings were 2.10", 3.17", and 1.83", respectively. The engineering drawings of the rings are shown in APPENDIX A.

4.2 Stage Assembly

The bigger stage and its different components are indicated in Figure 4.5. The stage was connected to the shaft by the spokes and set screws. The spokes were $1/4" - 20$ threaded rods. They were attached to the inner rings by hex nuts. The other end of each spoke was mounted in the housing. The housing was made in the RP machine, and was made of ABS plastic. Two ball bearings were located at the two ends of the housing. The bearings were for a shaft diameter of $5/8"$. They were of the steel flanged double sealed type, and had an outer diameter of $1\,3/8"$. The stage was connected to the shaft when the set screws were tightened. The screws had a style of socket head, and were $1/4" - 20$ fully threaded.

4.3 Pillars

The turbine shaft was held by the structure indicated in Figure 4.6. The reason for using two pillars was to make sure that the turbine shaft did not bend during the

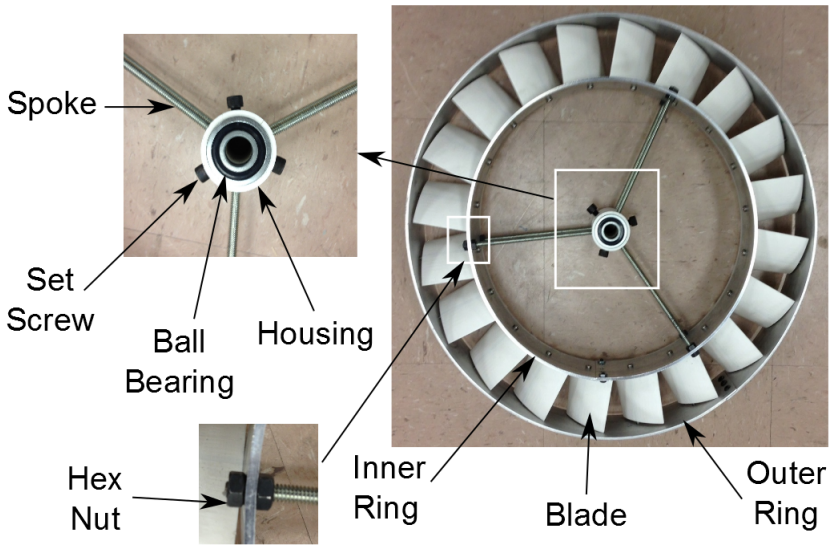

Figure 4.5: Bigger stage of the Zephergy wind turbine: assembly and different parts.

operation of the turbine. The dimensions of the head part were $2" \times 1.5" \times 2.5"$.

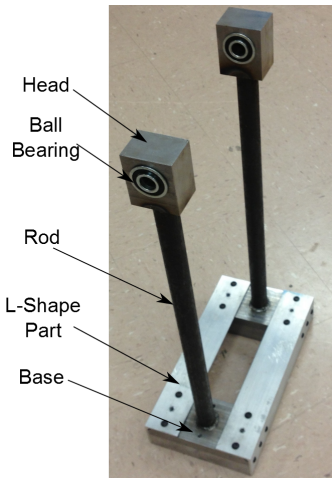

Figure 4.6: Pillar structure.

The distance between the inner surfaces of the two heads was $7.5"$ (Figure 4.7). The engineering drawings for different parts of the pillar structure are provided in

APPENDIX A. The ball bearings used in the heads were the same as those used in

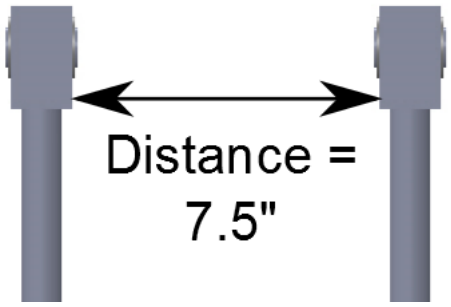

Figure 4.7: Distance between the two pillars.

the stage assembly. Each head part had two bearings. The radius of the rod was 1". Its total length was 18.75", but 0.25" and 0.5" of this length were welded inside the head and base, respectively; so the visible length was 18". The base had dimensions of 6" × 3" × 2". All parts other than the L-shape ones were made of steel to prevent the turbine from vibrating (the structure used by the AERO 629 group vibrated severely at high wind velocities.). The L-shape parts were made of aluminum. They were utilized to connect the two bases. The bases were attached to the floor of the test section. The floor had a thickness of about 1". Screws with a length of 3½" were used for attaching.

4.4 Electrical Motor

To extract energy from the wind, the turbine had to be connected to an electrical motor which in turn supplied a circuit. At first, the plan was to test the stages at a wide range of the wind speed including 25 $^{m}/_{s}$. Also, performance of the stages was overestimated and it was believed that each stage would have a power coefficient of more than 0.5, and so the generated power from the bigger stage at that wind speed

would be more than 400 W because

$$P = C_p(\frac{1}{2}\rho A V^3) = 0.5 \times \frac{1}{2} \times 1.2041 \times \pi \times 0.0271 \times 25^3 \approx 400$$

where ρ was the density of the air and equal to 1.2041 $^{m^3}/_{kg}$ at 20° C that was the typical temperature in the 3×4 feet wind tunnel. The area between the outer and inner rings was A. So a 1-hp motor would be a good choice. Working with a DC motor was simpler than an AC one. Therefore, a 1-hp DC motor was used. The motor was of a permanent magnet (PM) type. The reason of choosing this type will be explained in the next section. Some companies were contacted to order the machine, but unfortunately, they only accepted orders of minimum five motors. Finally, a heavy (36 lbs.) motor was ordered from Grainger. The motor was produced by Dayton and its model number was 4Z378C. The nominal (full-load) characteristics of the motor are shown in Table 4.1.

Current	5 A
Voltage	180 V
Angular Velocity	1725 rpm
Torque	586 oz-in
Power	1 hp

Table 4.1: Nominal characteristics of the Dayton electrical motor.

The diameter of the motor shaft was $^5/_8$" that was the same as the diameter of the turbine shaft. A helical beam shaft coupling with the bore sizes $^5/_8$" was used to connect the two shafts.

As it was mentioned before, the electrical motor was heavy. So an adjustable-height steel table was used to hold it in the test section (Figure 4.8).

The height of the table was set at 18". In this situation, the distance between the center of the machine shaft and the test section floor was 21.5". Each leg of the table was attached to the floor by a L-shape aluminum part and two wood screws.

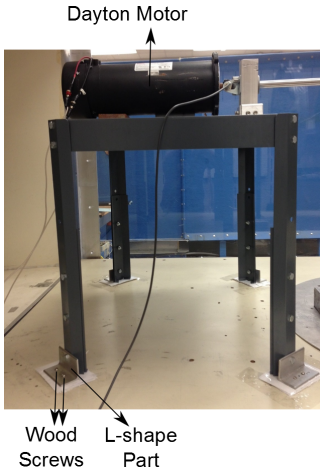

Figure 4.8: Steel table holding the Dayton electrical motor in the test section.

4.5 Proximity Sensor

A common method to measure the rotational velocity of a shaft is using a shaft encoder. To save money and reduce complexity, a proximity sensor (Figure 4.9) was employed in the experiments instead of a shaft encoder. It was a sensor that could detect the presence of nearby objects without any physical contact [24]. Various types of proximity sensors are used to sense different targets. For instance, capacitive photoelectric sensors detect plastic materials whereas the inductive type is suitable for metal targets. The maximum distance that a proximity sensor can detect is called normal range or sensing distance [24]. The sensor used in this project was OMRON E2E2-X3D1 that was an inductive one with a sensing distance of three mm.

A proximity sensor needs an electrical circuit to operate. Figure 4.10 shows the

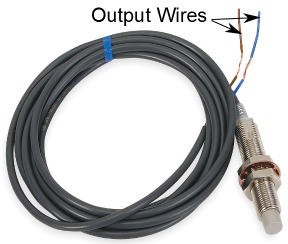

Figure 4.9: Proximity sensor.

output circuit of the sensor. Brown and blue in the figure are two output wires of the sensor and are shown in Figure 4.9. The power supply must provide some voltage between 12 and 24 VDC. The output current can be 3 to 100 mA. The current and voltage were set at 60 mA and 18 V, respectively. So the load was a $300 - \Omega$

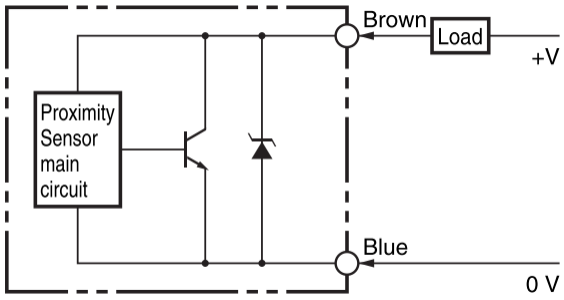

Figure 4.10: Output electrical circuit of a proximity sensor.

resistance because

$$R = \frac{V}{I} = \frac{18\,\text{V}}{0.06\,\text{A}} = 300\,\Omega$$

A proximity sensor could be normally open (NO) or closed (NC). When a NO sensor does not detect any object, the electrical circuit is open, and no current passes through the load. A normally closed sensor operates in an opposite manner. The sensors used in the experiments in this thesis were normally open. The standard

target for the sensors was an $12 \times 12 \times 1$ mm iron part. The object used in the experiments was an iron hex nut. The nut was fastened to the shaft of the motor by a piece of electric tape, and the sensor was installed on the steel table close to the shaft as shown in Figure 4.11. The sensor measured the angular velocity as follows:

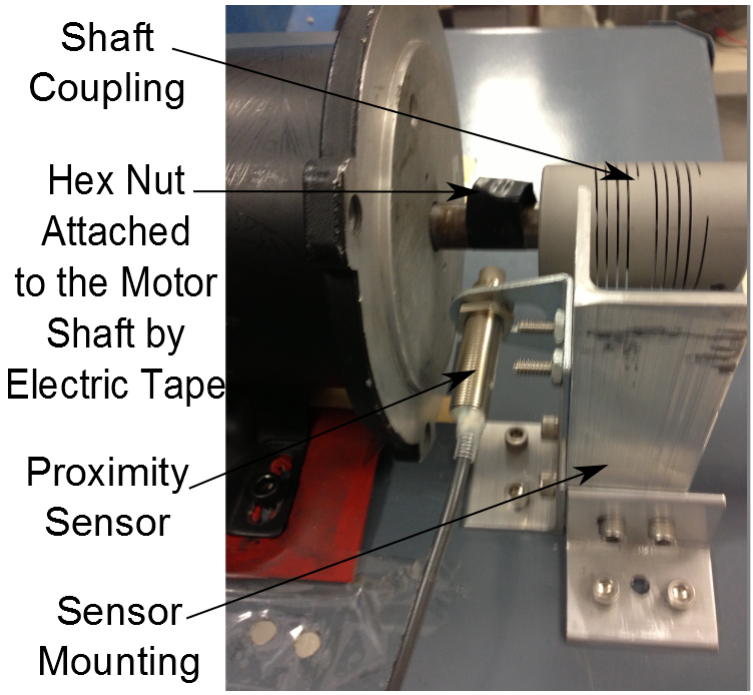

Figure 4.11: Proximity sensor installed on the table.

at each turn of the motor shaft, the iron nut was within the sensing distance for a specific amount of time. During that time, the circuit was closed and the current passed through the load in Figure 4.10, and generated some voltage. An oscilloscope with its probe connected to the two ends of the resistor indicated that voltage. So a square wave was observed on the oscilloscope. Measuring the period of the wave (T) gave the angular velocity according to $\omega = {}^{2\pi}/_{T}$.

4.6 Experimental Setup in the Test Section

Figure 4.12 indicates the experimental setup in the test section to investigate one stage.

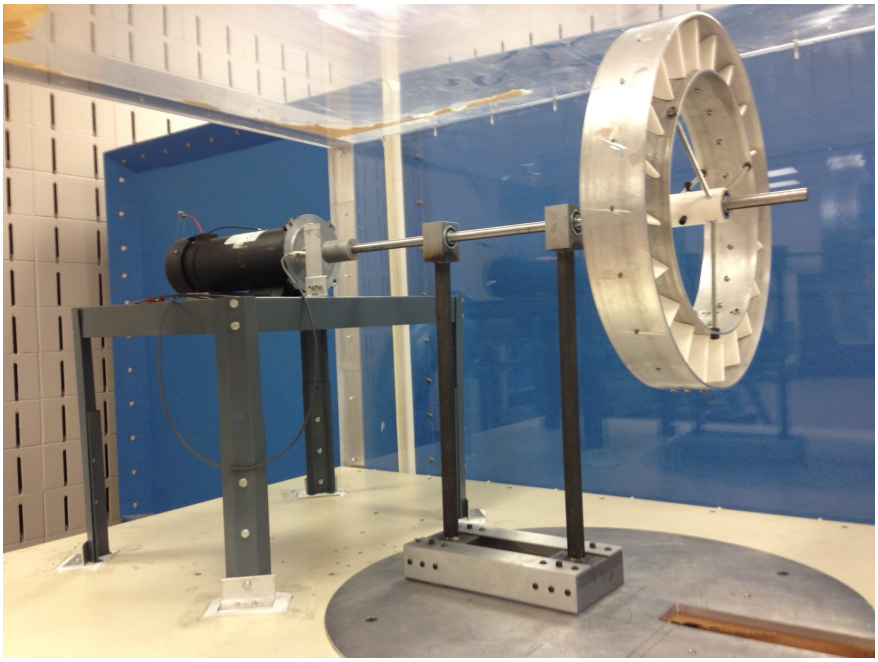

Figure 4.12: Experimental setup in the test section for running one stage of the Zephergy wind turbine.

4.7 Output Electrical Circuit

The most important parameter that indicates the efficiency of a wind turbine is the power coefficient. Apparently, the coefficient depends on the aerodynamics of the blades which is in turn dependent on the angle of attack. An important parameter that determines the angle of attack is the tip speed ratio that is indicated by λ, and is defined as the ratio of the circumferential velocity of the blade tips to the wind

speed [1], i.e.,

$$\lambda = \frac{\omega R}{V} \tag{4.1}$$

such that ω is the angular velocity of the turbine, R is its rotor radius, and V is the wind speed. So the tip speed ratio has a major effect on the power coefficient, and a curve that shows the change of the power coefficient versus the variation of the tip speed ratio is important. The goal of the experiments in this project was to derive this curve for each stage at different operating conditions. In other words, the goal was to determine the power coefficient at different tip speed ratios.

To extract energy from the wind an electrical load was required to be connected to the motor. The simplest type of a load was a resistor. Changing the resistor would change the output current of the motor as well as its angular velocity. So if the turbine was tested at a constant wind velocity, different tip speed ratios were achieved by varying the resistance in the electrical circuit. So a rheostat that is a variable resistor was needed. A $500-\Omega$ rheostat in addition to a dial and a knob (Figure 4.13a) were ordered from Ohmite. The maximum current that could pass through the rheostat and did not damage it was 1 A.

When testing the first stage at different wind speeds, it was observed that the tip speed ratio changed much faster at lower resistances ($0-10\ \Omega$) compared to the changes at the higher resistances. Setting the $500-\Omega$ rheostat on some resistance between 0 and 10 Ω was not easy because turning the knob by a small amount resulted in a high change in the resistance. Furthermore, at low resistances the current was higher than 1 A that could damage the rheostat. So a $10-\Omega$ rheostat (Figure 4.13b) was added to the circuit in series. A toggle switch was also connected to the $500-\Omega$ rheostat in parallel to keep it out of the circuit at high currents. Also, a $500-\Omega$ power resistance connecting to another toggle switch in parallel was

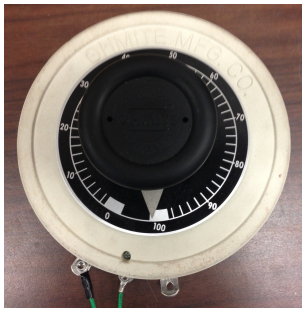

(a) $500-\Omega$ rheostat.

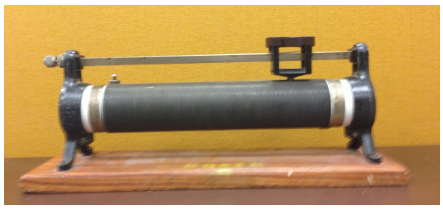

(b) $10-\Omega$ rheostat.

Figure 4.13: Rheostats.

added to the circuit in series so that a broad range of resistances was achievable. Two multi-meters were also used in the electrical circuit: one in series with the resistors to measure the current, and one in parallel with them to measure the voltage applied to them. The current was utilized to find the output power of the turbine. The voltage divided by the current gave the total resistance in the circuit except for the internal resistance of the motor. The schematic of the electrical circuit is indicated in Figure 4.14.

At each test, the wind speed was set at a specific amount. At first, both switches in Figure 4.14 were closed and so the only load in the circuit was the $10-\Omega$ rheostat. The electrical motor had an internal resistance R_0. By moving the knob of the $10-\Omega$ rheostat, the resistance in the circuit was increased from R_0 to $10+R_0$. Increasing the resistance reduced the current, and raised the angular velocity. At some random resistances, the rotational velocity was measured by the proximity sensor, and the tip

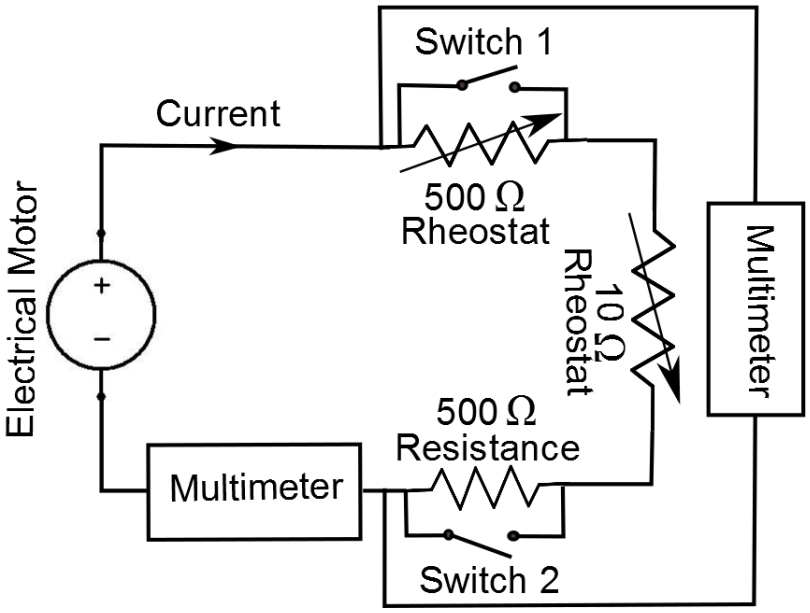

Figure 4.14: Schematic of the electrical circuit connected to one stage of the Zephergy wind turbine.

speed ratio was determined. To determine the power coefficient, the output power of the turbine was calculated by measuring the current and angular velocity. The method of calculating the output power is discussed in details in the next section. Then, Switch 1 was toggled to open and the $500 - \Omega$ rheostat was added to the circuit. By turning its knob, the resistance was varied from $10 + R_0$ to $510 + R_0$, and more points of the $C_p - \lambda$ curve were achieved. If additional points on the curve were required, Switch 2 was toggled to open too. In this case, the resistance could change from $510 + R_0$ to $1010 + R_0$ again by means of the $500 - \Omega$ rheostat.

Figure 4.15 shows the test section and a table beside it on which the components of the two electrical circuits (one for the operation of the proximity sensor and one for extracting energy from the turbine) were placed.

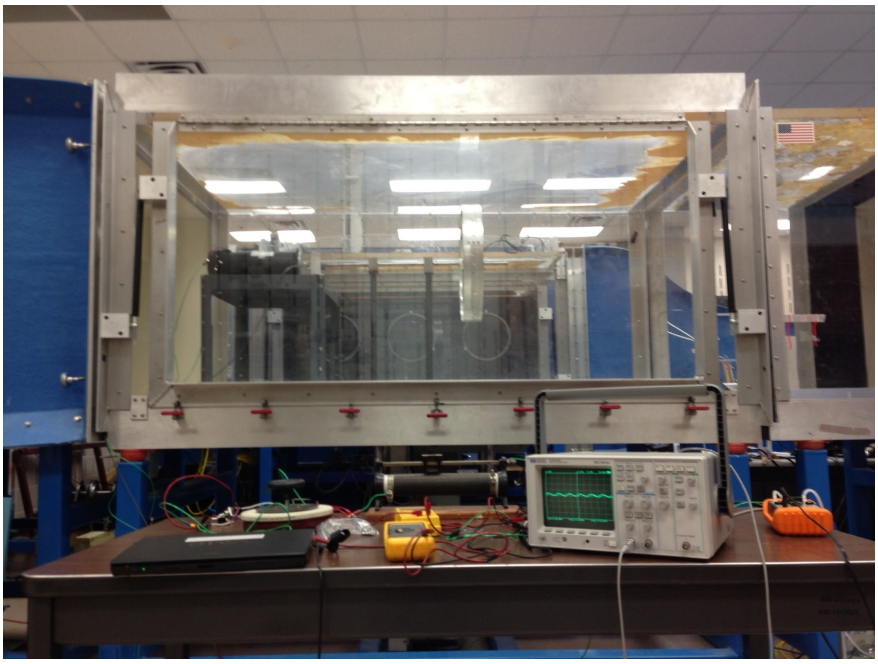

Figure 4.15: One stage of the Zephergy wind turbine ready for test in the wind tunnel.

4.8 Additional Setup Installed for Mounting the Second Stage in the Wind Tunnel

When the $C_p - \lambda$ curves were derived for each stage, additional parts were installed in the test section to run both stages simultaneously. Since the space in the test section was limited, it was impossible to install another 2-pillar structure. So the two pillars in Figure 4.6 were separated, and each one was used for one stage. The left pillar was not moved but the right one was displaced such that the distance between the two pillars was set at 19".

An electrical motor was required to be connected to the front stage. The experiments showed that at the wind speed of 18 $^{m}/_{s}$ and higher the stages could not handle the forces, and so the maximum extracted power from the first stage was about 90 W because $C_{P_{max}} \approx 0.3$. So a $^{1}/_{8} - \text{hp}$ electrical motor was enough for the

experiments. The motor was ordered from Bodine, and was a 33A Series Permanent Magnet DC Machine Model 6035.

Nominal characteristics of the motor are indicated in Table 4.2. The table shows that the motor had two different nominal modes. This motor was pretty light (6.9

Current	1.4/1.8 A
Voltage	90/130 V
Angular Velocity	1725/2500 rpm
Torque	73/95 oz-in
Power	1/8/1/4 hp

Table 4.2: Nominal specifications of the Bodine electrical motor.

lbs.), and so no table was needed to hold it in the test section. There were four 10-32 holes on its plate that were used to attach the motor to its mounting structure as indicated in Figure 4.16. The base and rod of the mounting had the same dimensions as those in the pillars. The width and radius of the head were selected based on the radius at which the holes were located on the motor plate and the length of the motor shaft. The engineering drawings of the Bodine motor and different parts of its mounting are available in APPENDIX A. The distance between the head of the mounting and the pillar was 9". The diameter of the motor shaft was 1/2"; so a 5/8" − 1/2" shaft coupling was used to connect the motor shaft to the turbine shaft.

Because there was no table for the new machine, there was no place for installing a proximity sensor close to it. If the sensor was installed beside the turbine shaft, its mounting would block the airflow, and cause a lot of disturbance. A method of determining the angular velocity was to stick a piece of steel sheet via a piece of aluminum tape to the stage, and install the proximity sensor close to the wheel

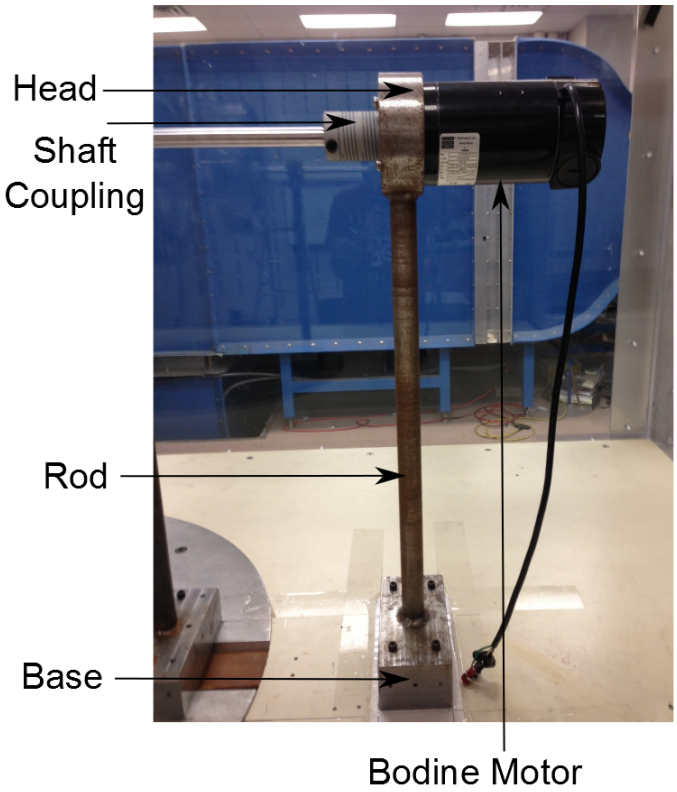

Figure 4.16: Bodine motor attached to its mounting installed in the test section.

(Figure 4.17).

Figure 4.18 indicates the additional experimental setup required for mounting the front stage in the test section.

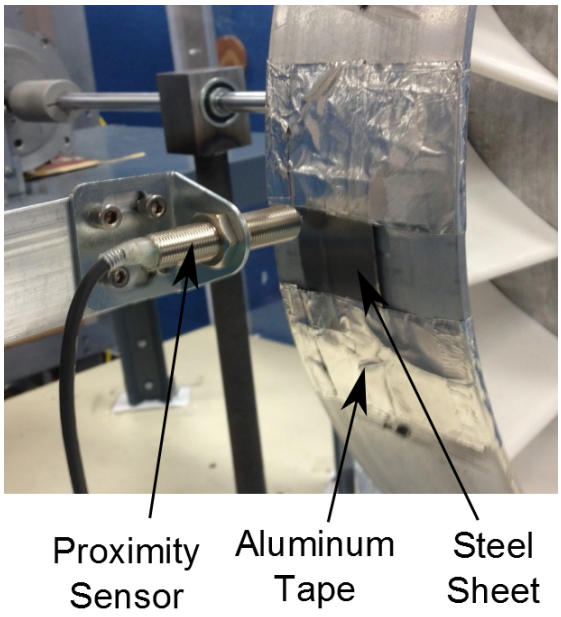

Figure 4.17: Proximity sensor beside the steel sheet attached to the stage.

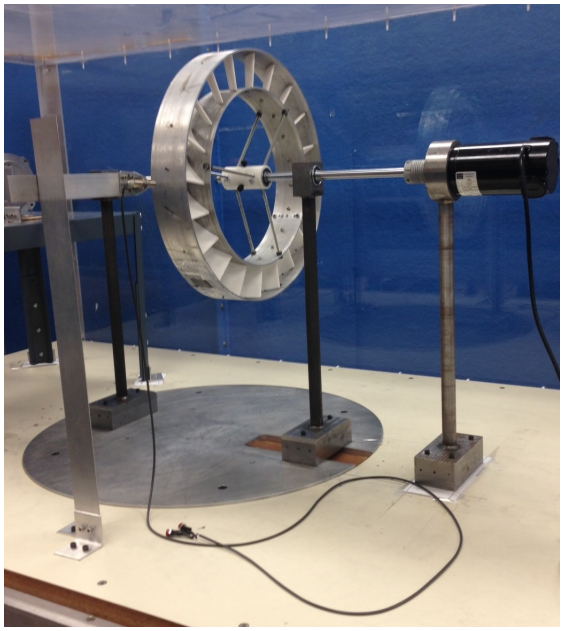

Figure 4.18: Experimental setup for mounting the front stage of the Zephergy wind turbine in the test section.

4.9 Experiments

The two stages were investigated at different experimental conditions.

4.9.1 Individual Stages with Nothing in the Front

Each stage was connected to the Dayton motor and was tested before installing the additional setup explained in Subsection 4.8. These experiments were run to derive the $C_p - \lambda$ curve for each stage.

4.9.2 Individual Stages with the Bodine Motor and its Mounting in the Front

After installing all the components explained in Subsection 4.8 other than the mounting for the proximity sensor, each stage was connected to the Dayton motor and run when the other rotor was not mounted in the front (Figure 4.19). These experiments were performed to see how the mounting affected the performance of each stage.

4.9.3 Stationary Bigger Stage in the Front

The bigger stage was mounted in front of the smaller one but it was held stationary. The distance between the two stages was set at 9" (Figure 4.20).

The bigger stage was held stationary by means of a bath sponge; the proximity sensor was removed from its mounting and the sponge was mounted instead as indicated in Figure 4.21. In this experiment the bigger stage acted like a contraction shell for the smaller one.

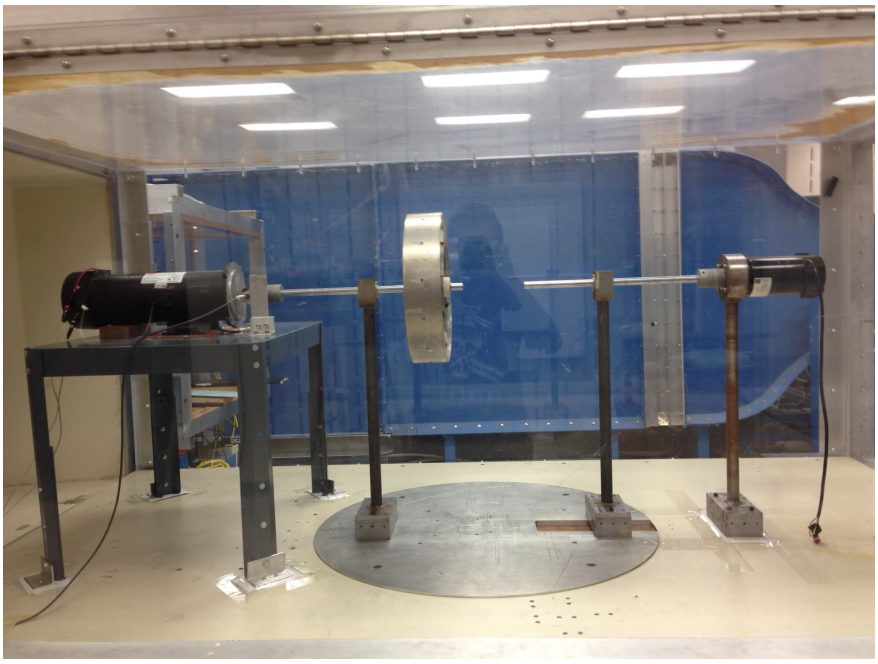

Figure 4.19: One stage running with the Bodine motor and its mounting in the front.

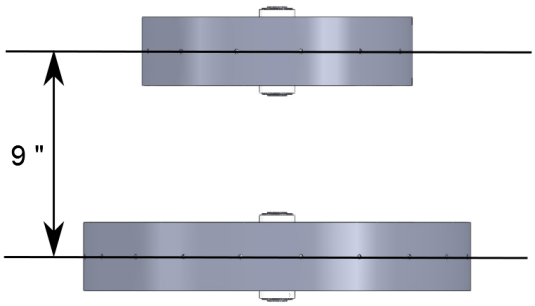

Figure 4.20: Distance between the two stages.

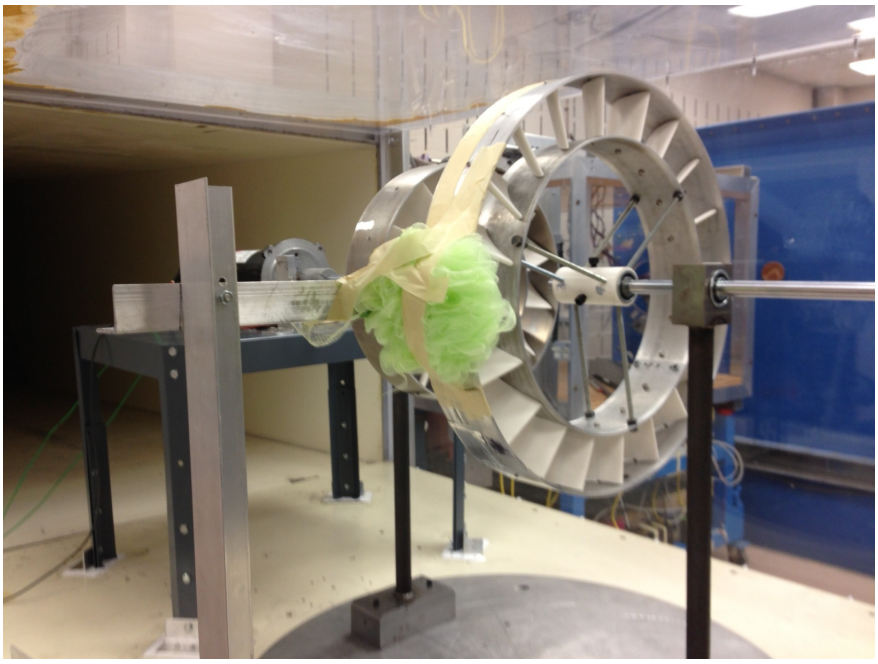

Figure 4.21: Bigger stage held stationary by means of a bath sponge.

4.9.4 Rotating Bigger Stage in the Front

In this experiment it was investigated how the rotation of the bigger stage affected the operation of the smaller stage when the bigger one was in the front. The bigger stage was coupled to the smaller motor. The resistive torque in the motor was very small compared to the Dayton one. This resulted in the bigger stage rotating very fast (for example its angular velocity at a wind speed of 10 $^{m}/_{s}$ was about 42 $^{rad}/_{s}$ when the Bodine motor was connected to a $1-\Omega$ power resistor) such that it made the structure unstable. On the other hand, it will be shown that the smaller stage showed its best performance at the wind velocities higher than 16 $^{m}/_{s}$. So the bigger stage had to be decelerated significantly in some way. Three pieces of dish sponge were attached to the end of a L-bracket, and the bracket was fixed to the mounting of the proximity sensor by means of a clamp. The proximity sensor was also installed

on the mounting by using four 3½" screws. Figure 4.22 shows the structure.

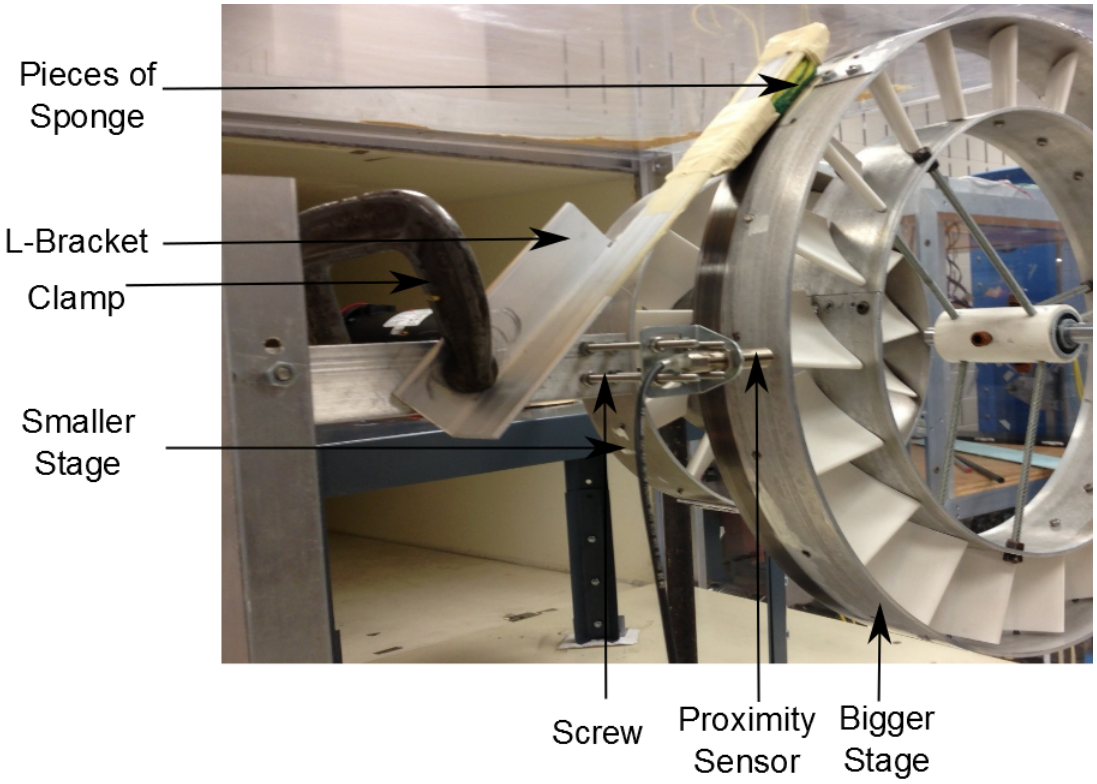

Figure 4.22: Structure used for decelerating the bigger stage.

4.9.5 Smaller Stage Coupled to the Bodine Motor, and No Stage was Connected to the Dayton One

The smaller stage was installed on the front mounting, and the other stage was not installed in the test section (Figure 4.23). This experiment was run to derive the governing equation of the losses in the Bodine motor. Section 5 will explain more about the power losses in both motors.

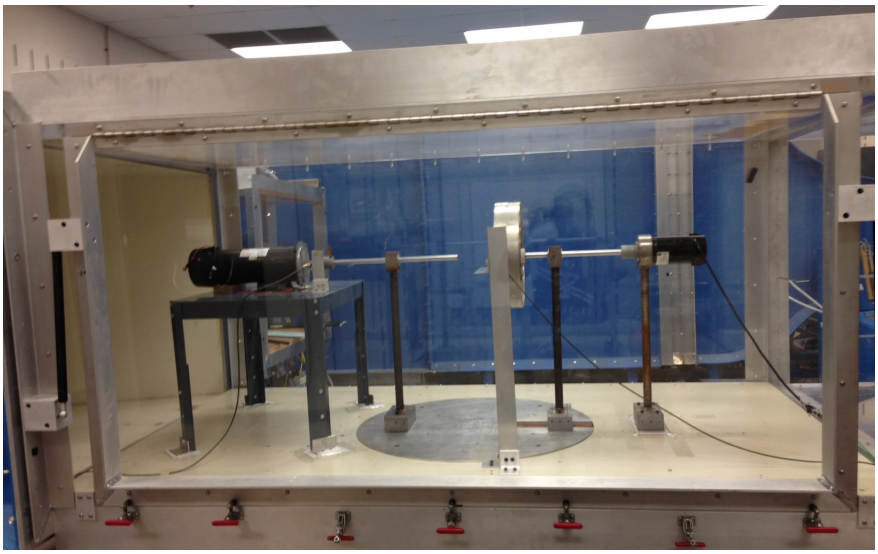

Figure 4.23: Smaller stage connected to the bodine motor with no stage in the back.

4.9.6 Smaller Stage in the Front

One of the initial goals of this project was to run both stages in such a way that the bigger one was in the front, and derive the characteristics of each stage at different angular velocities of the other one, but unfortunately the problem was that when the bigger stage was coupled to the smaller motor, it rotated very fast even at low wind speeds. Only one experiment was run with the bigger stage rotating in the front. So the two stages were installed such that the smaller stage rotated in front of the bigger one. The goal was to examine the performance of each stage at different rotational speeds of the other one. As it was explained in Subsection 4.7, the angular velocity of each rotor was proportional to the amount of the resistor connected to the electrical motor coupled to it. At first, the bigger stage was connected to $1-\Omega$, $10-\Omega$, and $100-\Omega$ power resistors, and the performance of the smaller stage was investigated when the distance between the two stages was set at $9^{"}$ (Figure 4.24). Then the experiments were run in an opposite manner, i.e., the smaller stage was connected

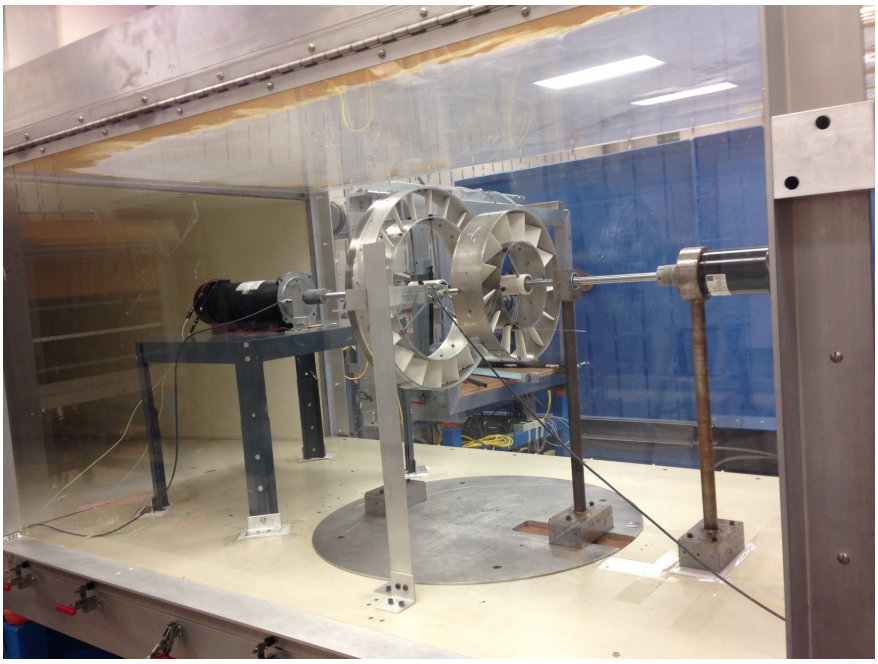

Figure 4.24: Examining the smaller stage with the bigger stage in the back.

to the three resistors, and the performance of the bigger stage was investigated. The mounting for the proximity sensor was removed from the test section because it caused a disturbance in the flow passing through the bigger stage (Figure 4.25).

Finally, the distance between the two stages was changed from 9" to 14", and two experiments were run; at each test one stage was connected to the $100 - \Omega$ resistor and the other stage was investigated. These two experiments indicated how the distance affected the operation of each stage.

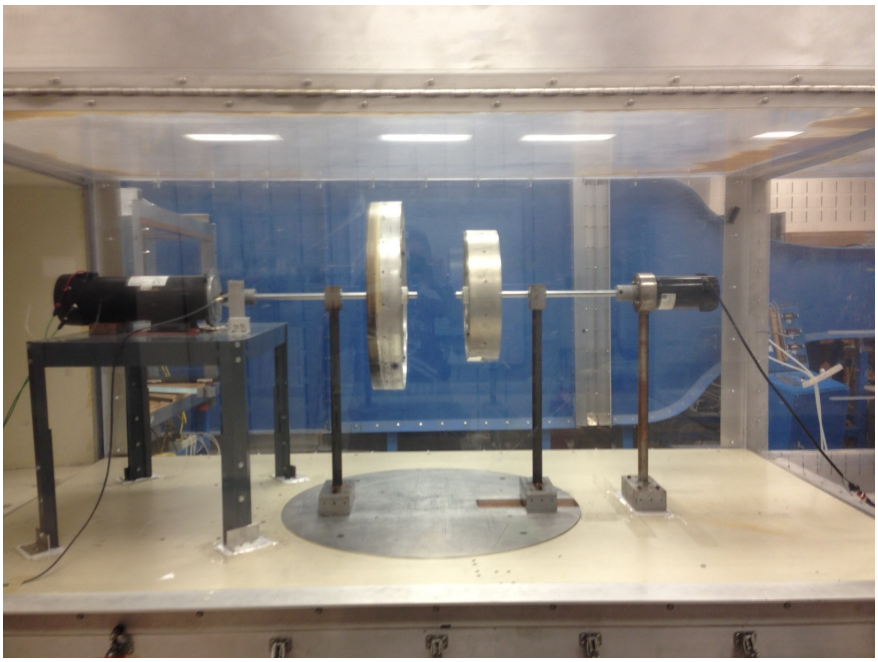

Figure 4.25: Examining the bigger stage with the smaller stage in the front.

5. CALCULATING THE OUTPUT POWER OF EACH STAGE

The power coefficient, C_P, represents the efficiency of a wind turbine. According to Equation (1.4), the generated power by each stage needed to be calculated to find the coefficient. There were two ways to determine the output power of each stage:

1. **Direct Method:** The power was equal to the generated torque multiplied by the angular velocity of the stage. So an easy way to find the power was coupling the turbine shaft to a torque-meter because it could measure the torque, angular velocity, and power. The problem was that a torque-meter was expensive; the cheapest one made by Himmelstein (the most well-known manufacturer of torque-meters in the world) in the 25 lb-in (2.82 N-m) range that was an appropriate range for the experiments in this thesis, was MCRT 48200V, and its price was $2755 based on the quote received from the company.

2. **Indirect Method:** The shaft of the turbine was connected to the shaft of the electrical motor by means of a shaft coupling in Figure 4.12. If the wasted power in the shaft coupling was negligible, all generated power by a stage was transferred to the electrical motor. Some part of this power was lost in the motor, and the remaining was conducted to the electrical circuit shown in Figure 4.14. The situation was the same for the other motor. So a method of measuring the output power of each stage was finding the input power to the electrical motors.

The indirect method was utilized to calculate the generated power by each stage. In this section, an introduction to electrical machines is provided first. Then, different types of losses in a DC machine are discussed. Measuring the input power to the first motor (the Dayton one) is described in details in the third subsection. The Bodine

motor is investigated at the end. The majority of the first subsection is from [3, 25].

5.1 Basic Concepts of Electrical Machines

Some applications such as air conditioners need electrical energy whereas some, such as fans, require a mechanical form of energy. One of the mentioned forms can be obtained from the other one by means of converters. Converters that are used to continuously translate the electrical input to the mechanical output or vice versa are called electrical machines. The process of translation is known as electromechanical energy conversion. In all machines the conversion is reversible. If the conversion is from electrical to mechanical, the machine is called a motor. The machine is said to operate as a generator when the conversion is reverse. So electrical machines work as generators when they are connected to wind turbines. In electrical machines, magnetic materials are used to produce a magnetic field that acts as a medium for energy conversion.

5.1.1 Magnetic Field

When some electrical current I passes through a conductor, a magnetic field is generated around it. Figure 5.1 shows a core and a coil of N turns extending along one leg of the core. If the core is made of iron or other ferromagnets (materials that can be magnetized by an external magnetic field and remain magnetized after the field is removed [26]), all the magnetic field produced by the current remains inside the core. Flux passing the section area in the figure is defined as

$$\Phi = \frac{\mu N I A}{l_c} \tag{5.1}$$

where μ is a characteristic of the material called permeability.

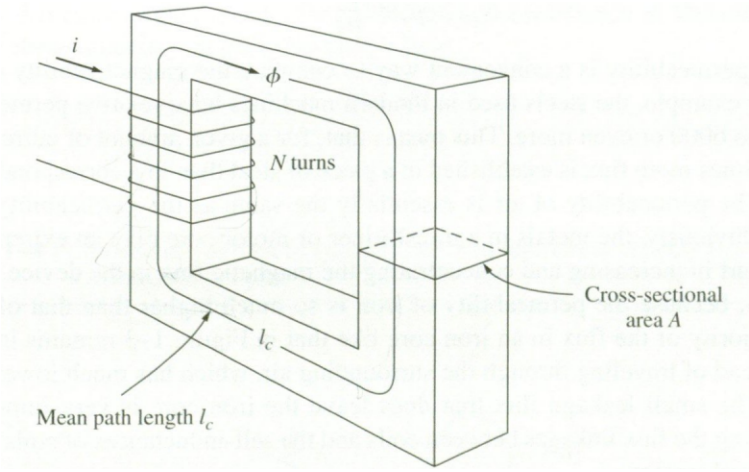

Figure 5.1: Magnetic core [3].

5.1.2 Electromagnetic Conversion

Electrical machines are used to transform energy from the mechanical form to the electrical one or vice versa. Electromechanical energy conversion is performed based on two following principal phenomena:

- If a conductor moves in a magnetic field, a voltage is induced in it.
- When a conductor carrying a current is placed in a magnetic field, a force is applied to the conductor.

Both described phenomena happen simultaneously when a machine is working in either motor or generator mode. In motoring action, an electrical system flows current through the conductors that are placed in a magnetic field. This induces a force on the conductors. If the conductors are free to rotate, the force generates a torque that will cause them to rotate at some angular velocity. The rotation of the conductors will induce a voltage on them. In the generator mode, the rotating part is driven by a mechanical system, and a voltage is induced on it. If the winding formed

by the conductors is connected to an electrical load, a current will flow. Since a current is passing through a conductor in a magnetic field, a force will be generated. The force applies a torque to the rotating part opposing the torque applied by the prime mover.

5.1.3 Structure of an Electrical Machine

An electrical machine has two major components: one part is stationary and is called stator, the other one is rotor that moves freely. There is a winding on each part. The winding in which voltage is induced is called armature winding. The main source of the flux in a machine is generated by the current passing through the field winding. In DC machines the field and armature windings are placed on the stator and rotor, respectively. In some electrical machines such as those used in this thesis, permanent magnets (objects made from ferromagnets) are used instead of the field winding as the source of the flux in the machine. This type of machine is called permanent magnet or PM. In DC machines, the induced voltage in the armature winding is alternating. A mechanical commutator and a brush assembly make the armature terminal voltage unidirectional.

5.1.4 Armature Voltage and Torque

According to the first phenomenon described in 5.1.2, when the armature rotates in the magnetic field a voltage E_a is induced in the armature winding that is known as back EMF. It can be proven that the voltage is determined by

$$E_a = K_a \Phi \omega_m \tag{5.2}$$

where K_a is the armature constant, Φ is the flux per pole (the stator of a DC machine is composed of two or more poles), and ω_m is the angular velocity of the machine

shaft.

When the armature winding carries current I_a in the magnetic field, the second phenomenon in 5.1.2 implies that a torque T_a is generated in the armature that is determined by

$$T_a = K_a \Phi I_a \tag{5.3}$$

Since both phenomena happen when an electric machine works in either the motor or generator mode, both Equations (5.2) and (5.3) always govern the machine. So in a generator action the mechanical power ($T_a \omega_m$) input to the magnetic field must be equal to the electrical power ($E_a I_a$) absorbed from it. The converse is true for the motor mode. This is confirmed by Equations (5.2) and (5.3):

$$T_a \omega_m = K_a \Phi I_a \omega_m = E_a I_a. \tag{5.4}$$

5.2 Losses in a PMDC Machine

The input power to a DC machine is not equal to its output power because some part of it is dissipated in the machine. Different types of losses in a DC machine are discussed in this subsection.

5.2.1 Copper Loss

Copper loss is the power wasted in the armature and field windings of an electrical machine. Because the machines used in this project are PMDC, it does not have any field winding and so the only copper loss existing in the machine is due to the armature winding. The copper loss in the armature (P_{copper}) is given by

$$P_{copper} = I_a^2 R_a \tag{5.5}$$

where R_a is the armature resistance.

5.2.2 Brush Loss

There is a voltage drop across the brushes in a DC motor. The drop is constant for a wide range of current passing through the armature and is about 1 V per brush that means the total voltage drop is approximately 2 V in a DC machine. As a result, the power loss in brushes (P_{brush}) is equal to

$$P_{brush} = 2I_a \tag{5.6}$$

5.2.3 Mechanical Loss

There are two types of mechanical losses in a DC machine: the first one is the friction loss caused by the bearings in the machine, and the second one is the windage loss produced by the friction between the rotating parts and the air inside the machine. The total mechanical loss is determined by the multiplication of a loss torque (T_l) and the angular velocity of the machine, i.e.,

$$P_{mech} = T_l \omega_m \tag{5.7}$$

where

$$T_l = B_l \omega_m \tag{5.8}$$

such that B_l is the damping factor.

5.2.4 Core (Iron) Loss

Losses due to an alternating current passing through a magnetic material located in a magnetic field are called core or iron losses. In a DC machine the armature current is AC although this is not true for the field current whereas in an AC machine

both currents are AC. Although the iron loss in a DC machine is less than that in a similar AC one, it could still be significant. The governing equation of the core loss is complicated and is beyond the scope of this thesis.

5.2.5 Power-Flow Diagram for a DC Machine

To understand how the input mechanical power to a DC generator is distributed at different parts of the machine, a power-flow diagram is indicated in Figure 5.2a. Since the input power to the generator (P_{gi}) is the same as the output power of the stage (P_{so}), it is equal to $T_m\omega_m$ where T_m is the torque applied to the shaft by the stage. Iron and mechanical losses are subtracted from the input power at first. The remaining mechanical power (P_{conv}), that is the multiplication of the armature torque and the angular velocity, i.e., $T_a\omega_m$, is converted to the electrical form in the armature and equals E_aI_a. Then, brush and copper losses are subtracted from the electrical power. The remaining power is the output of the generator (P_{go}), and is conducted to the electrical circuit. The power-flow diagram for a DC motor is also displayed in Figure 5.2b. In the figures, V_T is the voltage of the two output terminals.

5.3 Measuring the Power Input to the Dayton Machine

An electrical machine in a wind turbine setup works as a generator. The mechanical power applied to the machine shaft is equal to the sum of the electrical output power and the losses, i.e.,

$$P_{gi} = P_{go} + P_{loss} \tag{5.9}$$

So one way to determine the input power to the Dayton machine was to measure the output power and all losses separately. Measuring P_{go} was simple because it was

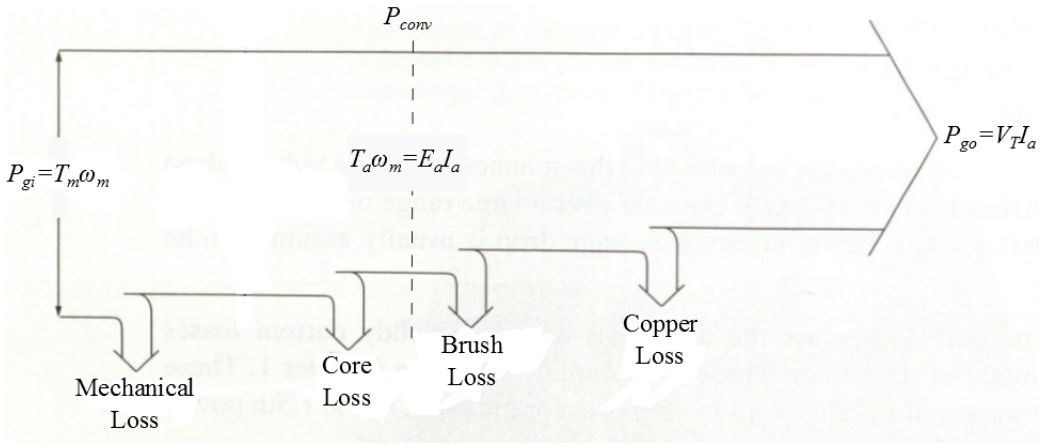

(a) Generator mode.

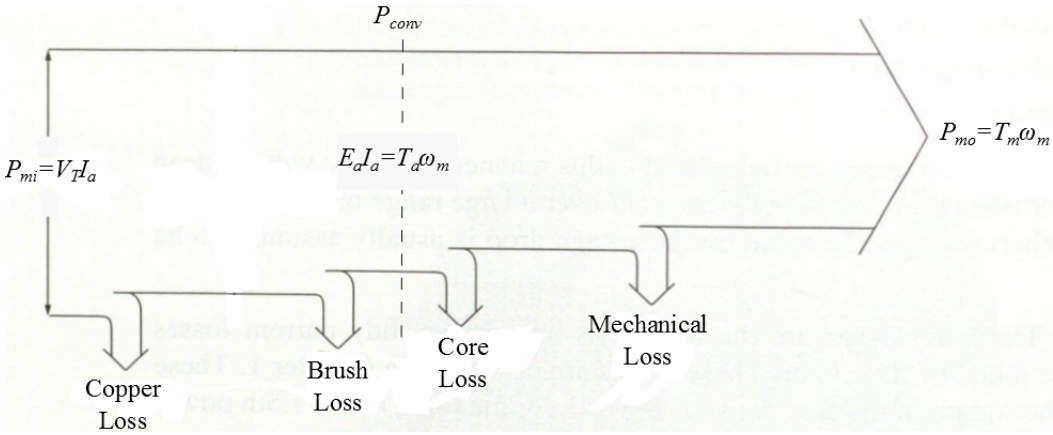

(b) Motor mode.

Figure 5.2: Power-flow diagram for a DC machine [3].

equal to

$$P_{go} = R_l I_a^2 \tag{5.10}$$

where R_l was the resistive load.

According to Equation (5.5), the armature resistance was needed to calculate the copper loss. Accessing the armature winding was difficult, and so the resistance of the whole machine was measured instead because it was almost the same as the armature resistance. An ohmmeter was connected to the output terminals of the

electrical machine to measure its resistance. Although the armature resistance was constant, the ohmmeter indicated a variable number from 3.5 Ω to 5.2 Ω when the shaft was located at different mechanical angles. The reason for such a phenomenon was the mechanism based on which the commutator-brush assembly worked in the machine to transform the alternating current to a unidirectional one.

Determining the brush loss was also complicated. Although, as it was mentioned in 5.2.2, the brush loss is usually considered equal to $2I_a$ in a wide range of the armature current, in the majority of the experiments in this thesis, the current was small (below 20% of the nominal current), and so $P_{brush} = 2I_a$ was not reliable. There was no way to estimate the brush loss in low currents. Consequently, the copper and brush losses could not be determined easily.

As it can be seen in Figure 5.2a, the mechanical power is transformed to the electrical form in the armature when a machine operates as a generator. This electrical power is distributed between the brush loss, copper loss, and finally electrical circuit. So if the power in the armature of the Dayton machine was measured, the sum of the output power of the generator and the copper and brush losses was determined. Because the machine was PM, the flux per pole, i.e., Φ was constant for all currents, and so Equation (5.3) could be written as

$$T_a = K I_a \tag{5.11}$$

where

$$K = K_a \Phi \tag{5.12}$$

Constant K in Equation (5.11) could be found by means of Figure 5.3 that was provided in the catalog of the machine. The figure shows the relation between the

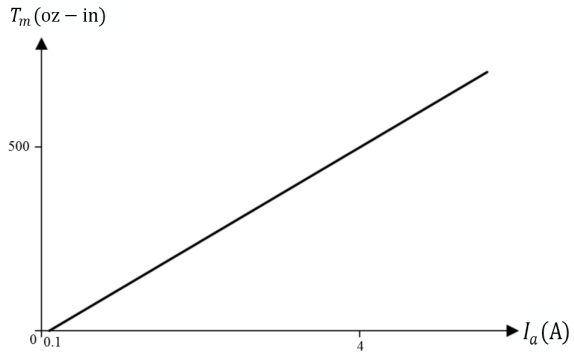

Figure 5.3: Torque-current curve of the armature in the Dayton motor.

output torque (T_m) of the machine and its input current, that is the same as the armature current because there is no field winding in a PMDC machine, when the machine operates as a motor in the nominal voltage (180 V). According to the figure,

$$T_m = k_1 I_a + k_2 \tag{5.13}$$

where

$$k_1 = \frac{500}{3.9} \text{ oz-in/A} = 0.9053 \text{ N-m/A} \tag{5.14}$$

$$k_2 = -\frac{50}{3.9} \text{ oz-in} = -0.0905 \text{ N-m} \tag{5.15}$$

Although T_m is not the same as T_a because of the mechanical and core losses, and so is not a completely linear function of I_a, the manufacturer approximates the output torque as a linear function of the armature current and so the same as the armature torque because in practical applications the difference between the approximated and real values is negligible. When the terminal voltage is different from the nominal one, only k_2 changes a little but k_1 is constant. Consequently, the coefficient K in

Equation (5.11) is the same as the coefficient k_1 in Equation (5.13), and so

$$K = 0.9053 \text{ N-m/A} \tag{5.16}$$

It should be mentioned that when the machine works as a motor and no mechanical load is connected to its shaft, a small current called no-load current (I_0) passes through the armature, and that is why the line in Figure 5.3 does not pass through the origin.

Therefore, if the output current of the generator was measured, the sum of the output power, copper loss, and brush loss was determined according to

$$P_{go} + P_{copper} + P_{brush} = KI_a\omega_m. \tag{5.17}$$

Remark: The generated power by the turbine was small (in the majority of the cases it was less than 100 W) compared to the nominal power of the machine (1 hp), and so it was not accurate to approximate the applied torque to the shaft of the generator with $T_m = KI_a$, and say

$$P_{gi} = KI_a\omega_m. \tag{5.18}$$

Two types of losses remained to be determined: the friction loss, and the iron loss. The damping factor in Equation (5.8) was required to determine the friction loss. Although some companies provide customers with the factor, it was not available in the catalog of the Dayton machine. Also, as it was mentioned earlier, finding the core loss was complicated. So there was no direct method to determine the friction and iron losses, and some method was required to estimate the sum of them.

Because the friction loss was a function of the angular velocity, and the iron loss

was a function of both angular velocity and current, the sum of the two losses had to be determined at different amounts of the current and angular velocity to find a governing equation that estimated the losses with a minimum error. To achieve this goal, the following experiment was done at the EMPE Lab at the Department of Electrical Engineering, Texas A&M University.

The machine was connected to a power supply and operated as a motor. Since the angular velocity was proportional to the back EMF and so the terminal voltage, different supply voltages made the shaft rotate at various frequencies. A hysteresis brake as a mechanical load was also connected to the motor. The brake, that was controlled by another power supply, could apply different amounts of torque to the motor shaft. Since the armature torque was a function of its current, the input current to the motor was controlled by adjusting the brake. The experimental set-up is shown in Figure 5.4.

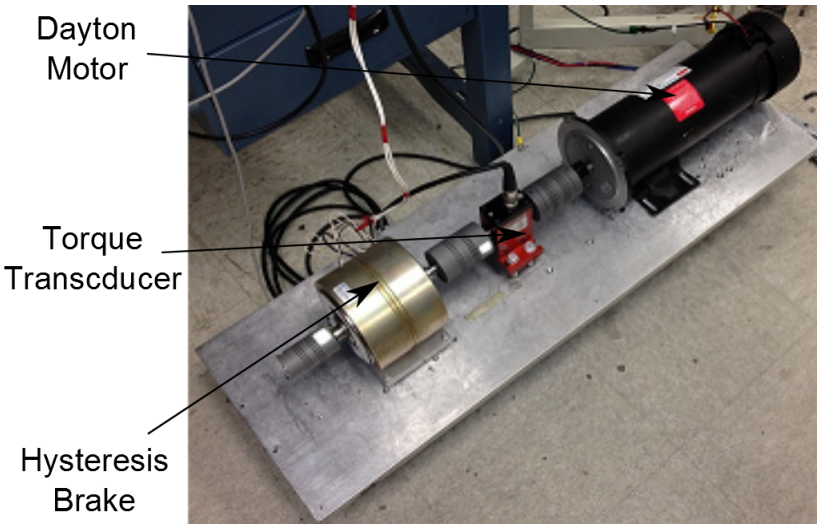

Figure 5.4: Brake-motor setup.

The torque transducer in the figure was used to measure the torque T_m applied to the shaft by the brake. For certain amounts of the armature current I_a and the angular velocity ω_m, according to the power-flow diagram in Figure 5.2b,

$$P_{conv} = T_a\omega_m = KI_a\omega_m \tag{5.19}$$

$$P_{mo} = T_m\omega_m \tag{5.20}$$

$$P_{mech} + P_{core} = P_{conv} - P_{mo} \tag{5.21}$$

where P_{mo} was the output power of the motor. The first experiment was run at the no-load condition, i.e., $T_m = 0$ but the others were done at different armature currents. Figure 5.5 shows the results of the experiments.

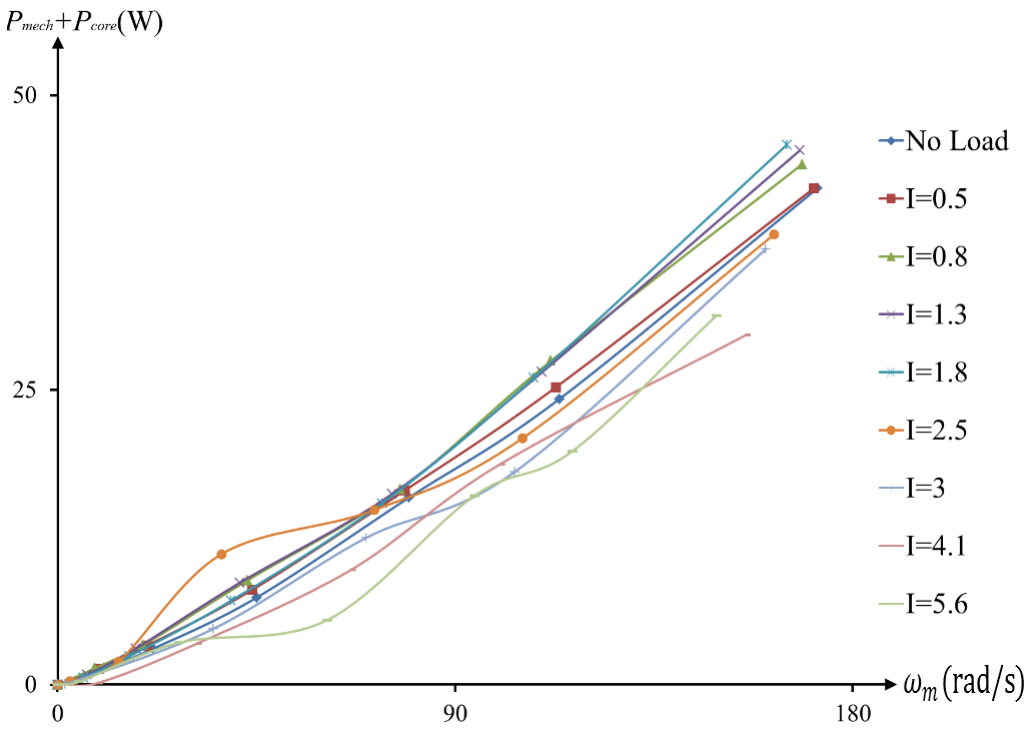

Figure 5.5: Sum of the mechanical and core losses at different currents and angular velocities for the Dayton motor.

As it was expected, the loss increased proportional to the angular velocity. In addition, for currents less than 2 A, the losses grew when the current increased, but for those amounts of the current that were greater than 2 A a lot of variation in the amount of the losses occurred that could have been because of some other phenomena that are beyond the scope of this discussion. It was observed that in the experiments in this project the current did not usually exceed 1 A let alone 2 A. In addition, high currents happened when the output power of the stage was very small; these low-power operating points were much less important than the high-power ones in the experiment results, and so the exact measurement of the power at these points was not necessary. So it was reasonable to pick the curve corresponding to $I = 0.5$ A as the curve that described the losses. Since the total amount of the mechanical and core losses was a quadratic function of the angular velocity, the curve was approximated with a polynomial of order two as

$$P_{mech} + P_{core} = 0.0004\omega_m^2 + 0.1722\omega_m \tag{5.22}$$

Since the machine and stage were coupled, their angular velocities were the same, i.e., $\omega_m = \omega$. So by measuring the rotational velocity of the turbine, ω_m was determined.

From now on, the sum of the power conducted to the output electrical circuit, and the copper and brush losses is represented by P_1, and the sum of the mechanical and core losses is indicated by P_2, i.e.,

$$P_1 = P_{go} + P_{copper} + P_{brush} \tag{5.23}$$

$$P_2 = P_{mech} + P_{core} \tag{5.24}$$

So, the output power of the stage, P_{out}, that was the same as the input power to the

generator, was equal to the sum of P_1 and P_2, i.e.,

$$P_{out} = P_1 + P_2 \tag{5.25}$$

5.4 Measuring the Input Power to the Bodine Machine

The Bodine machine was permanent magnet and DC. So the input power to the machine was calculated in a similar manner like the Dayton one. The power was comprised of two sources: P_1 and P_2 (Equation (5.25)). P_1 in (5.23) was derived from (5.17). The coefficient K in the equation was provided by the manufacturer.

$$K = 60 \text{ oz-in/A} = 0.4237 \text{ N-m/A} \tag{5.26}$$

P_2 was derived through the following procedure: the efficiency of each stage was a function of the tip speed ratio. This function for the smaller stage was derived from the experiments explained in Section 4. So at each tip speed ratio, the efficiency was known. The input power was calculated from Equation (1.5). The output power of the stage was determined by means of the efficiency and input power. By changing the resistance in the circuit, different rotational velocities and consequently various amounts of the tip speed ratio were obtained at a constant wind speed. So at different angular velocities, P_{out} and P_1 were known. The sum of the mechanical and core losses (P_2) was obtained from

$$P_2 = P_{out} - P_1 \tag{5.27}$$

P_2 is plotted versus the angular velocity (ω_m) at two different wind speeds in Figure 5.6. The two curves are a little different from each other, for example at $\omega_m = 40$ rad/s one curve gives 1.6919 W and the other one shows 2.0059 W. So the difference is only 0.314 W that is not a significant amount. The average of these two

curves is

$$P_2 = 0.00015\omega_m^2 + 0.04035\omega_m - 0.0051 \tag{5.28}$$

There are no mechanical and core losses when the shaft of an electrical machine does not rotate. So the governing equation of P_2 for the Bodine machine was considered as

$$P_2 = 0.00015\omega_m^2 + 0.04035\omega_m \tag{5.29}$$

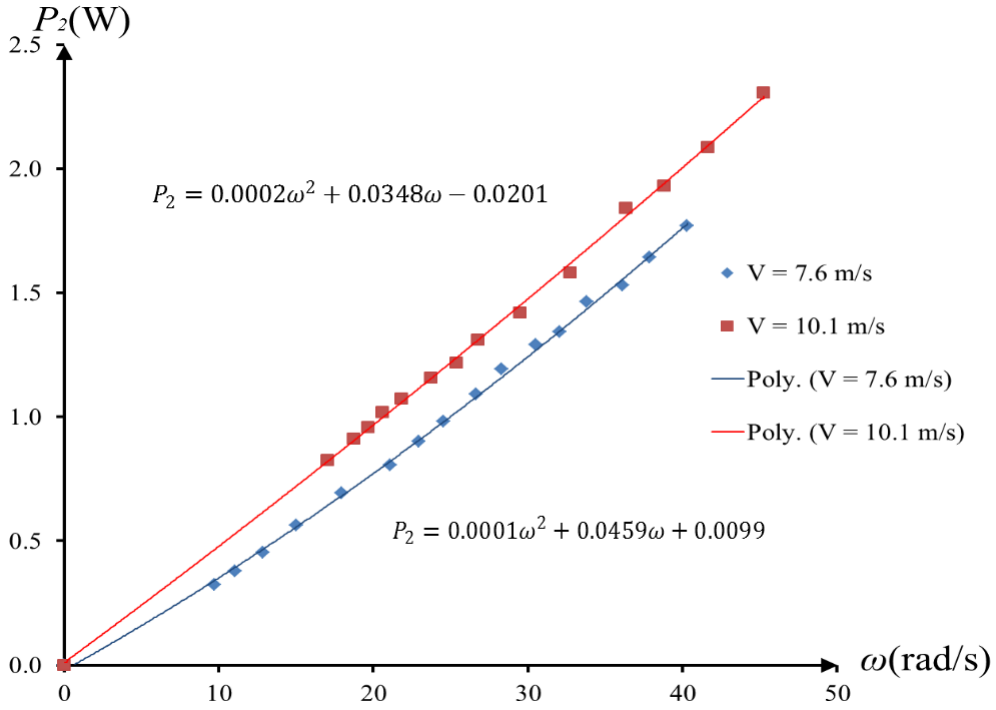

Figure 5.6: Sum of the mechanical and core losses for the Bodine motor at two different wind velocities.

6. RESULTS AND DISCUSSION

In this section, results obtained from different experiments explained in Chapter 4 are provided and investigated.

6.1 Performance of Individual Stages

The two stages indicated different performance characteristics. $C_p - \lambda$ curves were derived at two different wind velocities to establish the repeatability of the experiments.

6.1.1 The Bigger Stage

As it can be seen in Figure 6.1 the two curves of power coefficient versus tip speed ratio obtained at two different wind velocities are very close to each other that agrees with the fact that every wind turbine has a unique $C_p - \lambda$ curve.

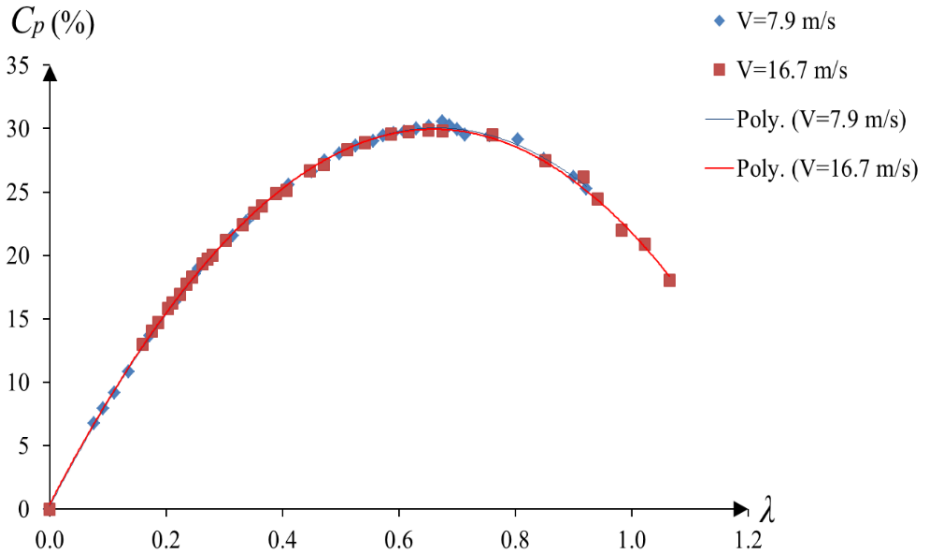

Figure 6.1: Power coefficient vs. tip speed ratio for the bigger stage.

6.1.2 The Smaller Stage

Figure 6.2 shows how the power coefficient changed when the tip speed ratio varied in the smaller stage. As it can be seen, the stage did not reach to its maximum performance at the wind velocity 13.7 $^{m}/_{s}$, and a saturation happened in the curve. One possible reason was that the stage was too small, and the resistive torque of the motor was large. So at the lower wind velocities the stage did not show its best performance.

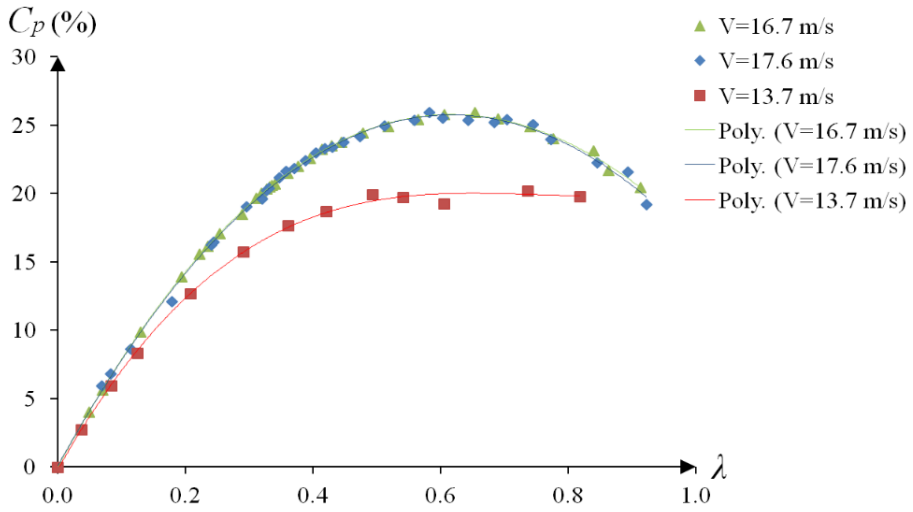

Figure 6.2: Power coefficient vs. tip speed ratio for the smaller stage.

6.1.3 Analysis of the Results

1. **Maximum Power Coefficient:** According to Betz-Joukowoski's theorem [1], the maximum possible C_p for an ideal wind turbine is equal to 0.59. Some modern large wind turbines have achieved a power coefficient up to 0.5 [12]. As it was explained in Section 1, there are many challenges that small wind turbines have to deal with such as small Reynolds number and starting performance. These

problems cause small wind turbines to have much lower power coefficients than the big size ones, for example, the maximum power coefficient of Bergey XL 10kW, that is a well-known small-size wind turbine [1], is 0.361 whereas this number for Vestas V80 2 MW is 0.435. The diameter of the first turbine is 7 m whereas the diameter of the second one is 80 m [1]. Obviously, the maximum power coefficient for the two stages of the Zephergy wind turbine with the diameter sizes of 0.4818 m (less than 7% of 7 m), and 0.3427 m (less than 5% of 7 m) are expected to be much lower than 0.361 whereas this number is 0.306 (about 85% of 0.361) and 0.259 (about 72% of 0.361) for the bigger and smaller stages, respectively. This shows that each stage had an exceptional performance.

2. **Design Tip Speed Ratio:** Wind turbines are designed in such a way that they show the maximum power coefficient at a specific tip speed ratio. For example, when it is said that a turbine has a design tip speed ratio $\lambda_D = 5$, the turbine is supposed to have the maximum C_p at $\lambda_D = 5$. Experiments that resulted in Figures. 6.1, and 6.2 showed that the tip speed ratios at which the maximum power coefficients happened for the bigger and smaller stages were 0.675 and 0.653, respectively, and so the two stages could be considered as wind turbines with low values of λ_D. Turbines with various design tip speed ratios have different characteristics and applications: a wind turbine with a higher λ_D has a larger power coefficient. According to Figure 6.3, the maximum possible power coefficient (when the lift-to-drag ratio and the number of blades are infinite) for a wind turbine with $\lambda_D = 1$ is about 0.42 whereas this coefficient for a turbine with $\lambda_D = 7$ is 0.59. In the figure, ϵ is the ratio of lift to drag, and the number of blades is indicated above each curve. The figure is provided by Schmitz [12]. He considered three major sources of loss in a wind turbine when deriving the figure:

profile loss that is drag, blade tip loss, and wake loss. The wake loss is the major source of the reduction in the power coefficient for low design tip speed ratio wind turbines [12].

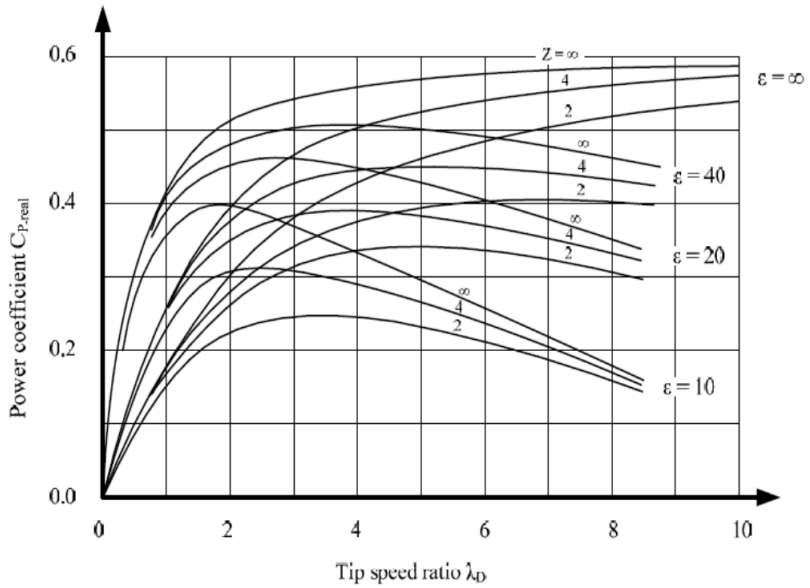

Figure 6.3: Schmitz diagram: power coefficient vs. tip speed ratio.

On the other hand, it can be verified that the starting torque in a turbine with a low λ_D is much more than the torque in a wind turbine that has a high design tip speed ratio [12]; the moment coefficient for a wind turbine is defined as

$$C_M = \frac{M}{\frac{\rho}{2}\pi R^3 V^2} \tag{6.1}$$

The moment coefficient at $\lambda = 0$, i.e., when the rotational velocity is zero, for a wind turbine with $\lambda_D = 1$ is about 0.325 whereas the coefficient for another turbine with $\lambda_D = 7$ is around 0.01 [12]. As it was explained earlier, the starting

torque is one of the main problems that small-size wind turbines have to deal with. Finally, the applications are totally different. Turbines with high design tip speed ratios are used for electricity generation whereas those with low values of λ_D are used in machines such as piston, heat pumps, or sawmills where high torques are required.

Therefore, each stage of the Zephergy wind turbine had a significant starting torque on one hand and so did not have the problem of starting performance, but had an excellent power coefficient on the other hand. As a result, unlike the conventional wind turbines with low design tip speed ratios, Zephergy can be used for the electricity generation.

6.1.4 Generated power by the two stages when $V = 17\,\mathrm{m/s}$

The generated power by a wind turbine is more important for the owner than the power coefficient. Figure 6.4 indicates how much power each stage of the Zephergy wind turbine produces at different angular velocities when the wind velocity is $17\,\mathrm{m/s}$.

6.2 Performance of the Stages When the Bodine Motor and its Mounting Were in the Front

The Bodine motor and its mounting acted like a block for the stage coupled to the other motor, and caused some disturbance in the airflow. The results indicate how the operation of each stage was affected.

6.2.1 The Bigger Stage

Figure 6.5 shows the $C_p - \lambda$ curve for the bigger stage when the Bodine motor and its mounting were in front of it. Figure 6.6 compares the performance of the stage when there existed and there did not exist the block in the front. As it can be

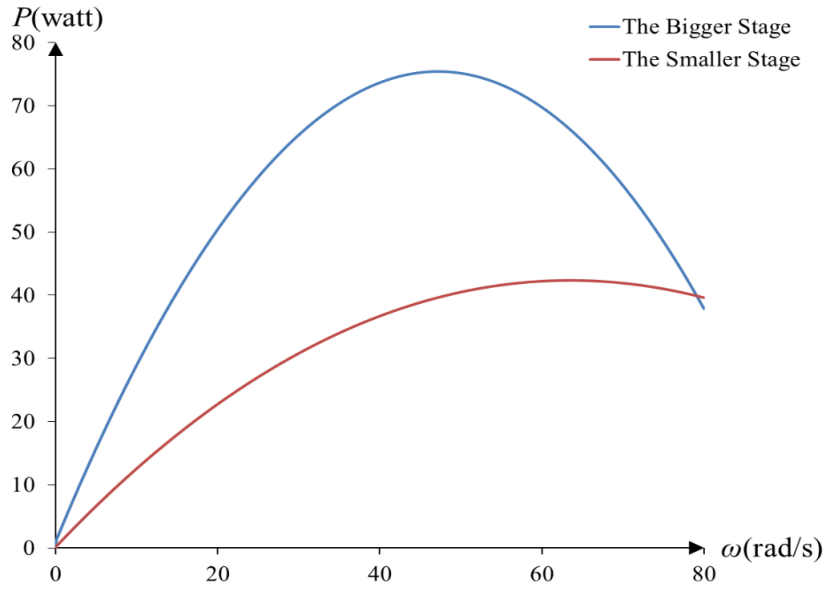

Figure 6.4: Generated power by the two stages at $V = 17$ m/s.

seen in the figure, the block reduced the efficiency.

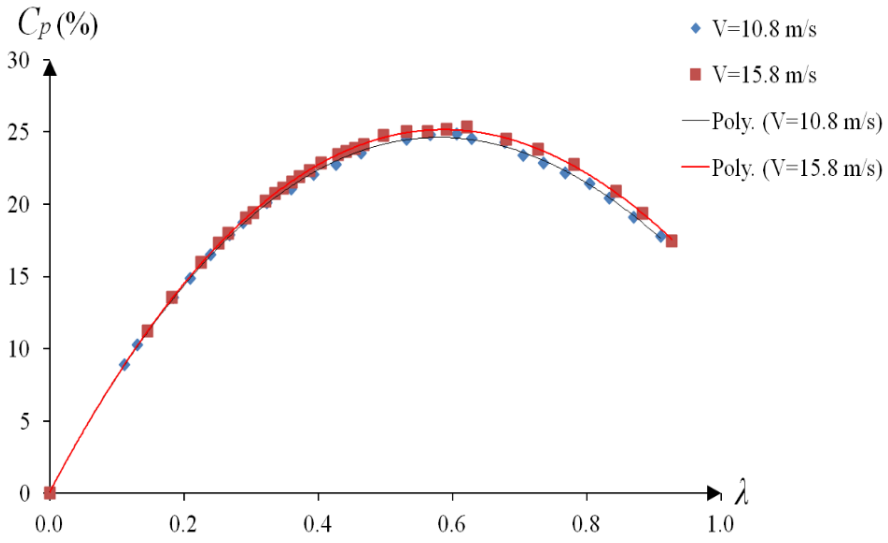

Figure 6.5: Performance of the bigger stage with the block in the front.

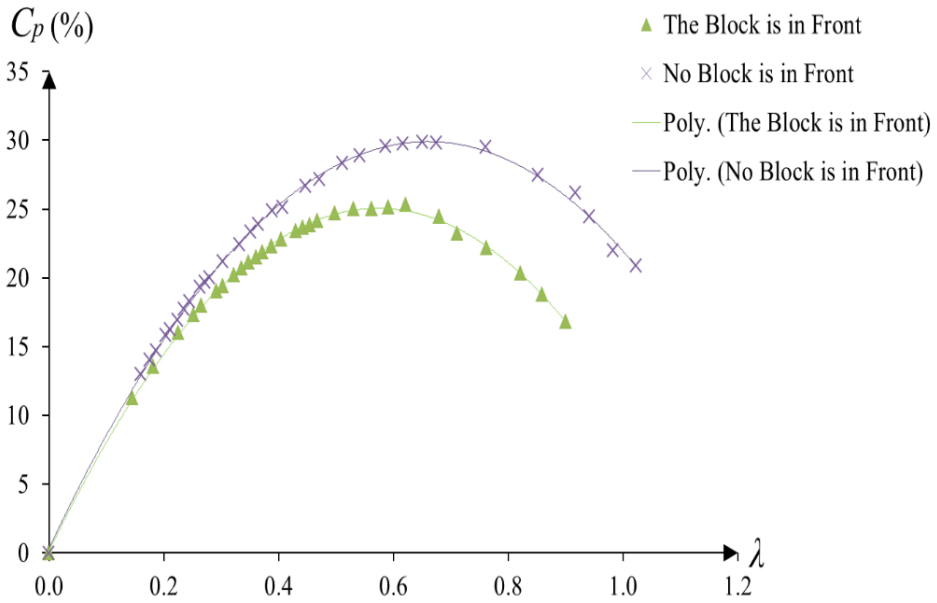

Figure 6.6: Performance of the bigger stage in two different situations: with and without the block in the front.

6.2.2 The Smaller Stage

The power coefficient versus tip speed ratio for the smaller stage when the Bodine motor was in the front is indicated in Figure 6.7. Like the bigger stage, the block in front of the stage reduced its performance as it is shown in Figure 6.8.

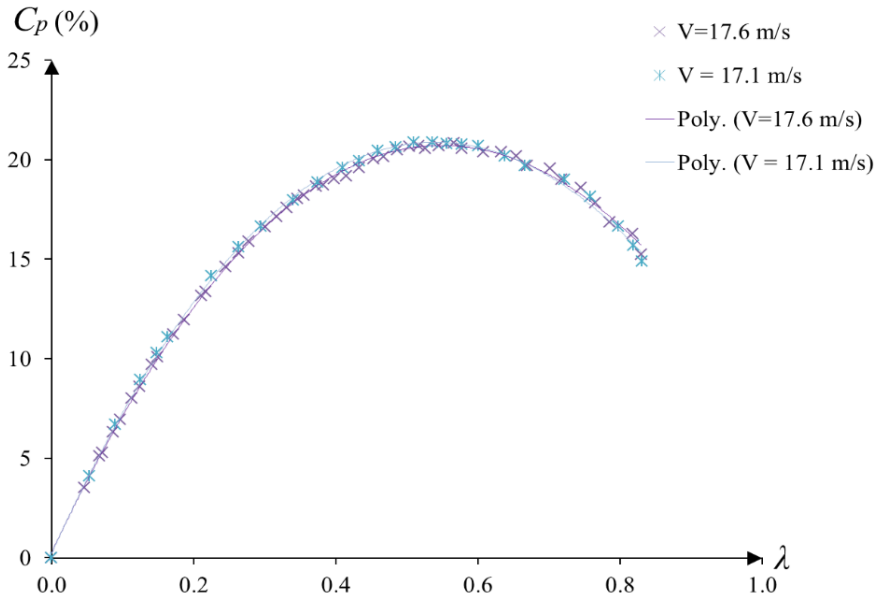

Figure 6.7: Performance of the smaller stage with the block in the front.

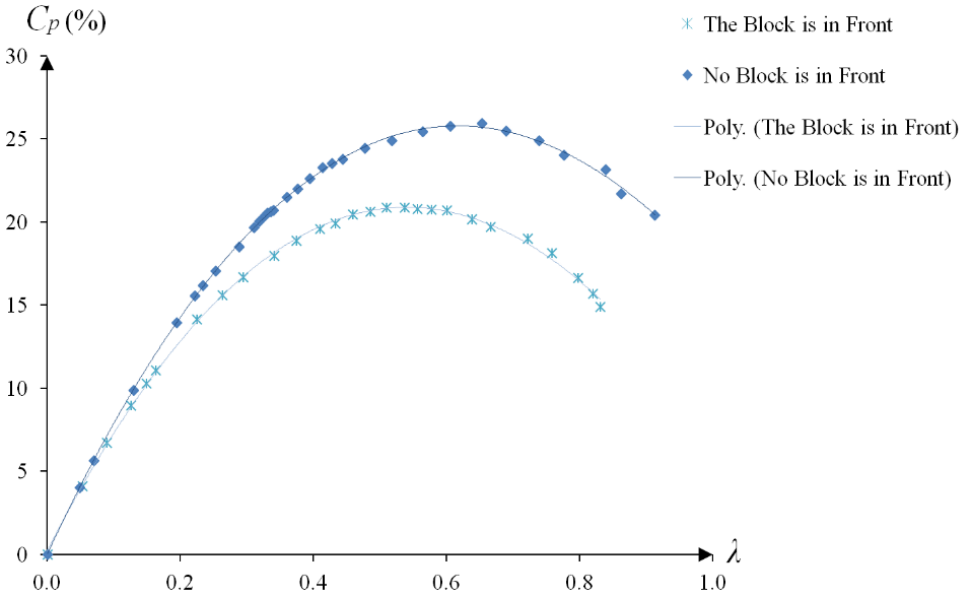

Figure 6.8: Performance of the smaller stage in two different situations: with and without the block in the front.

6.3 Characteristic Curve of the Smaller Stage When the Stationary Bigger Stage Was in the Front

The performance of the smaller stage was investigated when the bigger stage was held still in front of it (Figure 6.9).

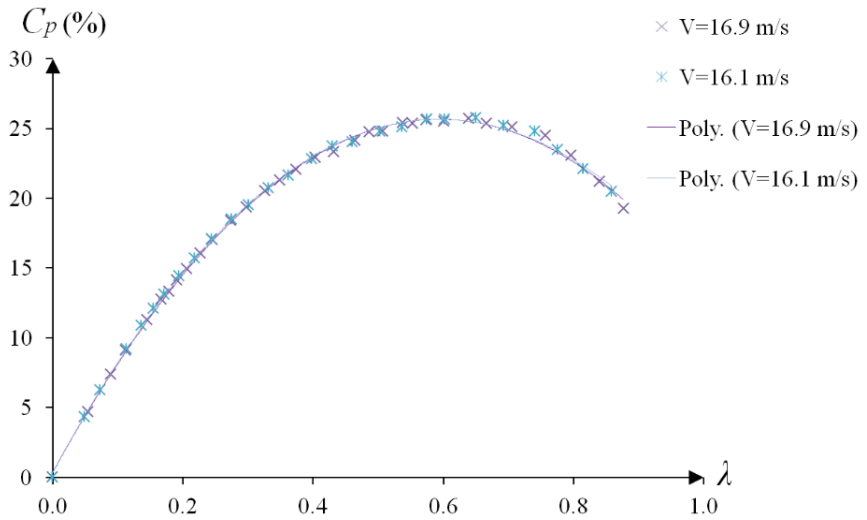

Figure 6.9: Performance of the smaller stage when the bigger stage was held stationary in the front.

The stationary stage acted like a contraction shell for the smaller stage and helped improve its performance compared to the case when the only object in the front was the Bodine motor and its mounting as indicated in Figure 6.10. The figure also shows that the characteristic curve was similar to the curve when nothing was in front of the stage.

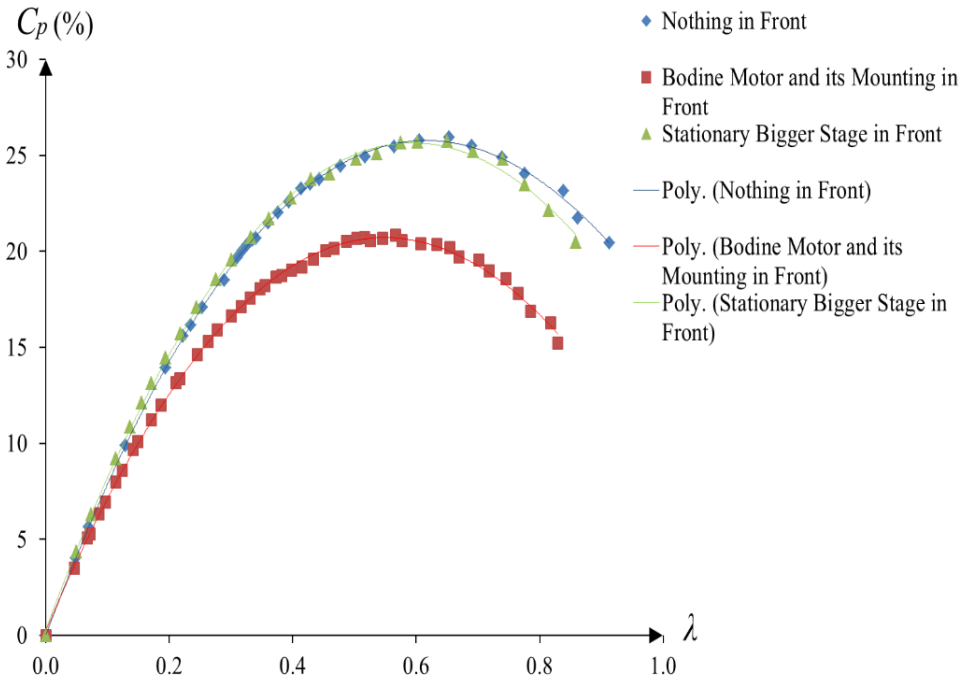

Figure 6.10: Performance of the smaller stage in three different situations: with and without the block in the front, and with the stationary bigger stage in the front.

6.4 Performance of the Smaller Stage When the Bigger Stage Was Rotating in the Front

As it was explained in 4.9.4, making the bigger stage operate at high wind speeds when it was coupled to the smaller motor was impossible because the rotational speed was very high, and a brake-like structure was required to decelerate the stage. Even by using the brake, the total structure of the turbine shook a lot and was barely stable. So the experiment was run only at one wind speed that was 16.2 $^{m}/_{s}$. The bigger stage was connected to a $1-\Omega$ power resistor to minimize its velocity. Its angular velocity was 36.1103 $^{rad}/_{s}$. The distance between the two stages was 9". The previous experiments were repeatable, and so the result was reliable. Figure 6.11 indicates the performance of the smaller stage, and compares it with two other

cases: when the bigger stage was stationary, and when the block was the only object in the front. Although the rotation of the bigger stage caused some fluctuation in the airflow and reduced the efficiency of the smaller one compared to the case when it was stationary, the performance was still better than the case when it was not in front of the smaller stage.

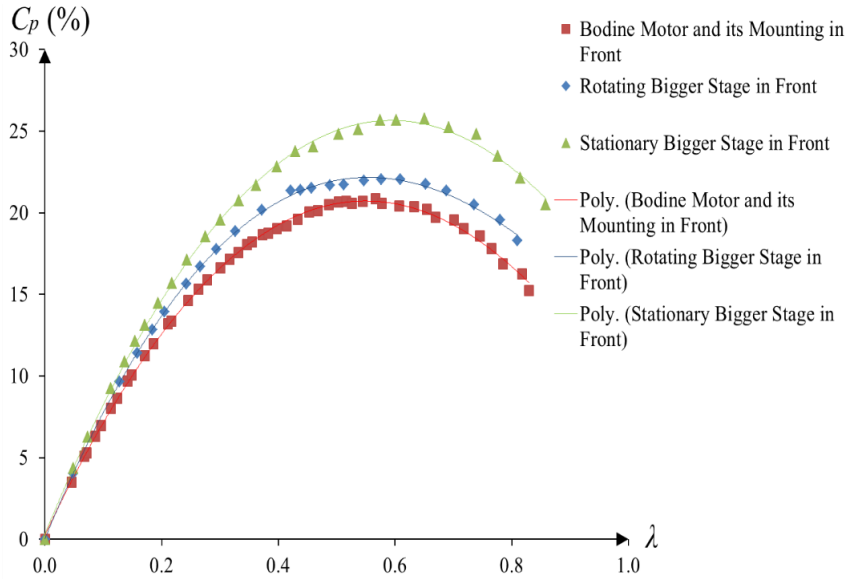

Figure 6.11: Performance of the smaller stage in three different situations: with the block, the stationary stage, and the rotating bigger stage in the front.

6.5 Characteristic Curves of the Two Stages When the Smaller Stage Was Rotating in the Front

It was not possible to run more than one experiment when the bigger stage was rotating in front of the smaller one. So the turbine was run in such a way that the smaller stage rotated in the front. Each stage was investigated when the other one was connected to three different power resistors.

6.5.1 The Smaller Stage

Figure 6.12 shows the $C_p - \lambda$ curves of the smaller stage when the resistance in the output electrical circuit of the bigger stage was 1 Ω, 10 Ω, and 100 Ω . The maximum power coefficients at the two cases $R = 1\,\Omega$ and $R = 10\,\Omega$ were the same. The only difference was that at the lower tip speed ratios the efficiency was more when $R = 1\,\Omega$ and so the bigger stage rotated slower, but at the higher ratios the efficiency was more when the other stage turned faster, i.e., when $R = 10\,\Omega$. The result was different when the resistance was 100 Ω. In this case the bigger stage rotated very fast and caused some disturbance in the airflow, and so reduced the efficiency.

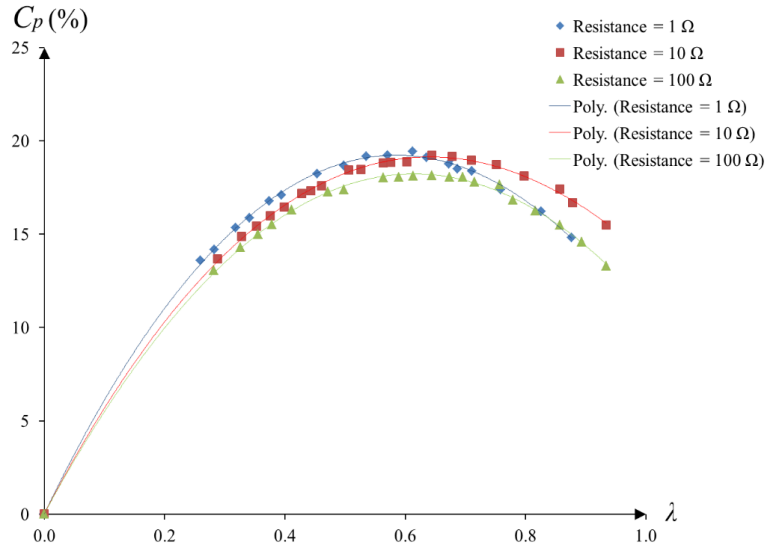

Figure 6.12: $C_p - \lambda$ curves of the smaller stage when the bigger stage was rotating behind.

It is interesting to compare the operation of the smaller stage in three cases: the Bodine motor and its mounting were in front of the stage in the first case. In

the second and third situations, the bigger stage was connected to a $100-\Omega$ power resistor and rotated in front of and behind the smaller one, respectively. Figure 6.13 indicates the comparison. The figure shows that when the bigger stage rotated in the front it influenced the smaller one in a positive manner whereas it reduced the efficiency of that stage when it rotated behind.

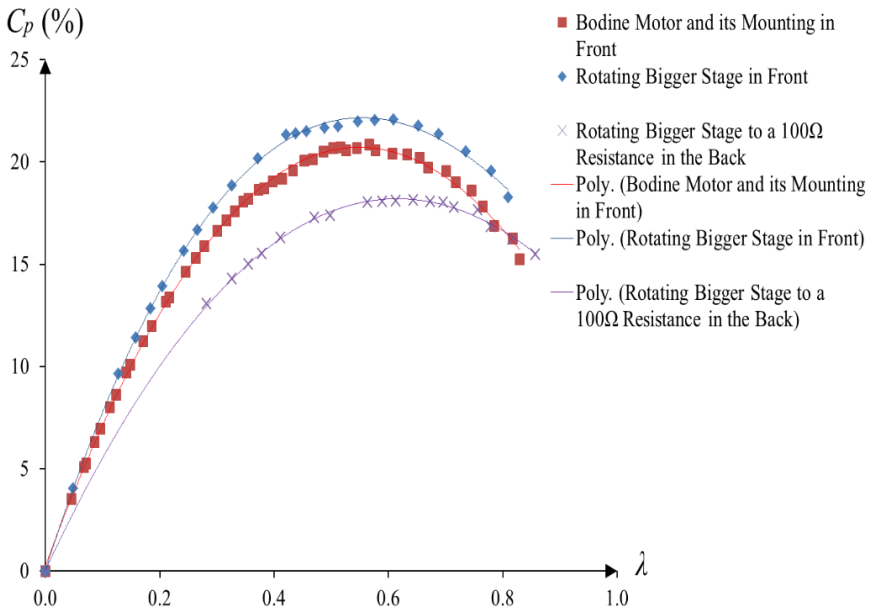

Figure 6.13: Performance of the smaller Stage in three different situations: with the block in the front, the rotating bigger stage in the front, and the rotating bigger stage connecting to a $100-\Omega$ power resistor in the back.

6.5.2 The Bigger Stage

The performance of the bigger stage when the smaller one rotated in front of it and was connected to the three different resistors is indicated in Figure 6.14. Figure 6.15 compares the operation of the stage in two different cases: when the Bodine motor and its mounting were in the front, and when the other stage was installed on

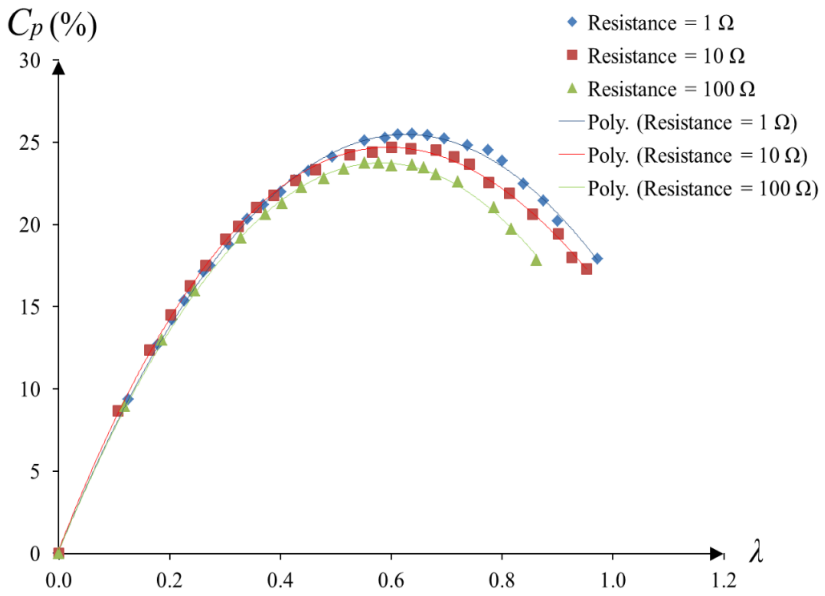

Figure 6.14: $C_p - \lambda$ curves of the bigger stage when the smaller stage was rotating in the front.

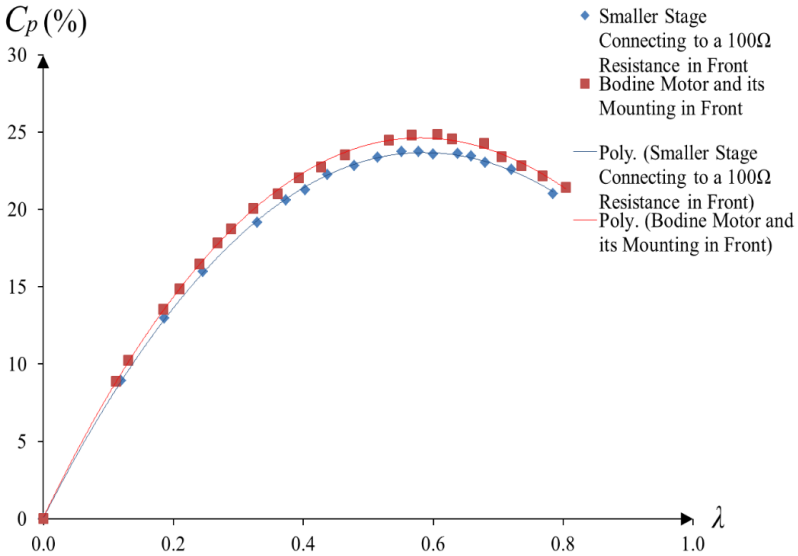

Figure 6.15: Performance of the bigger stage in two different situations: with the block in the front, and the rotating smaller stage connecting to a $100 - \Omega$ power resistor in the front.

the mounting and connected the $100-\Omega$ power resistance. The figure shows that the rotation of the smaller stage in front of the bigger one reduced the efficiency of that stage.

6.6 Impact of the Distance Between the Two Stages on Their Performance

The distance between the two stages was changed from 9" to 14". Two experiments were run; at each test, one stage was connected to a $100-\Omega$ power resistor, and the other stage was investigated. A $100-\Omega$ resistor was chosen because it caused the connected stage to rotate very fast that resulted in a lot of disturbance.

6.6.1 The Smaller Sage

Figure 6.16 shows the performance of the smaller stage, and compares it with the similar experiment when the distance was set at 9". As it is indicated, increasing the distance reduced the effect of the generated disturbance by the other stage that resulted in an increase in the efficiency.

6.6.2 The Bigger Stage

The impact of the distance between the two stages on the performance of the bigger stage is indicated in Figure 6.17. Like the smaller stage, raising the distance improved the performance.

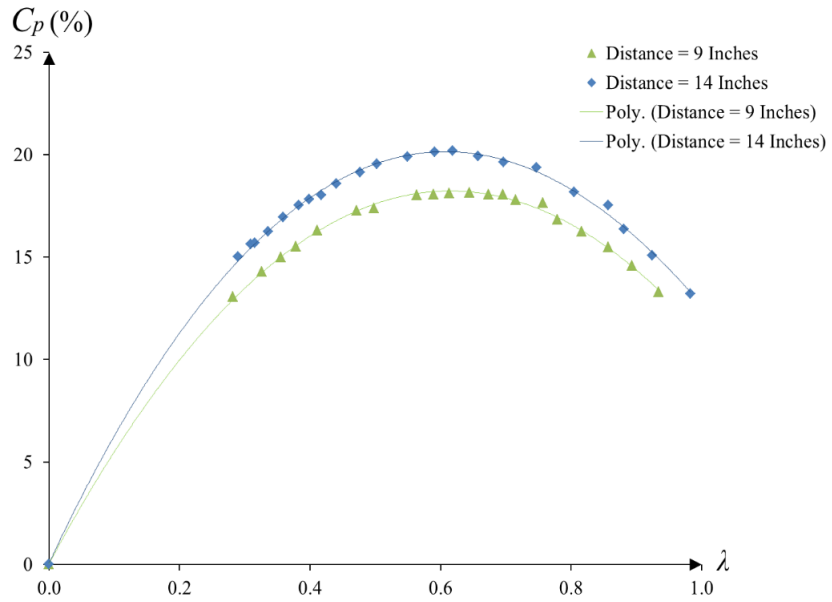

Figure 6.16: Effect of the distance between the two stages on the operation of the smaller stage.

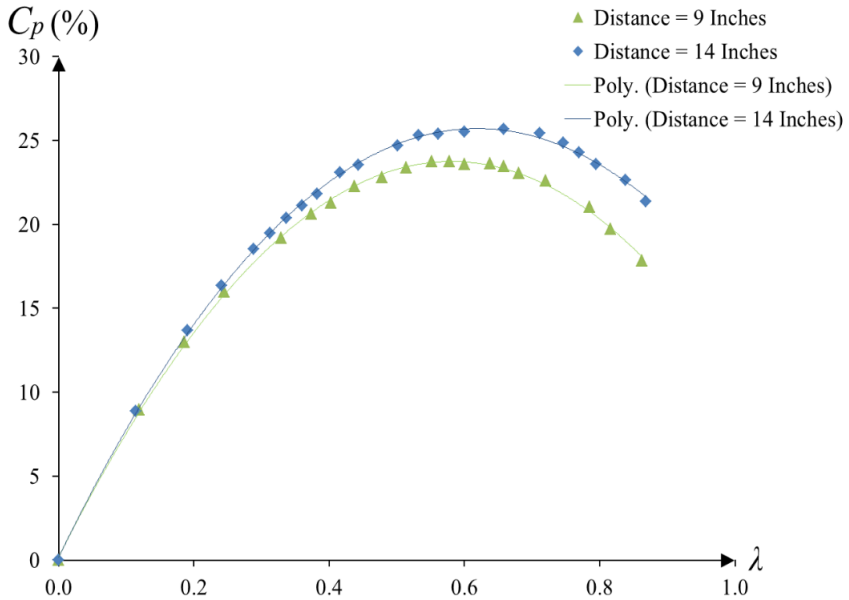

Figure 6.17: Effect of the distance between the two stages on the operation of the bigger stage.

7. SUMMARY, CONCLUSION, AND RECOMMENDATIONS FOR FUTURE WORK

7.1 Summary

There are many problems associated with small wind turbines that the large-size ones do not deal with. Small Reynolds number and starting performance are two of these challenges. These problems make them more expensive than the large ones per unit power. Therefore, new technologies are in demand to improve the quality of these turbines and reduce their costs. This thesis was devoted to investigating a novel type of small wind turbine called Zephergy. Unlike the conventional wind turbines, Zephergy was composed of more than one rotor. Each rotor was named a stage or wheel. A two-stage turbine was examined. Each stage had two inner and outer rings between which the blades were mounted. The diameters of the outer and inner rings for the bigger stage were 18.9690" and 13.4940", and for the smaller one were 13.2426" and 7.6976", respectively. So there was no overlap between the blades of the two stages. Designing the blades and choosing the number of them were performed based on turbomachinery. At first, pieces of magnets were supposed to be installed on a third ring such that each stage rotated the magnets around the coils, but the magnets and coils were not provided by the third party.

Different parts of the experimental setup for mounting one stage in the test section were investigated. To extract energy from the wind, the stage had to be connected to an electrical motor which in turn supplied a resistive load. It was explained that the most important curve that describes the efficiency of a wind turbine is the power coefficient versus tip speed ratio. A rheostat (variable resistor) was utilized as the load. By changing the amount of the load resistance, different angular velocities,

and so tip speed ratios were derived at a constant wind speed. To derive the power coefficient it was required to determine the output power of the stage. This goal was achieved by calculating the input power to the electrical motor coupled to the stage. An additional setup including another electrical motor was installed in the test section to make it possible to mount both stages in the test section.

Different experiments were run when both stages were in the test section to see how the presence of one stage affected the operation of the other. The distance between the two stages was set at 9". One goal of the experiments was to investigate the effect of a contraction shell for the turbine. So the bigger stage was held stationary in front of the smaller one in a test. In this situation, the bigger stage performed like a contraction shell for the smaller one. The primary goal of the experiments was to run the bigger stage in the front, but this required the stage to be coupled to the front motor. Because this motor was a small power one (1/8 hp) its resistive torque against the stage was not large enough, and so the stage rotated very fast even at low wind speeds such that the mounting structure became unstable. So only one experiment was run with the bigger stage rotating in the front. Then, the two stages were exchanged with each other, i.e., the bigger one was installed in the back. In this situation six experiments were run to see how the rotation of one stage at different angular velocities affected the operation of the other. Finally, the distance between the two stages was changed to 14" to investigate the effect of the distance on the performance of the stages.

7.2 Conclusion

Each stage indicated a very good performance: the maximum efficiencies for the bigger and smaller stages were 0.306 and 0.259, respectively. That coefficient for Bergey XL 10 kW that is a typical small-size wind turbine with a diameter of 275.591"

is 0.361. This means that whereas the diameters of the first and second stages were less than 7% and 5% of the diameter of the Bergey turbine, their maximum power coefficients were more than 84% and 71% of the corresponding coefficient for the Bergey one. Furthermore, $C_{P_{max}}$ happened at tip speed ratios that were less than 0.7. It can be verified that the starting torque for a wind turbine with a low design tip speed ratio is much more than the torque generated by a turbine designed to operate at a high tip speed ratio. So, the stages did not have the problem of starting performance common in small-size wind turbines.

Different experiments were run when both stages were mounted in the tunnel. It was shown that the performance of the smaller stage was improved when the other stage was held still in the front, and so a contraction shell could improve the operation of the stages.

Rotation of one stage affected the operation of the other. When the bigger stage rotated in front of the smaller one, interestingly not only it did not reduce the efficiency of that stage, but rather improved it. The reason was that the presence of the bigger stage in the front conditioned the airflow passing through the smaller one, although the rotation of the bigger wheel caused some disturbance. When the smaller stage was mounted in the front, rotation of each stage reduced the efficiency of the other. The faster one stage rotated, the higher the decrease in the efficiency of the other became. The reason was that the rotation of each wheel disturbed the airflow which in turn decreased the efficiency of the other. This disturbing effect was reduced when the distance between the two stages was increased.

7.3 Recommendations for Future Work

The blades were designed based on the experience of the designer, and no CFD (computational fluid dynamics) was done to simulate their performance. Because

the aerodynamic operation of each stage was dependent on the blade shape, more analysis on the blades either by CFD or BEMT (blade element momentum theory) [12] is necessary, and will improve the efficiency.

If the electrical motors are replaced by magnets and coils, performance of the stages will improve because there will be no more resistive torques. Another issue that could increase the efficiency is using a contraction shell for the whole turbine.

REFERENCES

[1] D. Wood, *Small Wind Turbines: Analysis, Design, and Application*, ser. Green energy and technology. Springer London, 2011.

[2] A. Glassman, *Turbine design and application*, ser. NASA SP. Scientific and Technical Information Office, National Aeronautics and and Space Administration: [For sale by the Supt. of Docs., U.S. Govt. Print. Off.], 1972, no. v. 1.

[3] S. Chapman, *Electric machinery and power system fundamentals*, ser. McGraw-Hill series in electrical and computer engineering. McGraw-Hill, 2002.

[4] P. Clausen and D. Wood, "Recent advances in small wind turbine technology," *Wind Engineering*, vol. 24, no. 3, pp. 189–201, 2000.

[5] "Annual Energy Outlook 2013," U.S. Energy Information Administration, Tech. Rep., April 2013.

[6] "20 percent Wind Energy by 2030," U.S. Department of Energy, Tech. Rep., July 2008.

[7] Database of State Incentives for Renewables and efficiency. [Online]. Available: http://www.dsireusa.org/rpsdata/index.cfm

[8] "AWEA U.S. Wind Industry Annual Market Report," American Wind Energy Association, Tech. Rep., 2013.

[9] "2011 U.S. Small Wind Turbine Market Report," American Wind Energy Association, Tech. Rep., 2012.

[10] T. Maeda, Y. Kamada, J. Suzuki, and H. Fujioka, "Rotor blade sectional performance under yawed inflow conditions," *Journal of Solar Energy Engineering*, vol. 130, p. 031018, 2008.

[11] T. Pedersen, "On wind turbine power performance measurements at inclined airflow," *Wind Energy*, vol. 7, no. 3, pp. 163–176, 2004.

[12] R. Gasch and J. Twele, *Wind Power Plants: Fundamentals, Design, Construction and Operation*, ser. Electrical Engineering. Springer Berlin Heidelberg, 2011.

[13] W. Shyy, *Aerodynamics of Low Reynolds Number Flyers*, ser. Cambridge Aerospace Series. Cambridge University Press, 2008.

[14] M. Anderson, D. Milborrow, N. Ross, and G. Britain, *Performance and wake measurements on a 3 m diameter horizontal axis wind turbine: comparison of theory, wind tunnel and field test data*. Department of Energy Energy Technology Support Unit, 1982.

[15] R. E. Sheldahl and P. C. Klimas, "Aerodynamic characteristics of seven symmetrical airfoil sections through 180-degree angle of attack for use in aerodynamic analysis of vertical axis wind turbines," Sandia National Labs., Albuquerque, NM (USA), Tech. Rep., 1981.

[16] C. Ostowari and D. Naik, "Post stall studies of untwisted varying aspect ratio blades with an naca 4415 airfoil section-part i," *Wind Engineering*, vol. 8, no. 3, pp. 176–194, 1984.

[17] T. M. Jahns and W. L. Soong, "Pulsating torque minimization techniques for permanent magnet ac motor drives-a review," *Industrial Electronics, IEEE Transactions on*, vol. 43, no. 2, pp. 321–330, 1996.

[18] M. Selig, "New airfoils for small horizontal axis wind turbines," *Urbana*, vol. 51, pp. 61 801–2935, 1998.

[19] P. Giguere and M. S. Selig, "Low reynolds number airfoils for small horizontal axis wind turbines," *Wind Engineering*, vol. 21, no. 6, pp. 367–380, 1997.

[20] T. Kogaki, H. Matsumiya, M. Iida, T. Inaba, N. Yoshimizu, and K. Kieda, "Development and experimental verification of an airfoil for small wind turbines," in *Proceedings of 2002 global windpower conference and exhibition*, 2002.

[21] D. Schum, "Wind turbine having multiple power generating elements," Patent 13/157,701, 07 08, 2013.

[22] Bezier Curve - Wikipedia: http://en.wikipedia.org/wiki/BezierCurve.

[23] I. Abbott, *Theory of Wing Sections*. Gannon Distributing Company, 1959.

[24] Proximity Sensor - Wikipedia: http://en.wikipedia.org/wiki/ProximitySensor.

[25] P. Sen, *Principles Of Electric Machines And Power Electronics*. Wiley India Pvt. Limited, 2007.

[26] Ferromagnetism - Wikipedia: http://en.wikipedia.org/wiki/Ferromagnetism.

APPENDIX A

ENGINEERING DRAWINGS

The engineering drawings of the inner ring of the bigger stage, and both rings of the smaller stage are provided. Also, the drawings for different parts of the pillar structure, the Bodine motor, and its mounting are shown.

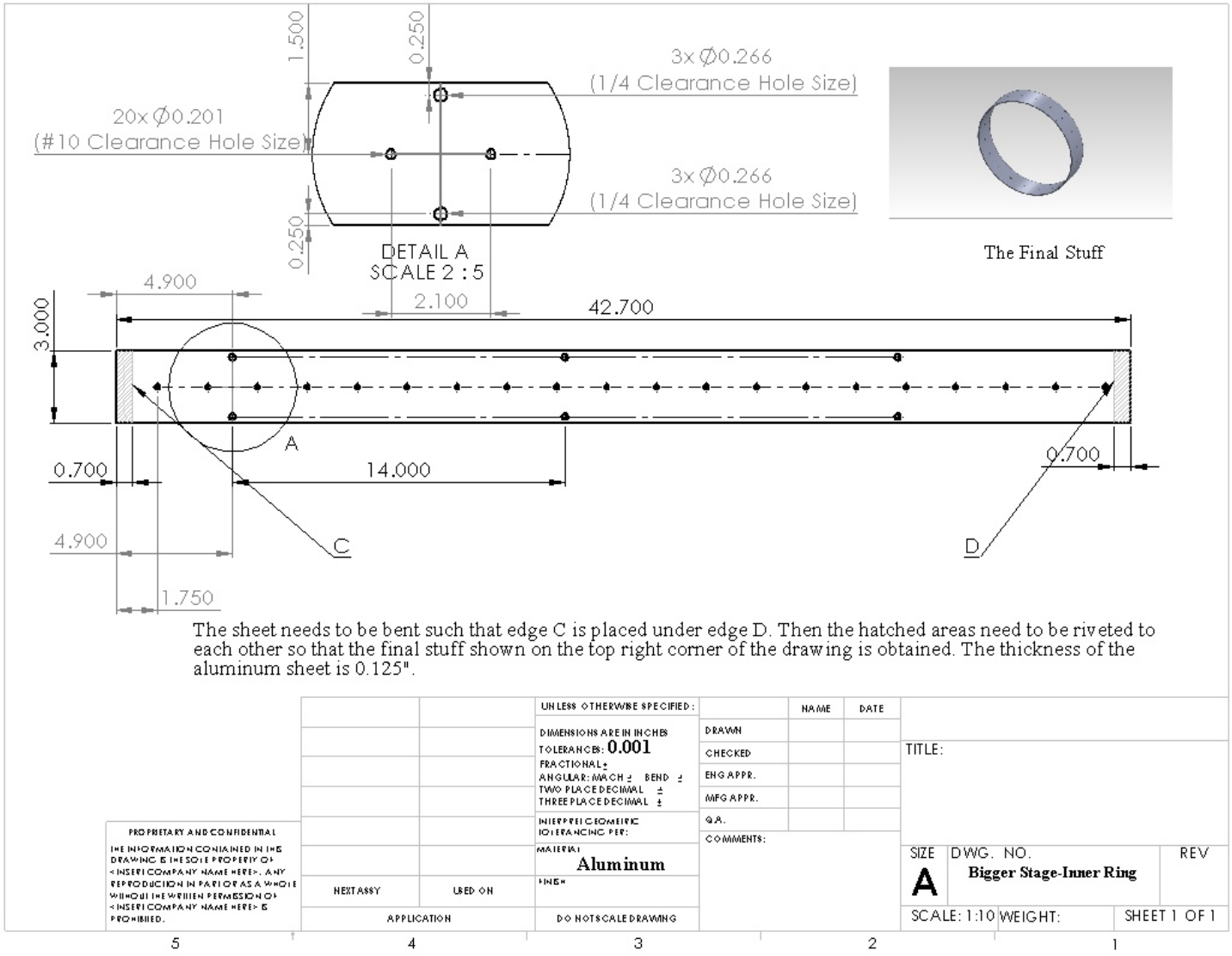

Figure A.1: Inner ring of the bigger stage.

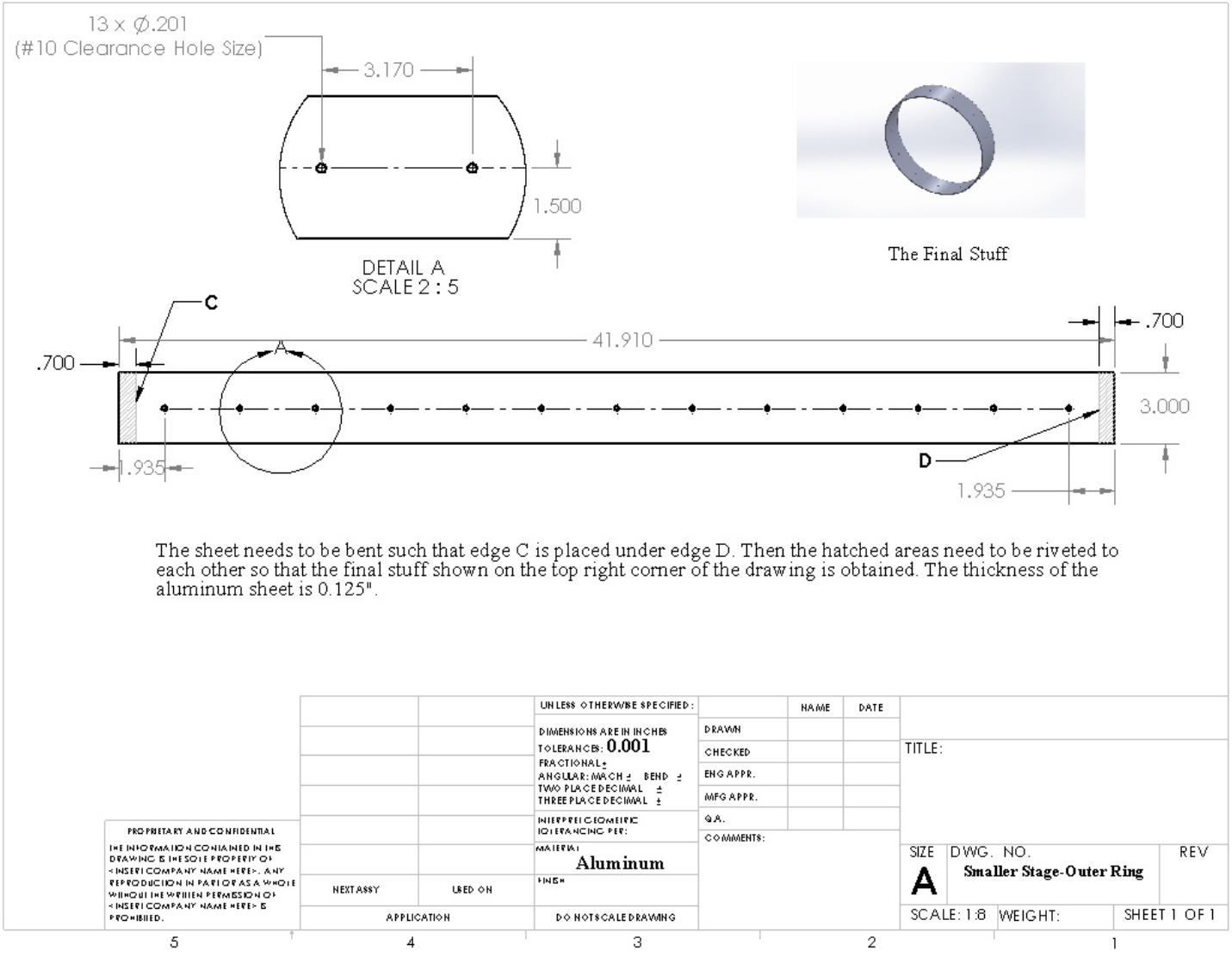

Figure A.2: Outer ring of the smaller stage.

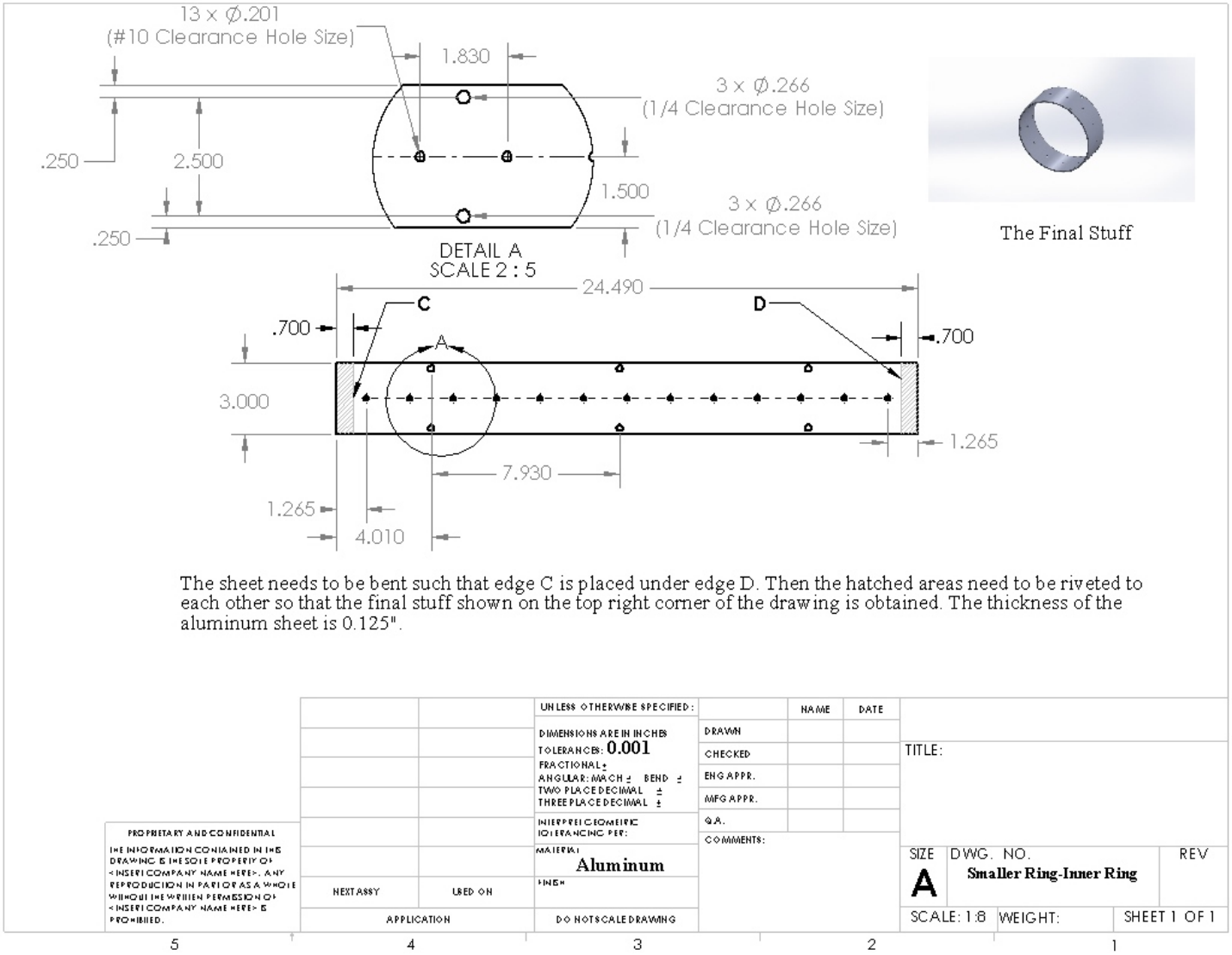

Figure A.3: Inner ring of the smaller stage.

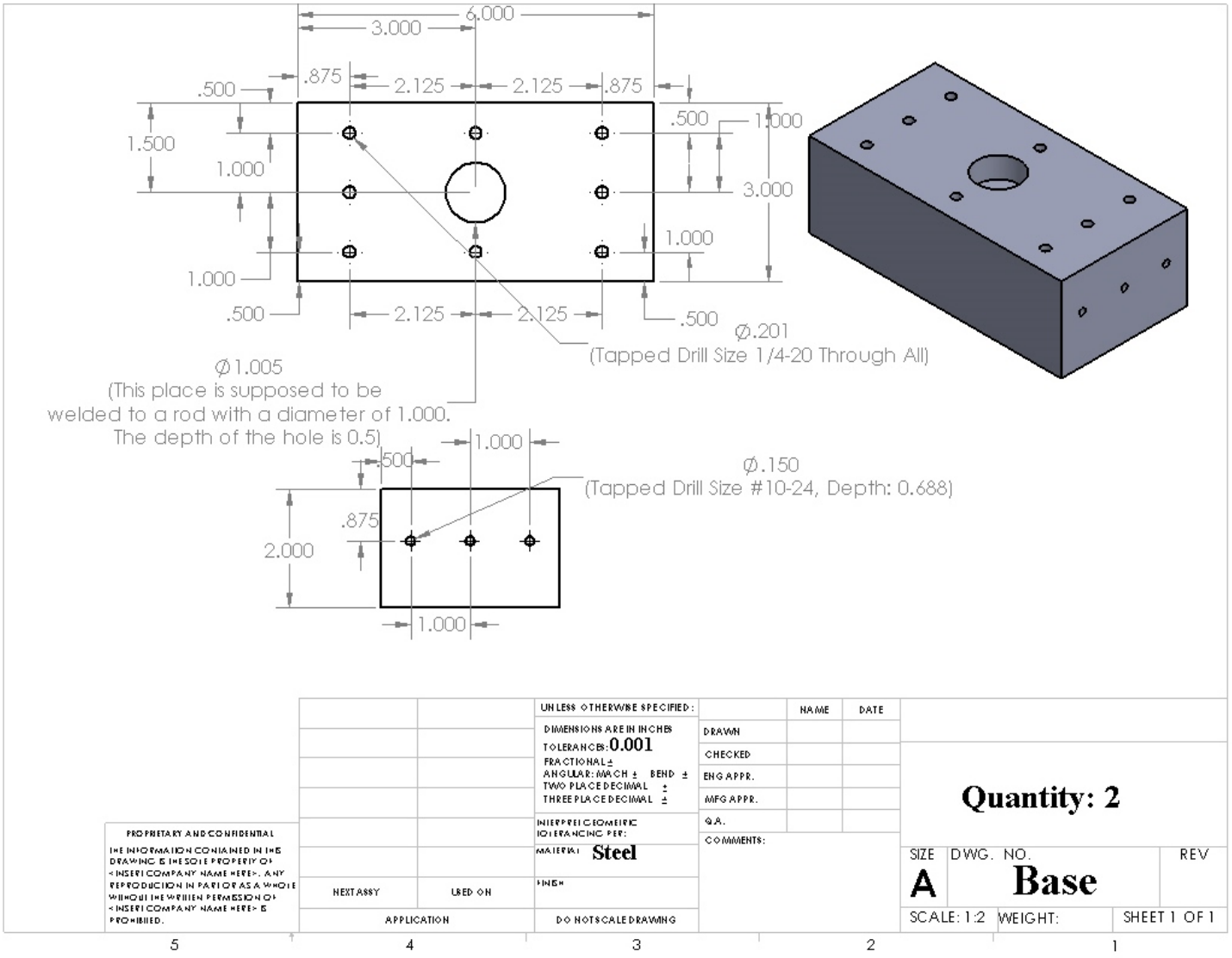

Figure A.4: Base of the pillar structure.

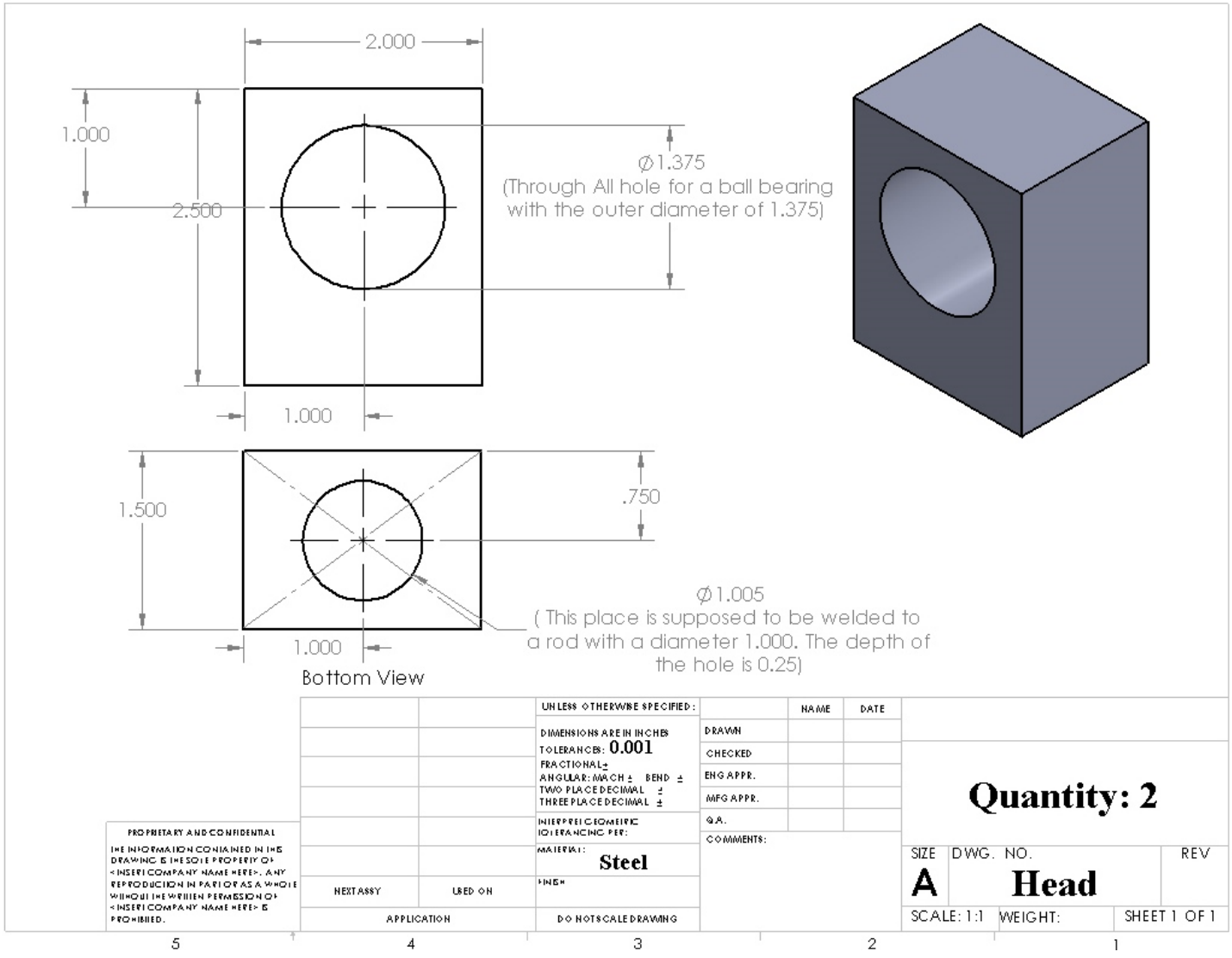

Figure A.5: Head of the pillar structure.

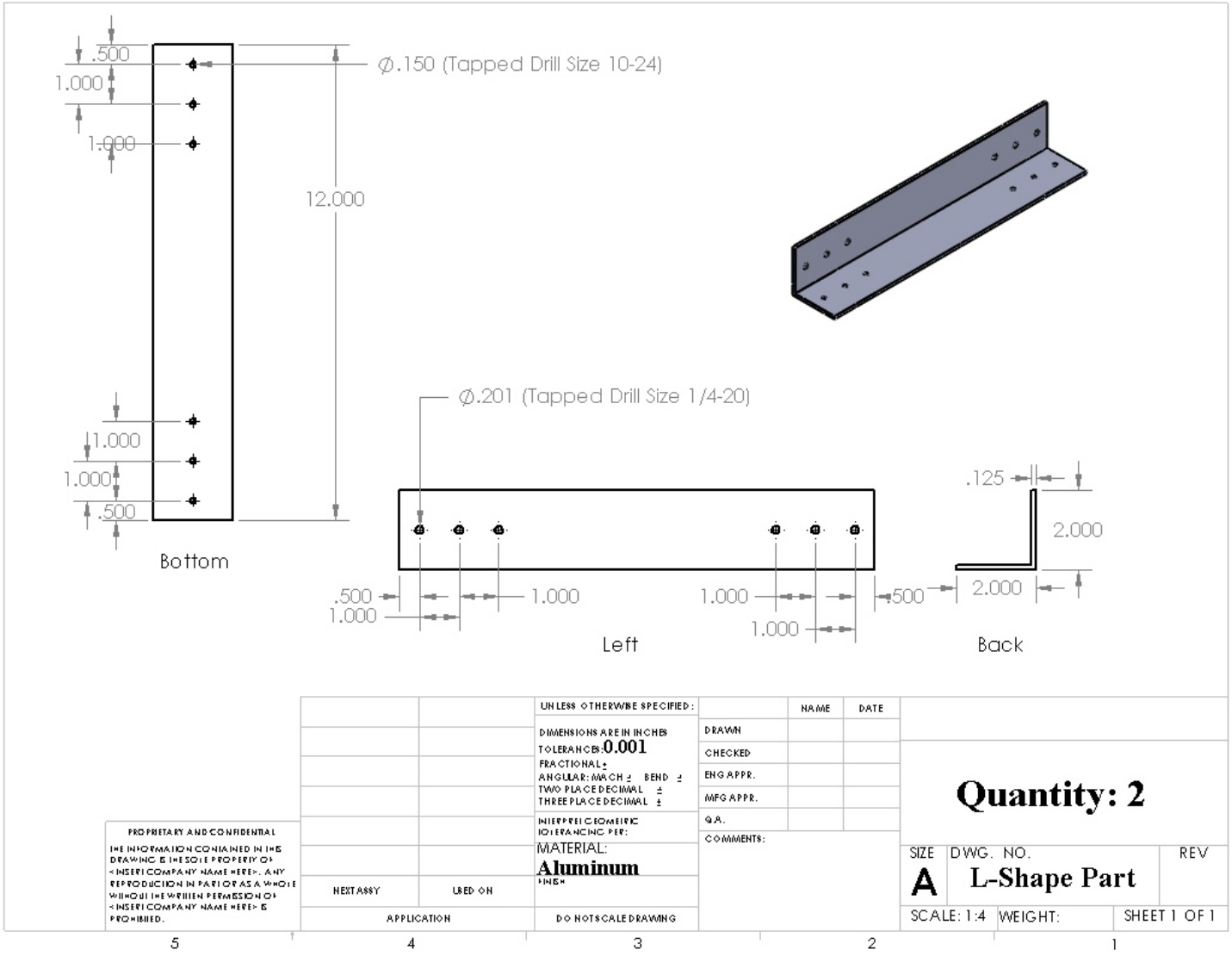

Figure A.6: L-shape part of the pillar structure.

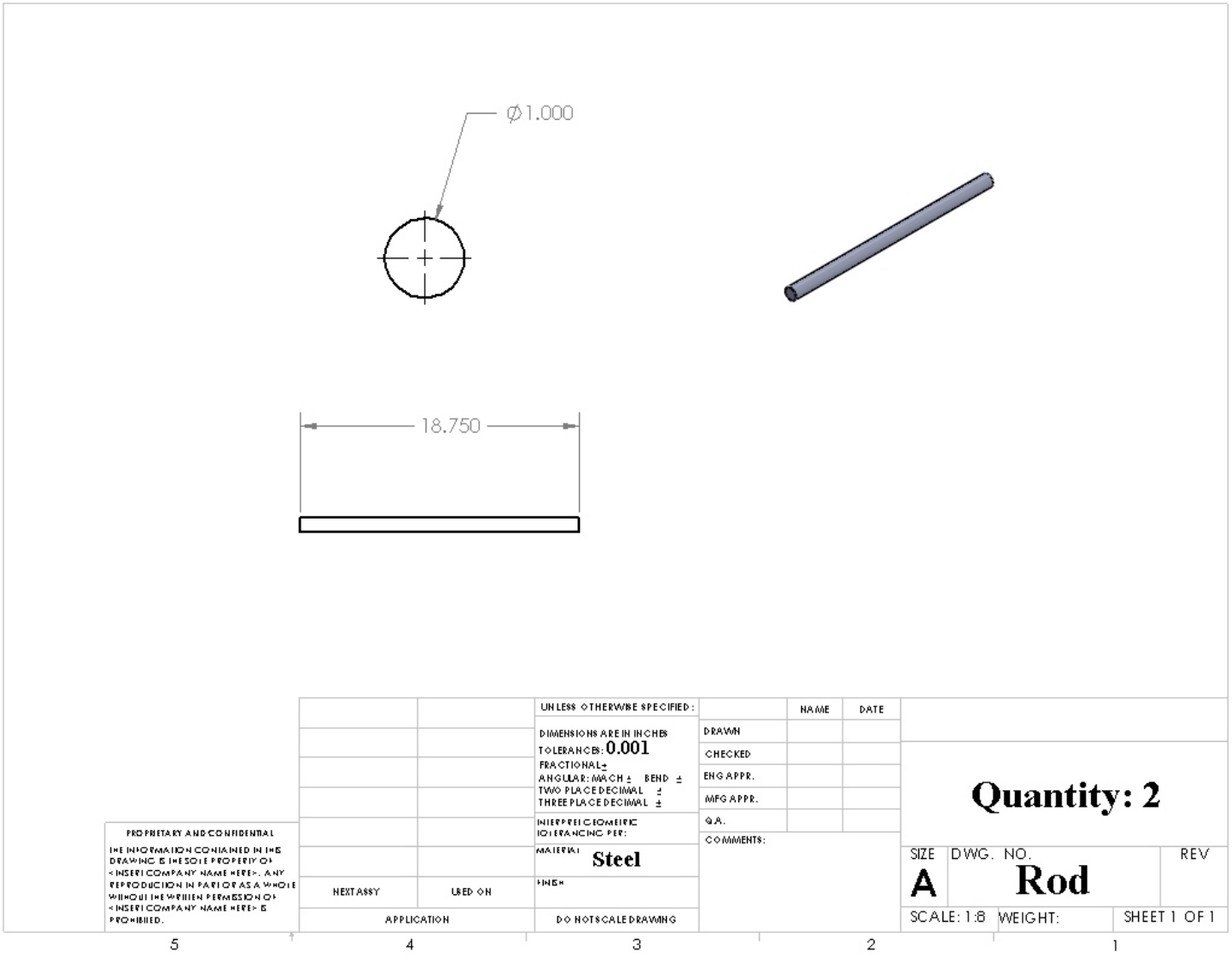

Figure A.7: Rod of the pillar structure.

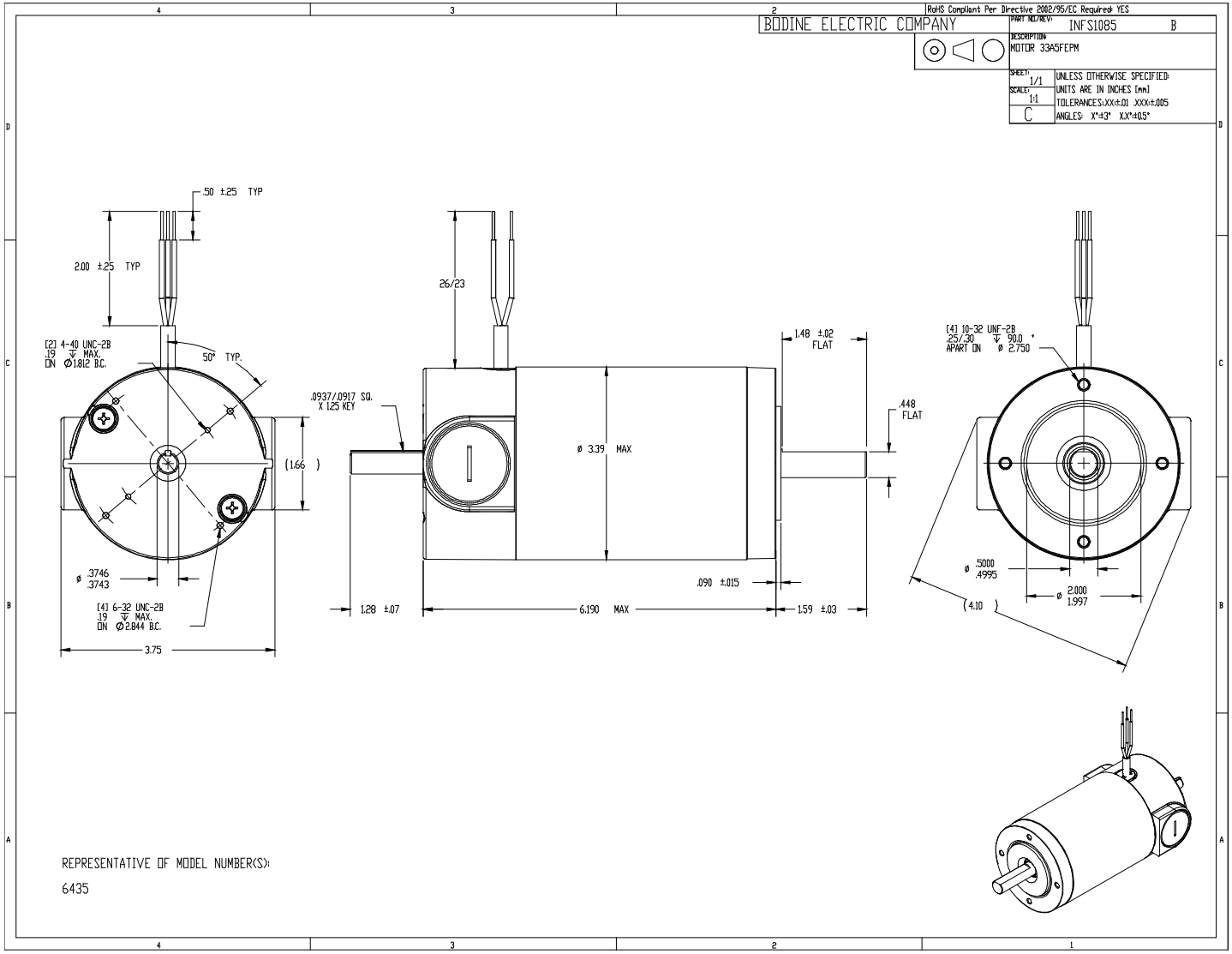

Figure A.8: Bodine motor.

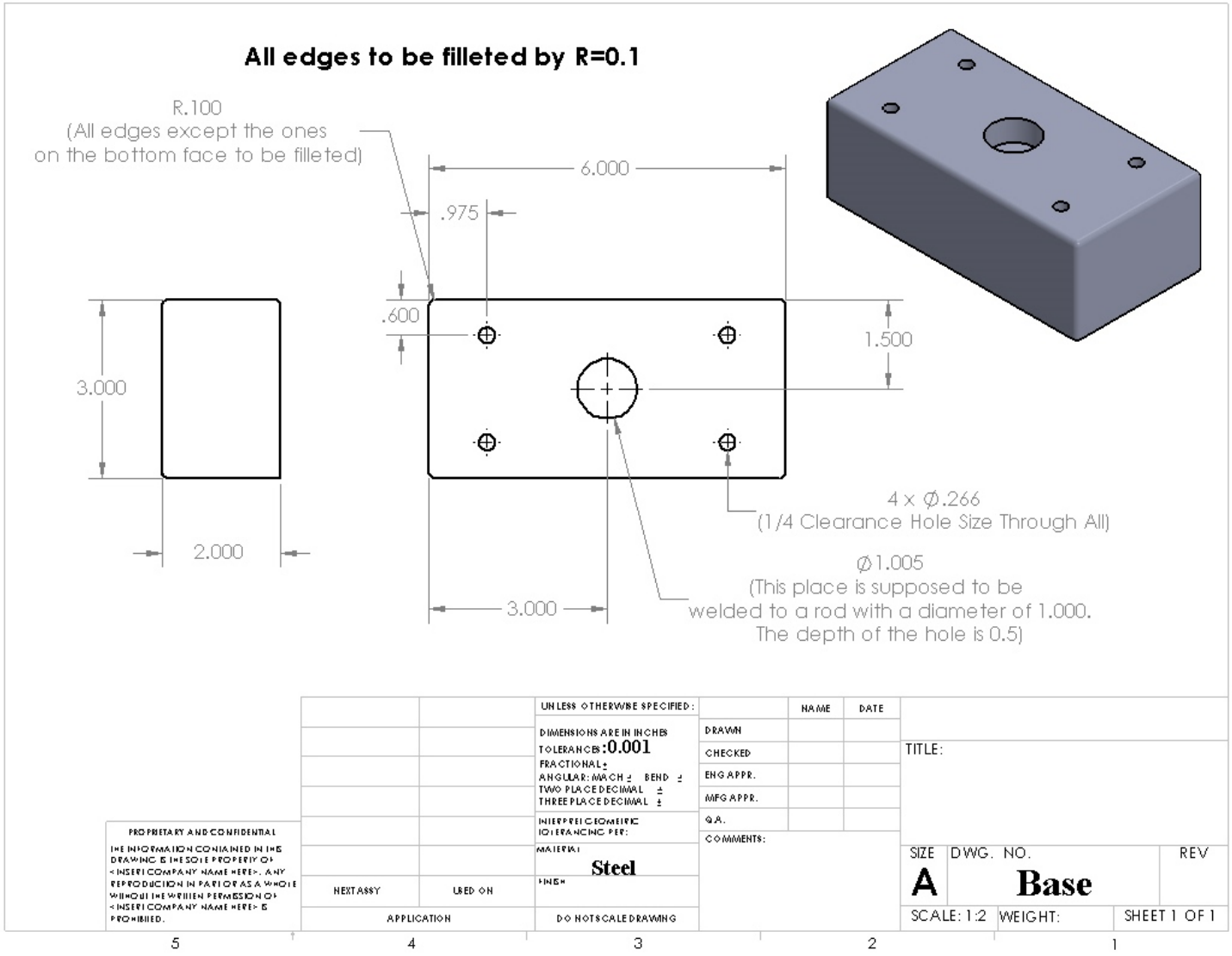

Figure A.9: Base of the mounting for the Bodine motor.

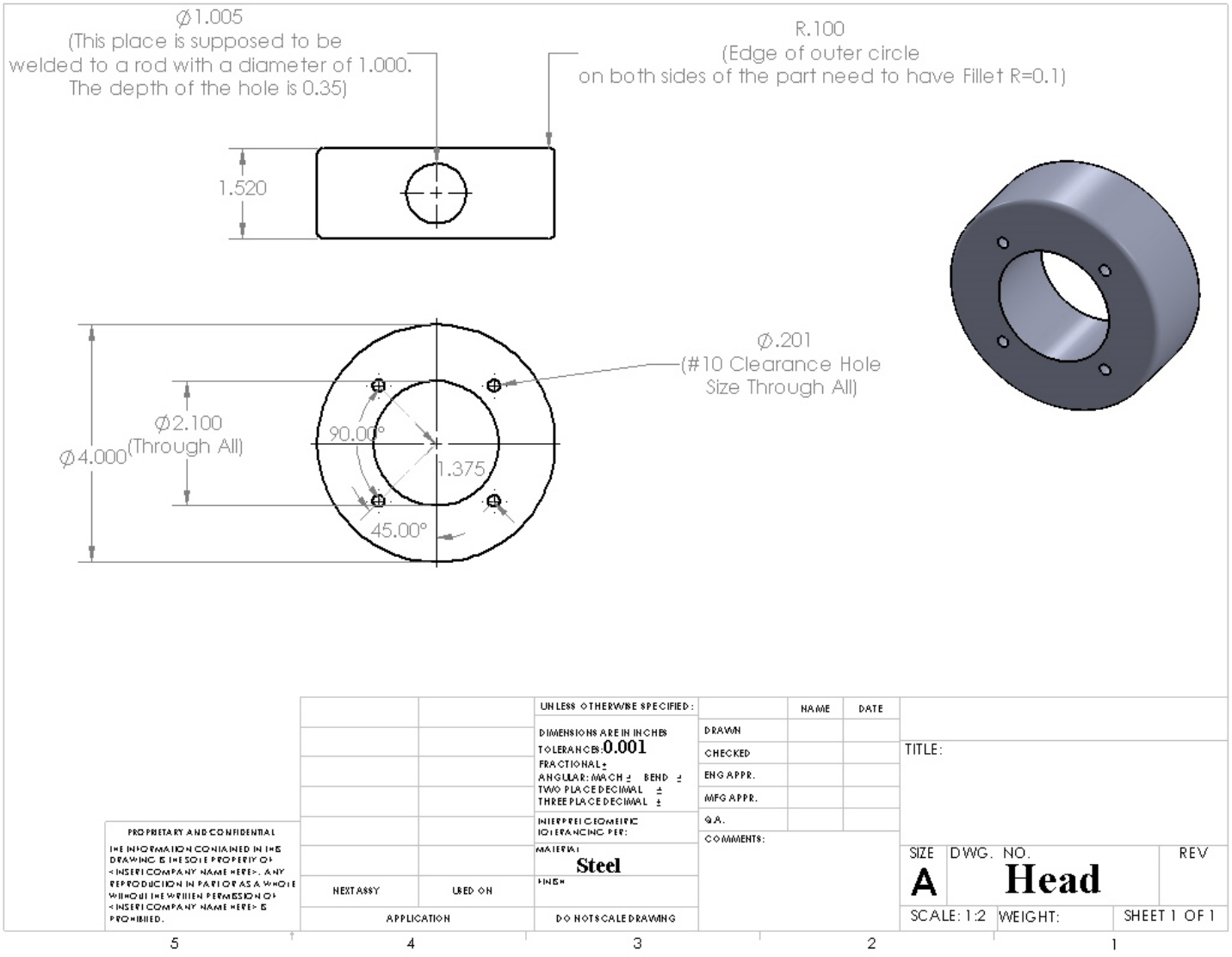

Figure A.10: Head of the mounting for the Bodine motor.

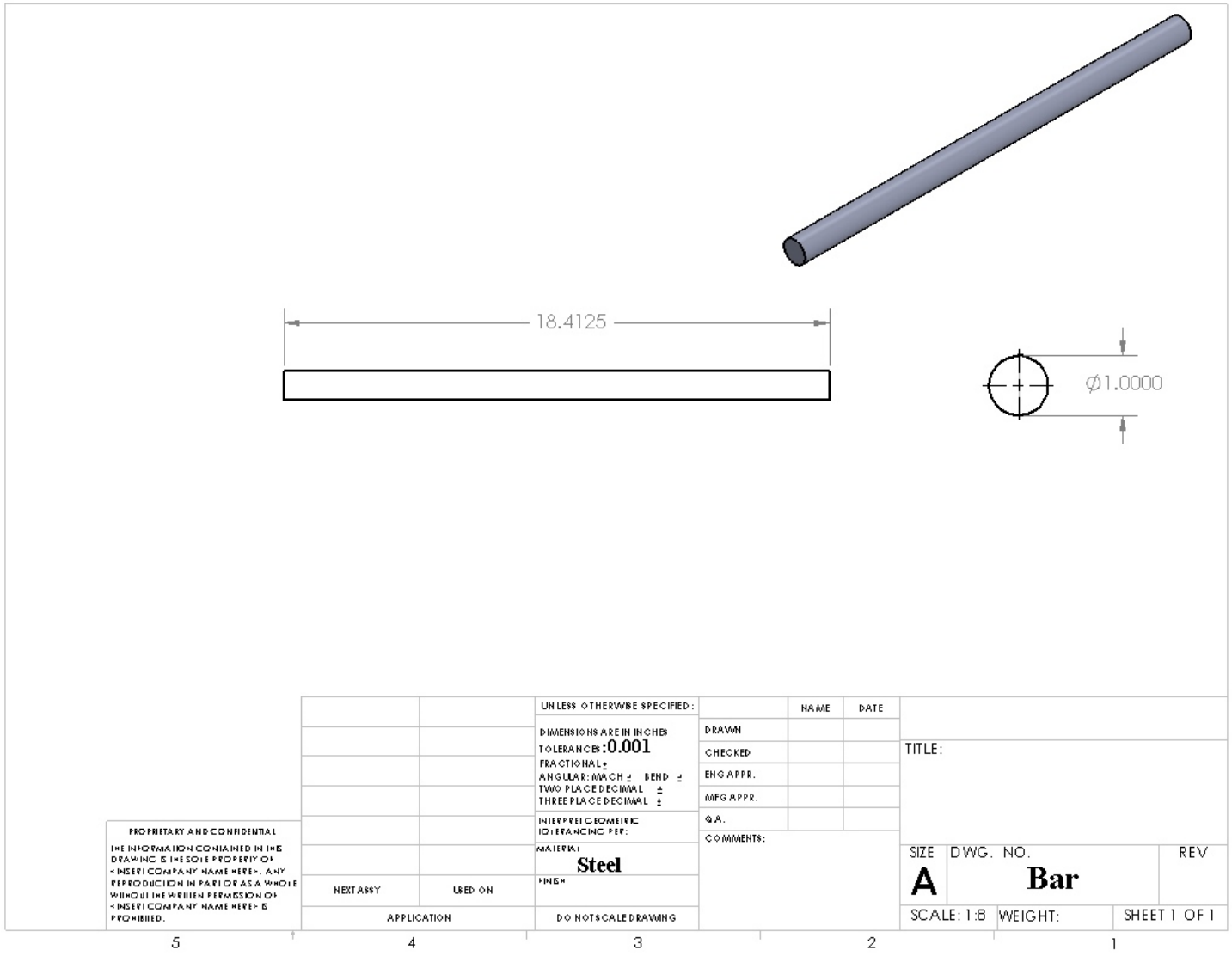

Figure A.11: Rod of the mounting for the Bodine motor.